Particle Acceleration and Detection

Ingo Hofmann

Space Charge Physics for Particle Accelerators

Springer

Particle Acceleration and Detection

The series *Particle Acceleration and Detection* is devoted to monograph texts dealing with all aspects of particle acceleration and detection research and advanced teaching. The scope also includes topics such as beam physics and instrumentation as well as applications. Presentations should strongly emphasise the underlying physical and engineering sciences. Of particular interest are

- contributions which relate fundamental research to new applications beyond the immeadiate realm of the original field of research
- contributions which connect fundamental research in the aforementionned fields to fundamental research in related physical or engineering sciences
- concise accounts of newly emerging important topics that are embedded in a broader framework in order to provide quick but readable access of very new material to a larger audience.

The books forming this collection will be of importance for graduate students and active researchers alike.

More information about this series at http://www.springer.com/series/5267

Ingo Hofmann

Space Charge Physics for Particle Accelerators

Springer

Ingo Hofmann
GSI/Technical University
Darmstadt, Germany

Goethe-University
Frankfurt

ISSN 1611-1052 ISSN 2365-0877 (electronic)
Particle Acceleration and Detection
ISBN 978-3-319-62156-2 ISBN 978-3-319-62157-9 (eBook)
DOI 10.1007/978-3-319-62157-9

Library of Congress Control Number: 2017951135

Printed on acid-free paper

This Springer imprint is published by Springer Nature
The registered company is Springer International Publishing AG
The registered company address is: Gewerbestrasse 11, 6330 Cham, Switzerland

To my dear children
Nadi, Nura, Anisa and Amin

Preface

The motivation for this book on space charge in particle accelerators has emerged from the continuing interest in the understanding and controlling of space charge effects in operating high-intensity particle accelerators and the numerous projects still under construction or in development, many of which are the world's largest instruments at the frontier of scientific and technical development.

This book focuses to a large extent on the author's angle on theoretical concepts of resonances and instabilities, in particular their coherent expressions, and attempts to connect them with simulation results and – in a limited number of cases – with experiments. Although these topics are well known in the accelerator community in the broad context of impedances or wake fields, their application to direct space charge is not yet equally well established. Utilizing terms like *coherent space charge resonances* or *coherent parametric instabilities* may be sometimes challenging; it is hoped that they will be useful to create a more systematic and differentiating picture of space charge effects, which is the primary scope of this book. It is thus complementary to existing textbooks on accelerators and beam dynamics with their much broader scope, which are needed for understanding themes that could not be adequately addressed in the format of this book.

The application of the material presented here is seen in the field of *linear* hadron accelerators at non-relativistic energies, but also in space charge issues in *circular* accelerators, like injector synchrotrons, all at basically non-relativistic energies, where direct space charge issues are of concern.

A personal remark: In preparing this manuscript, I have found time and again how challenging it is to map theoretical concepts of space charge effects to the boundary conditions of real accelerators. This is particularly true for linear accelerators, where a high level of space charge is embedded in often quite complex and transient acceleration structures.

Nonetheless it is hoped that the material presented here may be useful to all those who find that running a computer simulation code is not enough and who believe that trying to understand the gap between analytical concepts, multiparticle simulations and experiments is the best way to advance.

I am grateful to many colleagues at GSI Darmstadt, Goethe-Universität Frankfurt and Technische Universität Darmstadt, among them Oliver Boine-Frankenheim, Giuliano Franchetti, Lars Groening, Vladimir Kornilov and Jürgen Struckmeier, for the many valuable discussions. Among my international colleagues, I am particularly indebted to the late Martin Reiser, who shared his insight into space charge over many years, which I cannot adequately value. I am also grateful to Bob Jameson, who stimulated the early work on beam anisotropy; to the late Bob Gluckstern and to Robert Ryne and Tom Wangler for many inspiring discussions; and to Didier Uriot for his support, in particular by developing helpful diagnostic features (such as stability charts and tune footprints) in TRACEWIN. Last but not least, I am extremely grateful for having received highly constructive and appreciated comments on the full manuscript by Morteza Aslaninejad, Bob Jameson and Uwe Niedermayer and by Yong Liu, Ji Qiang and Rob Ryne on selected topics. Thanks go to Alex Chao also for his valuable conceptual comments.

Darmstadt, Germany Ingo Hofmann
June 2017

Contents

Chapter 1
Introduction

No one believes the simulation results except the one who performed the calculation, and everyone believes the experimental results except the one who performed the experiment.

[Quote from: Martin Greenwald, Massachusetts Institute of Technology, in [1]]

Abstract A short historical account of the early development on space charge in accelerators since the 1960s is followed by a list of books of reference on the wider field of accelerator physics. A proper distinction of *incoherent* and *coherent* in the context of resonant effects in space charge dominated beams is crucial. An equally important distinction is that between externally excited resonances – for example by error fields – and parametrically driven resonant instabilities, furthermore between isotropic and anisotropic beams. A conceptualization of these terms – by presenting a kind of guideline for the following chapters – is presented in the introduction and intended as a hopefully useful framework for interpretation of theory, simulation and experiments.

Modern particle accelerators are not thinkable without the tremendous progress in computer simulation for beam dynamics since the 1970s. Narrowing the gap between simulation models and observation of beams in real accelerators has remained a challenging task. The above quote from the context of hydrodynamic and plasma simulations, which have also prepared the ground for a great deal of accelerator beam dynamics simulation, has remained valid until today.

This is particularly true for the large-scale accelerators at high intensities, which are in operation or in planning/construction phases in a number of places in Europe, America and Asia – most of them linear accelerators. They enable many developments at the forefront of basic or applied sciences, from neutron scattering to energy, industry and environment, including future nuclear waste management by accelerator driven transmutation (see Fig. 1.1).

I. Hofmann, *Space Charge Physics for Particle Accelerators*,
Particle Acceleration and Detection, DOI 10.1007/978-3-319-62157-9_1

Fig. 1.1 Worldwide locations of major high intensity and high power accelerators in operation, planning or construction

For contrast, the first room-size particle accelerators from before World War II were practically hand-calculated – and yet they led to the discovery of new particles. Today's accelerators are not only designed by computers; operation at high beam power requires the use of computers to model and optimize beam behaviour. Predicting and controlling beam loss at high intensity, with space charge as major source of loss, is crucial for minimizing radioactivity in such facilities. This is a must for optimizing their performance and carrying forward the intensity frontier.

Hence, an in-depth understanding of the physics behind space charge – using analytical theory, simulation as well as experiments – is essential and the primary motivation behind this book.

1.1 Historical Remarks

A brief historical account may be in place here. In the early time of accelerators – the 1950s and 1960s – it was understood that the demand for higher intensity would soon be increasing, and understanding and controlling of beam space charge would become more and more important. Steady improvements in intensity were made, but this was primarily a technical challenge at the accelerator "front end", for example how to improve the performance of proton or ion sources and of low beta acceleration. Gradually, first analytical-numerical concepts on space charge were developed in the 1960s: Significant contributions were the exploration of gradient errors with space charge by Smith in [2]; the rms envelope equations by his student Sacherer in [3]; and the first analysis of 2D oscillation modes by Gluckstern in [4] – just to mention some of them.

The field of space charge and its limiting effects on beam intensity received an important boost with the proposal in the mid-1970s to use heavy ion accelerators as drivers for inertial fusion energy production, which required pushing intensity several orders of magnitude beyond state-of-the-art.[1] The first self-consistent Vlasov analysis of "space-charge induced transverse instabilities" in 2D beams in periodic focusing in [6] emerged from this project.

Since the late 1990s linear accelerator based high intensity spallation neutron sources triggered enhanced interest in space charge problems, also for rings, and efforts were increased towards a better understanding of the issues as well as laying a safe ground for the control of space charge effects. At the Shelter Island Workshop (Shelter Island, New York, 1998) Baartman in [7] justified that space charge deserves its own language: "Forces arising from the beam itself are not the same as external forces ... any theory which treats the two types of forces in the same way is incorrect and will make incorrect predictions."

1.2 Important Other Sources of Reading

The scope of this book is not to enter into details of the numerous fundamental concepts of accelerators and the large diversity of important facets of particle motion or collective beam interaction beyond direct space charge, which is the focus. Many other sources of reading exist for the field at large.

One of the early and remarkable books on space charge, among the very few in this direction that existed over three decades ago, was written by Lawson [8]. Computer simulation played no role at all, but Lawson helped understanding many questions in his own stimulating language. His book and ideas inspired Martin Reiser at Maryland University to build – from the 1990s onwards – several very compact electron devices. They helped addressing experimentally many questions about space charge up to the present day. Many of these findings, along with theoretical models and computer simulation examples, went into the book by Reiser [9], which become one of the indispensable sources of beam physics with space charge in a broader context.

In the field of rf linear accelerators, the book by Wangler [10] grants insight into beam dynamics and the role of space charge as well as design issues of high current linear accelerators.

Readers interested in nonlinear beam dynamics in storage rings will find a profound treatment of this subject in the book by Forest [11].

A broader selection of topics, also including the vast fields of collective effects, with selected topics on space charge, is found in the books by Chao et al. [12], Wiedemann [13], Lee [14] and others.

Students in particular may find it useful to use the published lectures from the CERN Accelerator School in [15] and the U.S. Particle Accelerator School in [16].

[1]A recent review of this project is found in [5], where also other energy related accelerator applications are reviewed.

1.3 What Are Space Charge Dominated Beams?

The notion of *space charge dominated* beams is not sharply defined and differs between linear and circular accelerators. In this book only “direct” space charge is considered assuming only electrostatic interaction of the charged particles within a bunch, or between line charges in a coasting beam model. Bunch-to-bunch, image, impedance or wake field effects would go beyond the scope of this book.

In synchrotrons an intensity limiting criterion used in the early days was guided by the idea not to have space charge tune shifts exceed the $\frac{1}{4}$ tune separation between fourth order resonances. It was learnt later that such a definition is not well-justified and often too conservative. In view of the diversity of space charge effects more specific criteria needed to be defined, including the role of coherent space charge effects.

In linear accelerators an early hand-waving argument, without real justification, was to let space charge – in the average – cancel about half of the external focusing force. This amounts to $\approx$30% reduction of the zero-current tune by space charge. In modern high current accelerators, though, much higher peak values are achieved on the basis of criteria, which consider the diverse relevant space charge effects.

1.4 Incoherent and Coherent Effects

Incoherent and *coherent* space charge effects are a central issue in the following chapters. These terms are not used in an unambiguous way in beam dynamics literature, however. Here they are understood as characterising the difference between single particle and collective response behaviour.

In circular accelerators *coherent mode* is frequently understood as dipole mode of oscillation causing a displacement of the beam as a whole, and *incoherent* as betatron oscillations of single particles. We ignore dipole mode instabilities here – they are not governed by direct space charge only – and focus on second order and even higher order modes, which may be resonantly driven by the lattice in combination with space charge and possibly beam anisotropy. The distinctive feature of *coherent* is a clear, observable frequency associated with the specific kind of mode. This leads to a coherent frequency shift entering into its condition of resonance. *Incoherent* motion is much more difficult to measure – often impossible – as it is part of the equilibrium beam; this is understood as a modulation following the periodic pattern of the focusing lattice.

In principle, this is not very different in high intensity linear accelerators, where the strength of space charge forces – relative focusing forces – is even more pronounced. Coherent motion of the beam core may result from lattice transitions or focussing discontinuities, but also from the resonant action of the lattice including space charge. As in circular accelerators, coherent space charge modes introduce new frequencies, which are not present in the matched beam and can be observed – at least in simulations.

1.5 Terminology of Resonance, Coherence and Instability

The terms of resonance, coherence, instability and parametric play a key role in this book. Generally speaking, they are not always used in an unambiguous way in the available literature. The following nomenclature is intended to be a consistent guide through the various chapters of this book hoping that it may also be useful beyond it.

Instabilities are understood as feedback processes growing exponentially from the noise level. Resonances require periodic action on single particles or eigenmodes – usually due to an *external driving force*, which can be also the space charge self-field of the beam.

We distinguish between a number of cases. First, note that a *coherent resonance condition* expresses the appearance of a coherent space charge shift in the resonance condition, in addition to the space charge shifted rms tunes of single particles; second, space charge structure resonances are driven by the periodic *matched beam space charge force*, which by itself is *not* a coherent feature.

- *Incoherent, also called single particle resonances*: they can be
  (1) *error resonances* due to error magnet multipoles;
  (2) *structure resonances* due to a magnet multipole with lattice structure periodicity; but also due to a space charge pseudo-multipole with lattice structure periodicity, in which case they are called *space charge structure resonances*; both cases are described as *incoherent* or – as alternative nomenclature – *single particle* resonance based on the space charge shifted tune of single particles (but *not* a coherent frequency shift as in the subsequent item).
- *Coherent resonances*:
  (1) coherent eigenmodes of oscillation – not just oscillating single particles – can be driven by error magnet multipoles[2]; described by a *coherent resonance condition*, which includes a coherent frequency shift (otherwise an incoherent resonance).
  (2) alternatively, coherent eigenmodes in beams with more than one dimension can be driven by anisotropy, e.g. different emittances and/or average focusing constants; described by *coherent difference resonance* conditions.

[2]For example a gradient error driving an envelope mode in a circular accelerator; this can also occur with the structure gradient, in which case the condition would correspond to the first "Mathieu" stopband – see Sect. 7.1.1.

- *Coherent parametric instabilities*[3]:
  coherent eigenmodes of oscillation are resonantly growing due to the parametric action of a system parameter – here the periodic modulation of the focusing force; they are called here *parametric instabilities* if they are associated with a half-integer (1:2) frequency relationship[4]; described, accordingly, by *coherent half-integer resonance* conditions.

In beam dynamics literature such coherent parametric instabilities are also called *structure space charge instabilities*; the more accurate term *parametric* is preferable as it also helps to adequately describe the phenomenon of sum coherent parametric instabilities in Chap. 7. Sum parametric resonances/instabilities are well-known in parametric resonance theory in theoretical mechanics; in beam dynamics, and as a *coherent* phenomenon, they have only been recently considered.

In circular accelerator literature the emphasis is primarily on magnet error driven resonances. In linear accelerators, however, coherent instabilities, to some extent also incoherent structure resonances by space charge, are a major source of beam degradation. The lower degree of periodicity in linear accelerators is easily outweighed by the higher level of space charge and its intrinsic strong nonlinearity.

Note that the direct space charge driven instabilities discussed here are practically always subject to resonance conditions. Non-resonant instabilities can be driven by dissipative mechanisms, like the resistive wall instability, which are not considered here.

1.6 Analytical and Simulation Approaches

Progress in the control of space charge in design, optimization and operation of high intensity and high power accelerators is owed to both, analytical studies as well as advanced particle-in-cell computer simulations. An in-depth understanding of the diverse effects of space charge is the basis for the interpretation of simulation and experiments.

Beam dynamics at high intensity is an interplay of single-particle nonlinear dynamics with various coherent and parametric resonance effects. The goal of comparisons between analytical results, simulation and experiments must be to clarify the importance of this interplay under realistic conditions.

Several important topics cannot be adequately covered here, although they are interwoven with space charge: among them the role of errors in linear accelerators, which are a driving source for emittance growth and halo; out of the broad field of magnet error driven resonance effects in circular accelerators only selected

[3]To be distinguished from *single particle* parametric instabilities, see Sects. 7.1 and 6.1.

[4]Where the eigenmode oscillates at half the lattice periodicity. Note that these modes have been addressed under the name “space-charge induced transverse instabilities” in [6], where also other (not necessarily practically significant) frequency relationships were considered, like 1:1 etc.

examples are presented; and the wide area of impedance driven collective effects in circular accelerators, where space charge also plays a role, is beyond the scope of this book.

1.7 Overview

The material is presented in the following way:

Chapters 2 and 3 review basic concepts on phase space dynamics leading to Vlasov's equation as important analytical tool needed further on; the concept of matched equilibrium beams is outlined in Chap. 4.

Chapter 5 exposes the nature of different modes of interaction when dealing with space charge on a general level; this includes the role of resonance vs. instability and of incoherent vs. coherent oscillations. Followed by a review of the Vlasov theory of anisotropic coherent eigenmodes and a discussion of the role of negative energy waves and of Landau damping, this chapter lays the ground for the later Chaps. 7, 8 and 9. Chapter 6 applies part of this to analyse space charge in mismatched beams.

A central theme of space charge interaction in this book is that of coherent parametric instabilities dealt with in Chap. 7; it is followed in Chap. 8 by a discussion of selected coherent and incoherent resonance effects in circular machines driven by magnet errors; and by Chap. 9 on anisotropic beams in linear or circular accelerators, where the role of coherent effects on emittance exchange between planes due to different emittances and/or focusing strengths is discussed in some detail.

Chapter 10 summarizes the relevance of the discussed space charge effects in the design of circular and linear accelerators, and an Epilogue offers a brief outlook.

Literature is found sorted by chapter. No claim of completeness is made, and I therefore apologize for having omitted relevant and important contributions to the field.

References

1. M. Greenwald, *Beyond benchmarking – how experiments and simulations can work together in plasma physics*. Comput. Phys. Commun. **164**, 1–10 (2004)
2. L. Smith, in *Proceedings of the International Conference on High Energy Accelerators*, Dubna, 1963, p. 897
3. F.J. Sacherer, Ph.D. thesis, University of California at Berkeley [UCRL-18454, 1968]
4. R.L. Gluckstern, in *Proceedings of the Linac Conference* (Fermilab, Batavia, 1970), p. 811
5. I. Hofmann in *Reviews of Accelerator Science and Technology: Accelerator Applications in Energy and Security*, vol. 8, ed. by A.W. Chao, W. Chou (World Scientific, Singapore, 2015)
6. I. Hofmann, L.J. Laslett, L. Smith, I. Haber, Part. Accel. **13**, 145 (1983)
7. R. Baartman, Betatron resonances with space charge, in *Workshop on Space Charge Physics in High Intensity Hadron Rings*, Shelter Island, 1998. AIP Conference Proceedings, vol. 448 (AIP Press, New York, 1998), p. 56

8. J.D. Lawson, *The Physics of Charged Particle Beams*, 2nd edn. (Clarendon Press, Oxford/New York, 1988)
9. M. Reiser, *Theory and Design of Charged Particle Beams*, 2nd edn. (Wiley, Weinheim, 2008)
10. T.P. Wangler, *RF Linear Accelerators*, 2nd edn. (Wiley, New York, 2008)
11. E. Forest, Beam dynamics, in *The Physics and Technology of Particle and Photon Beams* (CRC Press, 1998)
12. A.W. Chao, K.H. Mess, M. Tigner, F. Zimmermann (eds.), *Handbook of Accelerator Physics and Engineering*, 2nd edn. (World Scientific, Singapore, 2013)
13. H. Wiedemann, *Particle Accelerator Physics II* (Springer, Berlin/Heidelberg, 2012)
14. S.Y. Lee, *Accelerator Physics*, 2nd edn. (World Scientific, Singapore, 2004)
15. http://cas.web.cern.ch/cas/
16. http://uspas.fnal.gov/

Chapter 2
Phase Space Dynamics in Theory and Simulation

Abstract Particle motion in accelerators is usually assumed in 6D phase space, under the action of external forces for acceleration and focusing, and with space charge interaction resulting from the Coulomb interaction between particles. The by far dominating contribution to direct Coulomb interaction in accelerator beams is via the so-called mean field or self-consistent space charge potential, which is calculated from an assumed smoothed charge density $n(x, y, z, t)$, and ignoring the discreteness of charges. Assuming that collisional effects can be neglected, this chapter introduces the Vlasov-Poisson equations and the important concepts of emittance, rms equivalence as well as beam anisotropy. In the context of computer simulation, however, some aspects of artificial collision and noise effects due to numerical discretisation are an important subject, which is also briefly discussed.

2.1 Basics of Kinetic Theory

In this section the Vlasov-Poisson equations suggested by Vlasov in [1] are introduced as collision-less limit of the Fokker-Planck-equation.[1] They are the main tool for a self-consistent analytical modelling of space charge effects in 4D and 6D phase space, while the Fokker-Planck approach is used here only for the discussion of numerical collision effects in particle-in-cell simulation.

The importance of the dynamics in 4D or 6D phase space – understood as *kinetic approach* – is illustrated in Sects. 2.1.4 and 5.6 by an example of non-kinetic so-called "fluid models", which reduce the problem to a simplified flow in real space.

2.1.1 Single Particle Motion in a Smooth Field

Ignoring collisional or dissipative effects we first consider here equations of motion in x, y, z with linear, time-dependent external focusing forces and – in

[1]Collision effects by elastic small angle scattering are ignorable in linear accelerators, but not always in circular accelerators. In the latter the "intrabeam scattering" is an important subject on long time scales as in storage rings or colliders, but it has no direct influence on space charge effects and is thus beyond the scope of this book.

I. Hofmann, *Space Charge Physics for Particle Accelerators*,
Particle Acceleration and Detection, DOI 10.1007/978-3-319-62157-9_2

general nonlinear – electrical forces generated by a time-dependent space charge distribution[2]:

$$\begin{aligned}
\ddot{x} &= -K_x(t)\,x + \frac{q}{m\gamma^3}E_x(x,y,z,t)\\
\ddot{y} &= -K_y(t)\,y + \frac{q}{m\gamma^3}E_y(x,y,z,t)\\
\ddot{z} &= -K_z(t)\,z + \frac{q}{m\gamma^3}E_z(x,y,z,t),
\end{aligned} \tag{2.1}$$

with q the ion charge, m the ion rest mass, γ the relativistic factor and $K_{x,y} \equiv \pm B'/[B\rho]$. $[B\rho]$ is the magnetic rigidity ($= m\gamma\beta c/q$, with βc the particle velocity), B' the quadrupole gradient and $K_z(t)$ the equivalent longitudinal focusing in case of a bunched beam. Next we assume that the electric field in the moving frame can be calculated from Poisson's equation

$$\nabla_{\mathbf{x}} \cdot \mathbf{E}(x,y,z,t) = \frac{q}{\varepsilon_0}\, n(x,y,z,t). \tag{2.2}$$

Here $n(x,y,z,t)$ is the particle density determined from an assumed distribution f of particles in 6D phase space, such that the number density in a small phase space volume is given by

$$dN = f(x,y,z,p_x,p_y,p_z,t)\; dx\, dy\, dz\, dp_x\, dp_y\, dp_z \tag{2.3}$$

and the particle density in real space by

$$n(x,y,z,t) = \int\int\int f\, dp_x\, dp_y\, dp_z. \tag{2.4}$$

2.1.2 Fokker-Planck Equation

Liouville's theorem for systems described by a Hamiltonian says that the volume of a phase space element occupied by particles remains invariant in time along its trajectory. For charged particles Coulomb interaction must be included and, strictly speaking, Liouville is only valid in the $6N$-dimensional Γ-space. In this hyper phase space the invariance of density is described by a vanishing total derivative of the corresponding distribution function, $df/dt = 0$.

The relatively weak collisional effects in charged particle beams can be taken into account in the reduced 6D phase space by assuming a splitting of the Coulomb

[2] Here and in the following it is assumed that the motion in the external focusing optics is first-order and in *paraxial ray* approximation (see also in [2])

interaction into a time-dependent self-consistent (mean field) space charge potential plus a part due to collisions. The collisional part leads to the Boltzmann-type collision term on the r.h.s. of the total derivative of a distribution function in 6D phase space, e.g. $df/dt = [\partial f/\partial t]_{coll}$.

Under certain conditions the latter can be written as sum of a diffusion and a friction term (see, for example, [2–4], or [5]),

$$\begin{aligned}\frac{df}{dt} &= \frac{\partial f}{\partial t} + (\dot{\mathbf{x}}\cdot\nabla_{\mathbf{x}})f + \left(\dot{\mathbf{p}}\cdot\nabla_{\mathbf{p}}\right)f = [\frac{\partial f}{\partial dt}]_{coll} = \\ &-\sum_i \frac{\partial}{\partial p_i}\{F_i(\mathbf{p},t)f\} + m^2\gamma^2 \sum_{i,j} \frac{\partial^2}{\partial p_i \partial p_j}\{D_{ij}(\mathbf{p},t)f\},\end{aligned} \tag{2.5}$$

where the F_i stand for the friction vector, and the D_{ij} for the diffusion tensor. With $\dot{\mathbf{p}} = m\gamma\,\ddot{\mathbf{x}}$ and the equations of motion Eqs. 2.1 for an externally provided – in general time-varying – linear focusing force plus the self-consistent space charge force from Eq. 2.2 a closed system of equations is obtained.

In Sect. 2.3 the r.h.s. collision term is the starting point for a discussion of the unphysical noise in PIC-simulation caused by finite grid and particle number effects. Besides this it is not further considered.

2.1.3 Liouville and Vlasov-Poisson Equations

Beam evolution with space charge can be described in the collisonless limit, with $[\partial f/\partial t]_{coll} = 0$, by Vlasov's equation

$$\frac{df}{dt} = \frac{\partial f}{\partial t} + (\dot{\mathbf{x}}\cdot\nabla_{\mathbf{x}})f + \left(\dot{\mathbf{p}}\cdot\nabla_{\mathbf{p}}\right)f = 0 \tag{2.6}$$

to be solved jointly with Poisson's equation Eq. 2.2. Liouville's theorem applies in 6D phase space as a result of the canonical equations of motion, hence the volume of a phase space element occupied by particles remains invariant in time – however distorted it gets under the effect of nonlinear forces as is shown schematically in the reduced 2D phase space example of Fig. 2.1.

In such a system there is no growth of the exactly determined phase space volume, if "infinite phase space resolution"[3] is assumed. With finite resolution growth of the effectively determined phase space volume can result from distortion and progressive filamentation processes in phase space – even though the phase

[3]The assumption of "infinite phase space resolution" is a hypothetical one; phase space resolution is always limited – ultimately by quantum mechanics –, which is the basis of entropy growth in a real system in the absence of collisions – see also [6].

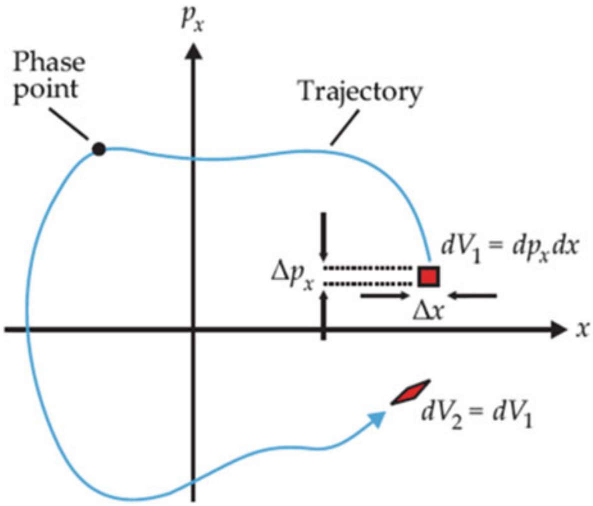

Fig. 2.1 Principle of the area invariance of a phase space element in 2D phase space along a trajectory

space flow as such is collisionless. This requires, however, nonlinear forces and mixing of void regions with regions occupied by particles. Growth of the rms emittances (see Sect. 2.2.2) as a very coarse measure of a phase space volume is then also inevitable.

Progressive filamentation of phase space can be also limited by physical processes, besides finite phase space resolution. An example is the space charge induced multi-stream instability, which eventually destroys a regular filamentary structure as is shown in Sect. 5.4.2.

Whenever coupling forces from external sources or from space charge are absent or small, reduced Vlasov-Poisson equations, for example in the transverse or longitudinal phase space alone, are obtained by integration. Transverse Vlasov-Poisson equations in 4D phase space are strictly valid in *coasting beam* approximation, where no dependence on the longitudinal coordinate exists (see Sect. 5.3).

2.1.4 Fluid Models

While the Vlasov-Poisson formalism in phase space is a fully kinetic theory, attempts have been made to approximate the problem in a non-kinetic fluid-type model by integrating over momentum space. The loss of the full information on the velocity space, with only a "temperature" left, is a severe simplification; nonetheless the model is helpful for a distinction between kinetic and non-kinetic modes. As an example we refer to Lund and Davidson in [7], which will be discussed further in Sect. 5.6.

2.2 Emittance and Anisotropy

A beam is defined as ensemble of particles moving in a given direction, with small deviations of individual particles in positions and times or energies from a so-called reference particle. Maintaining *high beam quality* implies keeping these deviations, respectively their rms values as small for as high a fraction of particles as possible. The concept of *beam emittance* has been developed to quantify the occupied phase space volume in measurable quantities. While the complete information is only given by the full distribution in 6D phase space, projections onto separate 2D phase planes related to x, y or z are more accessible to measurements and therefore the usually preferred quantities.

Here it must be kept in mind that nonlinear forces from external sources or space charge may lead to coupling between different phase planes. Also, the 6D distribution may reveal correlations between mixed phase planes, which are not described by separate projections in x, y or z. Such correlations may be given initially, or as a result of coupling forces. In this context the characterization of beam "anisotropy" between degrees of freedom by introducing a suitable rms anisotropy factor is helpful; it should be used instead of the occasionally used – but not appropriate – idea of "temperature ratios".

Further details on this topic are found, for example, in [2] or [3].

2.2.1 *Trace Space Emittances*

For convenience and comparison with measurements based on the directions of particles, the 6D phase space is usually replaced by the so-called *trace space*. Using the distance $s = \mathrm{v}t$ of a reference particle moving with velocity $\mathrm{v} = \beta c$, the divergences $x' \equiv dx/(\beta c dt)$ (and similar in y or z) are suitable quantities to define *trace space emittances* as areas in the transverse planes $x - x'$, $y - y'$ and the longitudinal plane $\Delta\phi - \Delta W$ or $z - z'$.

In general terms, beams do not necessarily have properly defined boundaries in 2D phase planes. The definition of an emittance as area (divided by π) within an elliptical boundary in 2D trace space is commonly adopted as shown in Fig. 2.2. It is based on the idea that particles have elliptical trajectories in 2D phase planes in the ideal case of linear forces and time-independent focusing with no acceleration.

2.2.2 *Rms Emittances and Rms Equivalent Beams*

The quality of beams is expressed in an rms sense by making use of the rms size and divergence of a beam in trace space. The rms size $\tilde{x} \equiv \sqrt{\overline{x^2}}$, for example, results from the second order moment of x^2 of the distribution function f in 4D trace space:

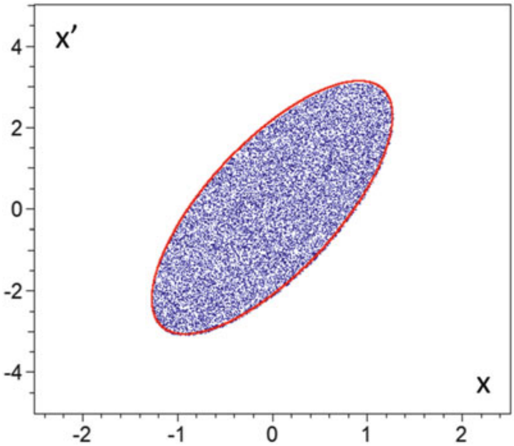

Fig. 2.2 Emittance ellipse of a uniform beam distribution in $x - x'$ phase space

$$\tilde{x}^2 \equiv \overline{x^2} \equiv \frac{\int\int\int\int x^2 f\, dx\, dx'\, dy\, dy'}{\int\int\int\int f\, dx\, dx'\, dy\, dy'}. \tag{2.7}$$

Likewise rms moments are defined in x'^2 and $x x'$, and the rms emittance in the x-plane results as[4]

$$\varepsilon_{x,rms} = 4\sqrt{\overline{x^2}\,\overline{x'^2} - \overline{xx'}^2}, \tag{2.8}$$

with analogous expressions applying to the other phase planes.[5] For an upright ellipse the term $\overline{xx'}^2$ is zero. It stands for the correlation between x and x' in a converging or diverging beam.

Practically important is the concept of "rms equivalence": beams with different distribution functions, but identical intensities and rms moments in all directions of phase space are called "rms equivalent". This concept is based on the validity of the rms envelope equations independent of the shape of a distribution functions. Although this relies on the assumption of constant (normalized) rms emittances (see Sect. 3.2.1), it is a highly useful tool for comparing beams with different distribution functions, which are normally required to be rms equivalent. Examples of rms equivalent waterbag and Gaussian distributions in 4D phase space projected on the $x - x'$-plane are shown in Fig. 2.3.

[4]Note that the factor 4, which is used to make this definition stand for the *full* area (divided by π) of a uniformly populated ellipse, is dropped in some purely rms based conventions.

[5]In the remainder of this book the suffix "rms" is omitted, and ε is understood as rms emittance, unless otherwise explained.

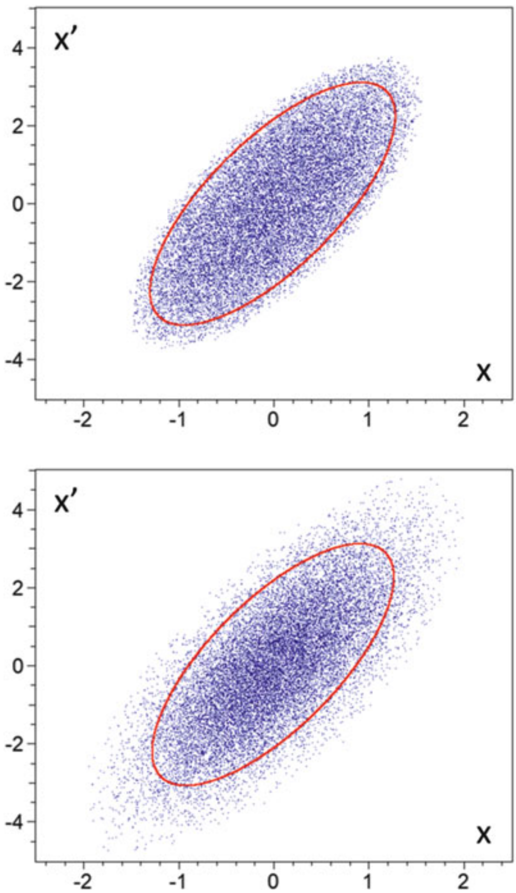

Fig. 2.3 Rms equivalent 4D water bag (*top*) and Gaussian (*bottom*) phase space distributions in $x - x'$, with ellipses showing equivalent KV-boundary as in Fig. 2.2

2.2.3 Anisotropy Factor

Beam anisotropy as a measure for the internal energy balance needs a quantification. A practically useful quantitative measure "T" for the anisotropy between different degrees of freedom can be defined – in non-relativistic approximation and for upright phase space ellipses – as ratio of the rms averaged squared velocity deviations (see Sect. 2.3 as well as Chap. 9):

$$T \equiv \frac{T_x(s)}{T_y(s)} \equiv \frac{\overline{x'^2}}{\overline{y'^2}}, \tag{2.9}$$

and similar for the remaining ratios. Here it is assumed that individual particles are harmonic oscillators, and in this case the ensemble averaged kinetic energy equals the total energy as a special case of the virial theorem.

Note that occasionally "temperature ratios" are proposed, which is misleading. Temperatures cannot be defined properly for beams, which are not in a thermal equilibrium state due to lack of collisions.

2.3 Multiparticle Simulation Effects

Leaving aside the physical intrabeam scattering or various dissipative effects, computer simulation of space charge dominated beams aims at a modelling consistent with the collision-less Vlasov approach. In multi-particle simulation codes this is, however, not rigorously possible. Controlling and minimizing the non-physical effects of numerical discretization becomes an important task. While this is a large field of its own,[6] only a few specific aspects can be discussed here, along with examples from the TRACEWIN code.

2.3.1 Rms Entropy and Simulation Noise

Collision or noise effects can, in principle, be associated with entropy growth. The concept of a probability based entropy in accelerator beams was first discussed in general terms by Lawson et al. in [9]. They introduced it for a time-independent KV-distribution in 4D phase space as

$$S = k \ \ln \ \varepsilon, \tag{2.10}$$

where k is the Boltzmann constant and ε the emittance, which is interpreted here as probability to find particles in a certain volume of phase space.

A significant further step in this direction has been the noise and entropy growth model by Struckmeier in [10, 11]. Starting from Eq. 2.5, Struckmeier kept the Fokker-Planck terms and derived rms equations by calculating the second order moments of the Fokker-Planck equation.[7]

The key point is that a 6D rms emittance can be introduced as product of emittances according to $\varepsilon_{6D} \equiv \varepsilon_x \varepsilon_y \varepsilon_z$, which depends on beam anisotropy (defined in Sect. 2.2.3) and is a growing quantity under the influence of collisions and anisotropy. In analogy to Eq. 2.10 its logarithm can be used to define an entropy "S", and its growth results as:

[6]See, for example, the work by Birdsall and Langdon in [8].

[7]Therein Struckmeier extends significantly the second order procedure by Sacherer in [12], which is limited to the *collision-less* Vlasov equation.

$$\frac{1}{k}\frac{dS}{ds} = \frac{d}{ds}\ln\,\varepsilon_{6D}(s) = \frac{k_f}{3}\,I_A \geq 0.$$

where $s = \beta ct$ measures the distance and $k_f \equiv \beta_f/\beta c\gamma$, with β_f the dynamical friction coefficient, which is proportional to the Coulomb logarithm.[8] The total anisotropy factor I_A measures the deviation from an isotropic beam. It is a positive quantity, which can vary locally in periodic focusing:

$$I_A \equiv \frac{(1-r_{xy})^2}{r_{xy}} + \frac{(1-r_{xz})^2}{r_{xz}} + \frac{(1-r_{yz})^2}{r_{yz}}. \tag{2.11}$$

The r_{nm} are based on the anisotropy factors defined in Sect. 2.2.3, hence $r_{xy}(s) \equiv T_y(s)/T_x(s)$, and similar for the remaining ratios.

Recently, this collision based noise model has been extended in [6] on a phenomenological basis to also include a "grid noise" induced contribution to entropy growth for 3D bunched beams, and in an analogous manner by Boine-Frankenheim et al. in [13] for 2D coasting beams. For the 3D case the respective entropy growth expression is:

$$\frac{\Delta\varepsilon_{6D}}{\varepsilon_{6D}} = \Delta s\frac{k_f^\star}{3}\,(I_A + I_{GN})\,. \tag{2.12}$$

Here, $k_f^\star$ is phenomenologically modified to take into account the additional grid noise effects generated in the simulation. This effect also enters into the offset term I_{GN}, which takes care of the entropy growth found in simulations of isotropic beams, where $I_A = 0$.

2.3.2 Application to TRACEWIN Code

We present examples of noise calculation based on the above theoretical framework from [6], which are obtained with the TRACEWIN code [14]. It is a widely used PIC-code developed primarily for linear accelerators and employed here for most of the simulation examples in periodic focusing lattices in the subsequent chapters. Note that the numerical values of the parameters $k_f^\star$ and I_{GN} are specific to the code under consideration, but the general structure of Eq. 2.12 is applicable to other codes.

The PICNIC space charge routine of TRACEWIN is used with its *rz* and *xyz* Poisson solver options for 3D bunched beams, in later chapters also the 2D *xy* version for coasting beams. PICNIC assumes a grid over the core region of the beam

[8] β_f follows from the friction term in Eq. 2.5; note that in or near equilibrium the friction and diffusion terms in this equation are related to each other via the Einstein relations.

– for example defined up to 3.5σ – and an analytical expression beyond. For our discussion the total number N of simulation particles matters, likewise the number n_c of grid cells, which is counted in each direction from the bunch centre to the core region edge.

Examples from [6] for collision and grid effects for a space charge dominated beam in a periodic focusing symmetrical FODO lattice over 1000 cells, with an rf gap in the centre of each drift space (details see Sect. 7.4.1) are shown in Fig. 2.4. The l.h.s. graph shows the predominantly collisional entropy growth due

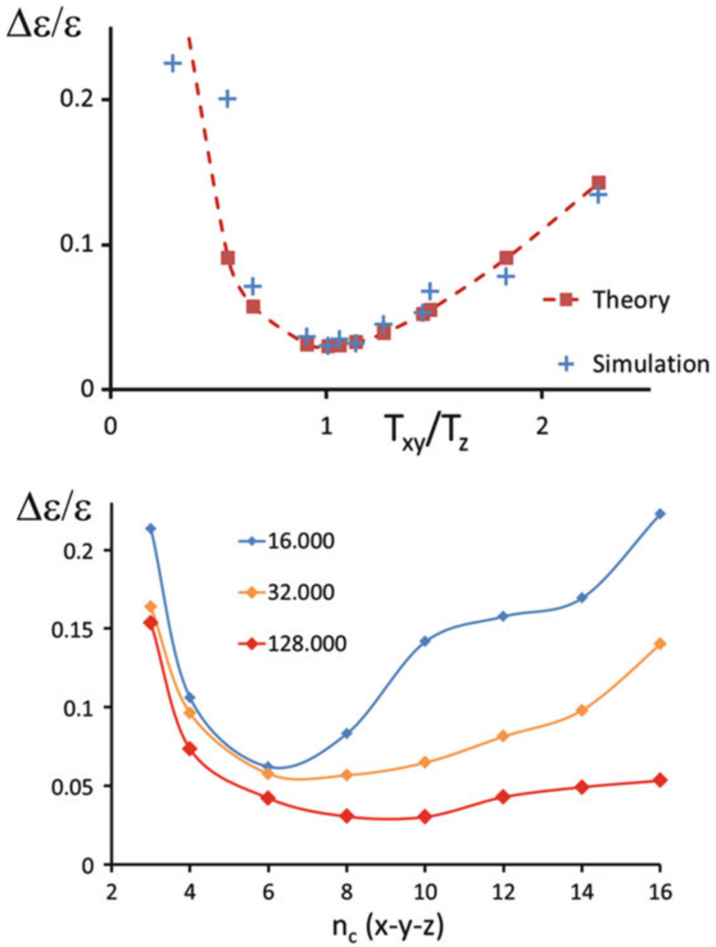

Fig. 2.4 Rms entropy growth over 1000 cells from noise in TRACEWIN computer simulation for a symmetrical FODO lattice. *Top graph*: Relative growth of ε_{6D} with rz Poisson solver in periodic solenoid lattice as function of initial temperature anisotropy in simulation, and comparison with Eq. 2.12; *Bottom graph*: Relative growth of ε_{6D} in FODO lattice for N=16.000/32.000/128.000, as function of the number of grid cells in x, y, z (Source: [6])

to anisotropy for a near spherical bunch with equal zero-current focusing strengths in all directions and anisotropy realized by different emittances. Relatively high grid resolution, $n_c = 16$, is assumed for this case. The collision effect is enhanced independent of anisotropy by choosing a small number of simulation particles, $N = 4000$, hence highly charged simulation macro-particles. These simulation results are compared with the theoretical dependence on anisotropy through I_A in Eq. 2.12, and fitted values of $k_f^\star$ as well as I_{GN}. Good agreement between simulation and theory is obtained.

The r.h.s. graph for isotropic beams, $I_A = 0$, but with variable grid resolution and for different N, demonstrates the existence of two regimes: For small n_c the noise is dominated by the poor grid, and increasing N is not helpful; increasing n_c at small values of N resolves well the collisions of the highly charged simulation macro-particles, and the noise is collision dominated. Increasing N to a sufficiently large value – like the case $N = 128{,}000$ – reduces the charge per macro-particle correspondingly, and collision effects are weakened.

Thus, $n_c = 8 \ldots 10$ and $N > 10^5$ lead to an acceptably low noise level for 3D bunches in high-current linac applications. It should be noted that in the 2D noise simulation study of Ref. [13] the collisional growth of ε_{6D} is found to be significantly more pronounced for high grid resolution – apparently due to the longer range of the Coulomb force in case of interacting charged "rods" in 2D.

A low level of noise is desirable from the point of view of confidence in simulation results. On the other hand, noise plays a role as initial seeding mechanism – besides density or rms mismatch – in unstable situations with exponential growth, like the coherent parametric instabilities in Chap. 7.

References

1. A.A. Vlasov, J. Phys. USSR **9**, 25 (1945)
2. M. Reiser, *Theory and Design of Charged Particle Beams*, 2nd edn. (Wiley, Weinheim, 2008)
3. T.P. Wangler, *RF Linear Accelerators*, 2nd edn. (Wiley, New York, 2008)
4. H. Wiedemann, *Particle Accelerator Physics Part III* (Springer, Berlin/Heidelberg, 2007), p. 335ff
5. J. Struckmeier, Part. Accel. **45**, 229 (1994); also Phys. Rev. E **54**, 830 (1996) and Phys. Rev. ST Accel. Beams **3**, 034202 (2000)
6. I. Hofmann, O. Boine-Frankenheim, Phys. Rev. ST Accel. Beams **17**, 124201 (2014)
7. S.M. Lund, R.C. Davidson, Phys. Plasmas **5**, 3028 (1998)
8. A.B. Langdon, C.K. Birdsall, Phys. Fluids **13**, 2115 (1970) and C.K. Birdsall, A.B. Langdon, *Plasma Physics Via Computer Simulation* (IOP Publishing, Philadelphia, 1991)
9. J.D. Lawson, P.M. Lapostolle, R.L. Gluckstern, Part. Accel. **5**, 61–65 (1973)
10. J. Struckmeier, Phys. Rev. E **54**, 830 (1996)
11. J. Struckmeier, Phys. Rev. ST Accel. Beams **6**, 034202 (2000)
12. F.J. Sacherer, Ph.D. thesis, University of California at Berkeley [UCRL-18454, 1968]
13. O. Boine-Frankenheim, I. Hofmann, J. Struckmeier, S. Appel, Nucl. Inst. Methods Phys. Res. A **770**, 164 (2015)
14. D. Uriot, N. Pichoff, paper MOPWA008, in *Proceedings of IPAC2015*, Richmond, 2015

Chapter 3
Vlasov and Envelope Analysis

Abstract Self-consistent analytical studies based on the Vlasov-Poisson equations play an important role for analysing space charge phenomena and interpreting computer simulation, in spite of the practical limitation to linearised perturbation theory and to special distribution functions – primarily the so-called distribution by Kapchinskij and Vladimirskij. This chapter introduces the required linearization – with emphasis on 2D beams. The role of rms envelope models as second order approximations, often sufficient for layout and first order design of accelerator lattices, but insufficient in the presence of nonlinear forces, is also discussed.

Rms envelope models, which are only second order approximations, are often sufficient for layout and first order design of accelerator lattices. Due to the presence of nonlinear terms in space charge forces as well as in focusing and accelerating fields, self-consistent methods are required on the analytical as well as the simulation side.

The bulk of analytical work on space charge effects is based on the delta-function distribution by Kapchinskij and Vladimirskij in [1], abbreviated as "KV-distribution", but also other distributions have been studied analytically – to a much lesser extent though.

Besides the theoretical insight into the modes of space charge interaction gained by these analytical methods, they are also indispensable for validation and benchmarking of simulation codes. In addition, analytical methods, combined with simulation, are helpful in developing road-maps in parameter space on possible locations of resonances and instabilities and other sources of beam quality degradation.

3.1 Vlasov Techniques

Analytical solution of the Vlasov-Poisson equations in Chap. 2 requires a number of approximations, which limit their applicability to realistic beams. General overviews, also on the field of applications to accelerators, are found, for example, in [2–4].

I. Hofmann, *Space Charge Physics for Particle Accelerators*,
Particle Acceleration and Detection, DOI 10.1007/978-3-319-62157-9_3

An almost inevitable approximation is the linearised perturbation treatment, which has been the basis of practically all self-consistent analytical modelling efforts so far. The restriction to special distribution functions to obtain explicit solutions is another important limitation.

The Vlasov-Poisson equations are nonlinear, since Eqs. 2.1 lead to products of $E_{x,y,z}$ and f in Eq. 2.6. A perturbation ansatz requires an unperturbed equilibrium solution, f_0, and a small perturbation f_1 about it. Practically solving the perturbation problem becomes increasingly complex from 1D to 2D. This is particularly true, if anisotropy is included in the problem, like unequal tunes or emittances in the different planes in 2D.

3.1.1 Linearized 1D Vlasov-Poisson Equations

Historically, the first study of 1D eigenmodes of collective oscillations of a sheet of electrons in a harmonic potential goes back to dePackh in [5] and Ehrman in [6]. They assumed a uniform phase space density, with only surface waves of the incompressible phase space fluid, which was therefore called "waterbag". Subsequently, Sacherer in [7] analysed the transverse collective resonances of a 1D model under the influence of external multipole errors, and in smooth approximation.

In the longitudinal phase space for long bunches, which is not further pursued here, a self-consistent 1D Vlasov analysis was carried out by Neuffer in [8].

3.1.2 Linearized 2D Vlasov-Poisson Equations

Due to its relevance in Chaps. 7 and 9, this case is exemplified here for a 2D coasting beam approximation in constant focusing.

For a time-independent potential a practical equilibrium solution is any function of the unperturbed Hamiltonian (see also Sect. 4.1),

$$H_0 = \frac{1}{2m\gamma}\left(p_x^2 + p_y^2\right) + \frac{1}{2}\left(K_x x^2 + K_y y^2\right) + \frac{q}{m\gamma^3}\Phi_0(x,y), \tag{3.1}$$

with $\Phi_0(x,y)$ the unperturbed space charge potential. H_0 is a constant of motion, and thus $f_0(H_0)$ solves Eq. 2.6. With a small perturbation ansatz we assume $f = f_0(H_0) + f_1(x,y,p_x,p_y,t)$ and $H = H_0 + H_1(x,y,p_x,p_y,t)$ as well as $\dot{\mathbf{p}} = \dot{\mathbf{p}}^{(0)} + \dot{\mathbf{p}}^{(\mathbf{1})}$, with $\dot{\mathbf{p}}^{(\mathbf{1})}$ depending on the perturbed electric field according to Eq. 2.1. The first order perturbation is a solution of the linearised equation

$$\frac{df_1}{dt} = \frac{\partial f_1}{\partial t} + \frac{1}{m\gamma}\left(\mathbf{p}\cdot\nabla_{\mathbf{x}}\right)f_1 + \left(\dot{\mathbf{p}}^{(\mathbf{0})}\cdot\nabla_{\mathbf{p}}\right)f_1 = -\left(\dot{\mathbf{p}}^{(\mathbf{1})}\cdot\nabla_p\right)f_0, \tag{3.2}$$

where $\dot{\mathbf{p}}^{(\mathbf{0})}$ follows from Eqs. 2.1 for the equilibrium solution. Note that the l.h.s. of Eq. 3.2 is the total derivative of f_1 along the unperturbed trajectories. Hence f_1 can be calculated by integrating the r.h.s. along these trajectories, thus following the method of solving a partial differential equation by integration along its characteristics.

A crucial point here is the nature of the unperturbed particle trajectories. In practical terms, the assumption of a KV-distribution $f_0(H_0) \propto \delta\,(H_0 - E_0)$ has two main advantages, which allow explicit solutions:

- It leads to uniform real space density with linear space charge forces in x, y (see Sect. 4.1). Hence, unperturbed trajectories are harmonic oscillators with frequencies independent of amplitude, which makes the integration process of f_1 feasible.
- Eigenmodes of perturbations can be expanded as finite order polynomials in x and y.

The same arguments apply, if the 2D Hamiltonian in Eq. 3.1 can be split into two 1D Hamiltonians, and f_0 is a function of both, which is applied to the case of the anisotropic beam stability in Chap. 9.

Non-KV-distributions, instead, lead to anharmonic oscillators, moreover to the additional complexity of an infinite series expansion in x, y for the eigenmodes of the electric field perturbations.[1]

3.1.3 Application to Periodic Focusing

In periodic focusing the Courant-Snyder formalism can be applied, which uses a linear canonical transformation generating a more general invariant to replace the Hamiltonian [9]. Any function f_0 of this invariant is again an equilibrium solution, and linearisation of the problem with a KV-distribution follows a similar procedure as discussed above for constant focusing. An example of this procedure leading to eigenfrequencies for parametric resonances in periodic focusing is given in [10].

3.1.4 Further Comments

These linearised approaches have been – with few exceptions – limited to KV-distributions for 2D beams, or its longitudinal analogue in 1D long bunches as in [8].

Nonetheless, the value of these perturbation models as guidance for computer simulation under more realistic conditions should not be underestimated. Comparison between theory and simulation shows that in many cases resonance conditions

[1] An example of such an expansion in terms of Legendre polynomials is found in Sect. 5.4.3.

obtained under idealistic KV and small perturbation conditions, like stopband locations and widths, provide useful information to interpret full-scale multi-particle simulation.

3.2 Envelope Equations

The idea of Kapchinskij and Vladimirskij in [1] to describe the envelopes of their distribution function by ordinary differential equations was generalized by Sacherer in [7] to the concept of rms envelope equations, which are applicable to more general distribution functions, and in all three spatial dimensions.

3.2.1 Rms Envelope Equations

The basic idea is to form second order moments from Vlasov's equation, Eq. 2.6, including all possible combinations of x, x' and E_x, and similar in the other planes. Using the definitions in Sect. 2.2.2 and following the procedure by Sacherer one obtains, after eliminating moments with x' and using the definition of the rms emittance, a second order rms envelope equation

$$\frac{d^2\tilde{x}}{ds^2} + \kappa_x(s)\,\tilde{x} - \frac{\epsilon_x^2(s)}{16\tilde{x}^3} - \frac{q}{m\gamma^3 \mathrm{v}^2}\frac{\overline{xE_x}}{\tilde{x}} = 0, \tag{3.3}$$

and similar in y. However, these equation are not a closed set. The time dependence of $\epsilon_x(s)$ is an unknown quantity at this level, and $\overline{xE_x}$ is correlated with higher order moments of Vlasov's equation, if E_x is a nonlinear force. For 2D beams $\overline{xE_x}$ is, however, independent of the actual density as long as it has elliptical symmetry defined as $n(x, y, s) = n\left(x^2/\tilde{x}^2 + y^2/\tilde{y}^2,\, s\right)$. Taking the 2D uniform beam limit for $\overline{xE_x}$ results in

$$\begin{aligned}
\frac{d^2\tilde{x}}{ds^2} + \kappa_x(s)\,\tilde{x} - \frac{\epsilon_x^2(s)}{16\tilde{x}^3} - \frac{K}{2}\frac{1}{\tilde{x}+\tilde{y}} &= 0 \\
\frac{d^2\tilde{y}}{ds^2} + \kappa_y(s)\,\tilde{y} - \frac{\epsilon_y^2(s)}{16\tilde{y}^3} - \frac{K}{2}\frac{1}{\tilde{x}+\tilde{y}} &= 0,
\end{aligned} \tag{3.4}$$

where the generalized perveance is given by $K \equiv \frac{Nq^2}{2\pi\epsilon_0 m\gamma^3 \mathrm{v}^2}$. For elliptical symmetry Eqs. 3.4 are exact, but they require a priori knowledge of the rms emittances. To what extent this is justified must be verified by multi-particle simulation.[2]

[2]For 3D bunched beams similar equations hold, with a suitably modified definition of perveance in [2], which are sufficiently accurate for practical applications.

3.2.2 Smooth Approximation

Periodic focusing in space charge dominated beam dynamics enhances complexity in analytical approaches. For many applications it is useful to approximate the periodical focusing by an assumed constant focusing of the same average strength per meter, hence also phase advance per meter.

Smooth focusing has been used by many authors, for example by Reiser in [2], to derive scaling laws connecting different beam and structure parameters. In Vlasov stability or resonance studies it is used – where acceptable – to approximate the more demanding periodic focusing.

3.2.3 Chernin's Equations

An extension of the second order rms envelope approach to include the linear coupling from skew quadrupole components, combined with space charge, has been derived by Chernin in [11]. The resulting equations are considerably more complex due to the additional coupled moments.

This may at least in part explain why these important equations have found relatively little attention so far, and space charge is hardly considered in linear coupling.[3] An example demonstrating the importance of this interplay is discussed in Sect. 8.2.2.

In the language of the eigenmodes discussed in Chap. 5, this introduces the possibility of "odd" modes with perturbing linear coupling or skew space charge potential terms $\propto xy$. They stand in contrast with the so far discussed "even" envelope modes, where the perturbing space charge potential only has terms x^2 and y^2.

3.2.4 Core-Test-Particle Model

In the context of studies on beam halo formation numerous authors have used a model, where the beam core is approximated by a rigid density profile. Allowing for mismatch of this core by varying rms sizes according to specific envelope eigenmodes, and with an assumed strictly periodical motion, it is a useful tool to explore and visualize resonant effects on test particles seeded in the outside region (for an example see Chap. 6).

One of the drawbacks of using a rigid core model is the lack of self-consistency. It can be serious if non-uniform density profiles and high levels of space charge are used, when self-consistent treatment leads to density profile flattening (see Chap. 4).

[3]More recently, similar equations with linear coupling and skewed space charge terms have been derived in [12, 13] and, with application to a twisted quadrupole channel, in [14].

References

1. I.M. Kapchinskij, *Particle Dynamics in Resonant Linear Accelerators* (Atomizdat, Moscow, 1966). Translated as LANL report LA-TR-80-10 (1980)
2. M. Reiser, *Theory and Design of Charged Particle Beams*, 2nd edn. (Wiley, Weinheim, 2008)
3. H. Wiedemann, *Particle Accelerator Physics Part III* (Springer, Berlin/Heidelberg, 2007), p. 335ff
4. T.P. Wangler, *RF Linear Accelerators*, 2nd edn. (Wiley, New York, 2008)
5. D.C. de Packh, J. Electron. Contr. **13**, 417 (1962)
6. J.B. Ehrman, Plasma Phys. **8**, 377 (1966)
7. F.J. Sacherer, Ph.D. thesis, University of California at Berkeley [UCRL-18454, 1968]
8. D. Neuffer, Part. Accel. **11**, 23 (1980)
9. E.D. Courant, H.S. Snyder, Ann. Phys. **3**, 1–48 (1958)
10. I. Hofmann, L.J. Laslett, L. Smith, I. Haber, Part. Accel. **13**, 145 (1983)
11. D. Chernin, Part. Accel. **24**, 29 (1988)
12. M. Chung, H. Qin, E.P. Gilson, R.C. Davidson, Phys. Plasmas **20**, 083121 (2013)
13. H. Qin, R.C. Davidson, Phys. Rev. Lett. **110**, 064803 (2013)
14. A. Goswami, P. Sing Babu, V.S. Panditc, Eur. Phys. J. Plus **131**, 393 (2016)

Chapter 4
Matched Beams

Abstract The basis for applying resonance and instability theory to beams, in particular with perturbation approaches, is the existence of a sufficiently well-defined initial "matched beam" solution. In constant focusing this could be a wide class of time-independent distribution functions of the Hamiltonian, which has to include the self-consistent space charge potential with its shielding properties. In periodic focusing a matched beam is ideally a solution that follows exactly the focusing periodicity. With nonlinear space charge forces – for non-KV-distributions – this is, however, not rigorously possible. This chapter introduces specific beam distribution functions, their nonlinear space charge forces and "shielding effects". Examples of "incoherent resonance" effects in matched beams are presented.

4.1 Distribution Functions and Their Properties

For a given beam dynamics study an adequate choice of initial distributions in 4D or 6D phase space is an non-trivial task. For analytical studies on space charge the KV-distribution in 4D phase space is frequently used as a starting point, in particular for circulating beams or long bunches in circular accelerators. It has played an important role in laying the ground for analytical perturbation theory. Comparison with waterbag and Gaussian or other models as a next step is largely left to computer simulation – see Chap. 7 for examples on this subject.

For constant focusing, and in 2D, the KV-distribution is written as delta-function

$$f_0(H_0) \propto \delta\,(H_0 - E_0)\,. \tag{4.1}$$

The Hamiltonian H_0 describes harmonic oscillators in a quadratic total potential including external focusing and space charge defocusing, where particles only populate the surface of a hyper-ellipsoid in 4D phase space given by a specific value of the total energy, $H_0 = E_0$. Projections onto 2D sub-spaces, obtained by

I. Hofmann, *Space Charge Physics for Particle Accelerators*,
Particle Acceleration and Detection, DOI 10.1007/978-3-319-62157-9_4

integration over momentum space, are uniform inside an elliptical boundary (for details on orbits etc. see Sect. 5.3.2; also, for example, in [1]):

$$\left(\frac{x}{a}\right)^2 + \left(\frac{y}{b}\right)^2 \leq 1, \tag{4.2}$$

with semiaxes a and b. This results in electric fields linear inside the boundary

$$\begin{aligned} E_x &= -\frac{qNx}{\varepsilon_0 \pi a(a+b)} \\ E_y &= -\frac{qNy}{\varepsilon_0 \pi b(a+b)}, \end{aligned} \tag{4.3}$$

with N the number of particles per unit length, and a quadratic space charge potential, which is part of the total harmonic oscillator potential in H_0.

Analytical studies using KV-distributions as starting point benefit from the fact that initially all particles are harmonic oscillators with the same oscillation frequency. It is not surprising that the absence of mixing by different particle frequencies leads to a significantly more coherent picture of response whenever perturbations of the initial beam are introduced. This is a well-known result from a wealth of computer simulation studies, where KV-distributions are compared with non-KV distributions.

Alternatively to the KV-distribution we focus on waterbag and Gaussian distributions in simulations of the subsequent chapters. Accelerator theorists that come from a "low-current culture" have a particular affection for a Gaussian distribution because in equilibrium – contrary to the KV-distribution – it is uncorrelated in the various dimensions; however, high levels of space charge potential or instabilities eventually establish correlations and change the nature of the distribution.

For the Gaussian it is assumed that

$$f_0(H_0) \propto \exp\left(-\frac{H_0}{E_0}\right), \tag{4.4}$$

where E_0 is chosen such that the rms radius of the beam is matched. Also truncated Gaussian distributions will be used, where tails are cut off some rms radii away from the centre.

The waterbag distribution is defined by the Heaviside stepfunction,

$$f_0(H_0) \propto \Theta\left(E_0 - H_0\right), \tag{4.5}$$

hence $f_0(H) = const.$ for $0 \leq H_0 \leq E_0$, and $f_0(H) = 0$ for $E_0 < H_0$. Particles populate the interior of the 4D hyper-surface given by $H_0 = E_0$ uniformly, which is also generalized to the 6D waterbag distributions used in some of our simulation examples.[1]

4.2 Linear and Nonlinear Space Charge Forces

For an axisymmetric coasting beam KV-distribution the space charge force is linear inside, and falls off $\propto 1/r$ in the outside region. In Fig. 4.1 we compare the KV-beam with rms equivalent (see Sect. 2.2.2) axisymmetric waterbag and Gaussian distributions beams. The corresponding densities are shown in the top graph; the bottom graph presents electric fields, which are calculated under the assumption of small space charge effects, otherwise the space charge shielding effect must be taken into account (see Sect. 4.3). On axis the rms equivalent Gaussian beam density

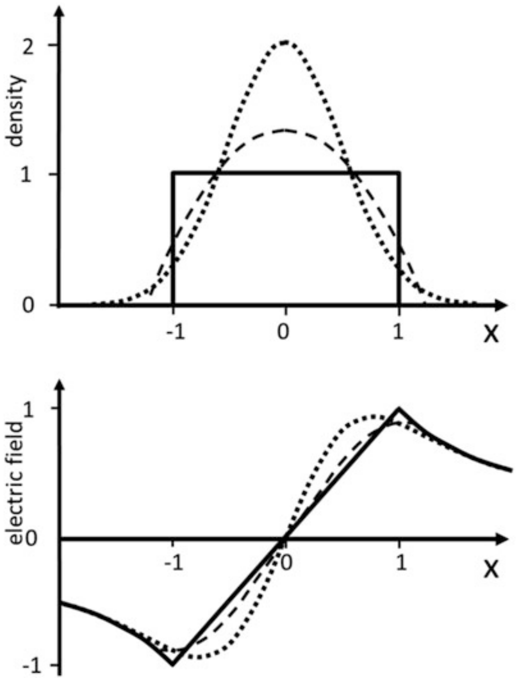

Fig. 4.1 Charge density profiles (*top graph*) and radial electric fields (*bottom graph*) (both in units of maximum values of KV-beam), versus distance from axis (in units of KV-beam radius) for rms equivalent axi-symmetric coasting beams with KV (*continuous lines*), waterbag (*dashed lines*) and Gaussian (*dotted lines*) distributions

[1]In TRACEWIN this energy surface is approximated by ignoring the nonlinear part of the space charge potential, see also Sect. 4.3.2.

is twice that of the uniform KV-beam, which explains the also doubled gradient of the electric field.[2]

Different methods have been proposed to compensate the nonlinear part of the space charge force to reduce its degrading effect on beam quality, which cannot be discussed in detail here. Batygin et al., for example, have demonstrated in [2] by simulation that adding compensating external multipoles (duodecapoles) for this purpose helps reducing rms emittance growth and halo formation in straight transport systems with strong tune depression as in high intensity linacs. Their role is to weaken the nonlinear component of the space charge force, which in practice is not matched and may lead to the emittance growth described in Sect. 6.3.

For circular high intensity proton accelerators or colliders electron lenses for compensation of space charge effects have been successfully considered – for a review see Shiltsev in [3].

4.3 Selfconsistent Non-KV Equilibria

For coasting beams in constant focusing any particle distribution $f(H)$ of the Hamiltonian H in the 4D phase space is a matched, stationary equilibrium solution if H, including the self-consistent and in general nonlinear potential from space charge, is time-independent. The resulting beam models are "equipartitioned" in the sense that ensemble averages of oscillation energies in the different degrees of freedom are identical. This also means $T = 1$ in the rms condition of Eq. 2.9. Formally speaking, an infinite variety of such "equipartitioned" and exactly stationary solutions exists in constant focusing.

4.3.1 Anisotropic Beams

Real beams in circular accelerators are practically always anisotropic or non-equipartitioned – with $T \neq 1$ following the definition in Sect. 2.2.3 – in the transverse plane due to either different emittances or focusing strengths in the horizontal or vertical direction. In linear accelerators the two transverse directions are usually assumed isotropic – $T = 1$ – due to equal production emittances and symmetric focusing strengths. This is normally not the case for the longitudinal and transverse degrees of freedom, except for particular "equipartitioned designs" (see also Chap. 9).

Exact equilibria for non-equipartitioned or anisotropic beams – with $T \neq 1$ – would require knowledge of an additional constant of motion, which can only exist under very exceptional assumptions. A special and practically useful case is a 2D

[2]See also the doubling of the single particle tune shift of small amplitude particles compared with the rms or KV-beam tune shift for example in Fig. 5.15 in Chap. 5.

continuous and uniformly charged beam, where the individual Hamiltonians in x and y are decoupled, and anisotropy is easily realized by means of the parameter T. Such an anisotropic KV-distribution is defined in Sect. 5.3.2 of the next chapter as starting point for theoretical studies of anisotropic beams. In the special case of $T = 1$ the standard KV-distribution is retrieved.

For relatively weak space charge – compared with the focusing strength – as in circular accelerators the matter of self-consistent distributions is not a critical subject. In most cases it is sufficient to define separate, uncorrelated distributions and ignore the coupling terms in the space charge potential. On a much longer time scale – compared with space charge effects – intrabeam scattering can be an issue influencing correlations and anisotropy, which is beyond the framework of this book.

4.3.2 Shielding by Space Charge

Another aspect of self-consistency is "space charge shielding", which is primarily of interest whenever the space charge defocusing forces are not small compared with the average focusing force as in high intensity linear accelerators. For non-KV distributions, like waterbag or Gaussian, a reduction of the emittance to zero – by $\nu/\nu_0 \rightarrow 0$ while maintaining rms equivalence – would lead to a complete cancellation – shielding – of the external focusing force by the space charge force. The density profiles of Fig. 4.1 – calculated ignoring this shielding – become increasingly flatter for lower values of ν/ν_0 due to this shielding, until they reach the shape of the uniform KV-beam at the absolute space charge limit $\nu/\nu_0 = 0$. This phenomenon is the same as the well-known Debye-shielding of a test charge in a neutral plasma, see also in [1]. To give an example, following [1], the peak density in Fig. 4.1 is reduced from 2 to 1.89 for $\nu/\nu_0 = 0.93$, and from 2 to 1.04 for $\nu/\nu_0 = 0.2$, which is almost flat.

For 2D and 3D Gaussian beams in constant focusing, approximate analytical expressions for this shielding have been obtained in [4] in the limit of $\nu/\nu_0 \ll 1$ by a series expansion in the total potential – noting that the total potential vanishes for $\nu/\nu_0 \rightarrow 0$ – and keeping the first order term. The resulting shielded density profiles are shown in Fig. 4.2 for $\nu/\nu_0 = 0.1/0.25$, with radii normalized to the beam edge radius a. The profiles are uniform everywhere, except for a boundary sheath[3] of a thickness given by the "Debye shielding length" λ_D, which is defined here in analogy with the well-known definition in plasmas:

$$\lambda_D^2 \equiv \frac{\overline{x'^2}}{\omega_p^2}. \tag{4.6}$$

[3]Note that the sharp boundary edge of the density profile in Fig. 4.2 for $r/a = 1$ is incorrect as the series expansion of the total potential fails at the edge.

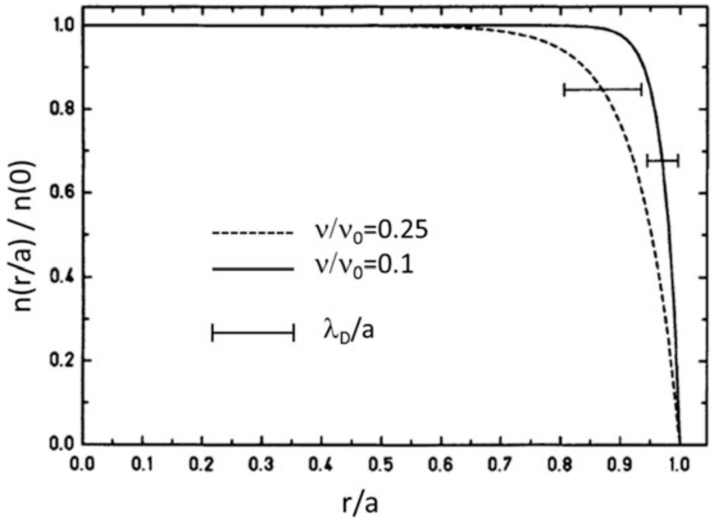

Fig. 4.2 Self-consistent radial density profiles for a spherical bunch with Gaussian distribution function and approximated "Debye shielding lengths" λ_D for $\nu/\nu_0 = 0.1/0.25$

The squared plasma frequency – here in the beam centre and in units of m^{-2} – follows the definition:

$$\omega_p^2 \equiv \frac{q^2 n(0)}{\varepsilon_0 m \gamma^3 \beta^2 c^2}, \tag{4.7}$$

where $n(0)$ is the density on axis. This results – with details in [4] – in a normalized Debye shielding length

$$\frac{\lambda_D}{a} = \frac{1}{\sqrt{n}} \frac{\nu}{\nu_0}, \tag{4.8}$$

with $n = 8$ in 2D and $n = 15$ in 3D.

Hence, this shielding effect is significant for strong tune depression as in very high intensity linear accelerators; in circular accelerators, where $\nu \approx \nu_0$, Eq. 4.8 is invalid. The then appropriate series expansion shows that $\lambda_D/a \gg 1$, hence the shielding effect is negligible.

Thus, for significant tune depression, a fully self-consistent solution requires including the density flattening effect of space charge in the initial distribution. In many computer simulation codes, as in TRACEWIN, this is ignored, and the phase space distribution is set up with the low-intensity space charge potential profile. The lack of this self-consistency is the origin of the "density mismatch" or "nonlinear field energy" emittance growth discussed in Sect. 6.3.

4.3.3 Periodic Focusing

In periodic focusing the situation is more complex. It is accepted – for which no proof exists – that a rigorously periodic equilibrium solution can be realized only with a continuous 2D KV-beam, including the generalization with anisotropy. Depending on intensity, KV-beams are, however, not stable over extended distances as will be discussed in Sect. 7.3.2.

Struckmeier et al. in [5] have suggested that non-KV distributions matched in constant focusing can be transformed "locally" into a quasi-periodic stationary equilibrium of a periodic focusing lattice. "Locally" implies an infinitesimal canonical transformation transforming the constant focusing solution into a periodic focusing one. According to transport simulations, the thus obtained "quasi-matched" equilibria are highly emittance conserving for weak space charge as in circular accelerators. For stronger tune depression as in high current linear accelerators, there is still excellent emittance conservation in periodic solenoid focusing; in alternating gradient focusing a small, but continuing emittance growth is found.

4.4 Incoherent Space Charge Effects on Resonances

The notion of "incoherent" space charge effects assumes a matched equilibrium beam, which is time-independent in constant focusing; or, in periodic focusing, a "quasi-matched" beam should follow to high accuracy the lattice periodicity.

4.4.1 Incoherent Space Charge Tune Shifts

The effect of uniform density – as in a 2D KV-beam – is to shift the oscillation frequencies[4] of individual particles independent of their amplitude, which causes an "incoherent tune shift".[5] Nonuniform density leads to nonlinear space charge forces, and the resulting amplitude dependence causes a "tune spread".[6]

[4] In the following also called "tunes" as number of oscillation periods per circumference in circular accelerators; in linear accelerators also called "phase advance" in degrees per lattice period.

[5] To be distinguished from the "coherent tune shift" discussed in the following chapters.

[6] This spread is also called "incoherent tune shift" in literature, but we prefer referring to it as tune spread.

With the linear space charge forces of Eqs. 4.3 and Eqs. 2.1 we write the space charge shifted tunes for the resulting single particle harmonic oscillators in 2D as:

$$\nu_x^2 = \nu_{0x}^2 - \frac{q^2 N}{\varepsilon_0 \pi m \gamma^3 a(a+b)}$$
$$\nu_y^2 = \nu_{0y}^2 - \frac{q^2 N}{\varepsilon_0 \pi m \gamma^3 b(a+b)}, \tag{4.9}$$

with $\nu_{0x}^2 \equiv K_x$, $\nu_{0y}^2 \equiv K_y$ the (squared) zero current single particle frequencies. Note that the incoherent tune shift drops with higher energy and increasing relativistic γ-factor.[7]

For a discussion of further types of density distribution and related electric field distributions see, for example, in [1]. For the analogous tune shift expressions in 3D short bunches relevant to linear accelerators see also in [6].

4.4.2 Structural Incoherent Space Charge Resonances

Both, the incoherent space charge tune shifts as well as spreads, are an important ingredient for nonlinear dynamics studies of beams in circular accelerators, where magnet nonlinearities are the primary driving source of resonances.

However, also space charge itself can be the driving force of resonances. A well-matched (or quasi-matched) equilibrium beam generates a space charge potential modulated according to the lattice structure. For a symmetrical Gaussian beam, for example, the space charge potential in the beam core can be expanded in a power series, which includes all terms of even order – frequently called space charge "pseudo-multipoles" in analogy with the multipole terms from magnets.

Such "structural" space charge driven resonances follow formally the same resonance condition as commonly used in the presence of magnetic field multipoles in circular accelerators[8]:

$$l\nu_x + m\nu_y = Nh, \tag{4.10}$$

where $l + m$ determines the order of the resonance, N stands for the number of lattice periods, respectively super periods, and $h > 1$ describes higher harmonics of the fundamental lattice period. Assuming that coherent effects are absent it is appropriate to call it incoherent or single particle resonance – driven by the structural space charge effects due to the matched equilibrium beam.

---

[7]The reduction is $\propto 1/\gamma^2$, if the reduction of the beam cross section $\propto 1/\gamma$ is taken into account.

[8]Note that nonlinear fields from magnets grow with the distance from axis; whereas the space charge field drops outside the beam core, which requires different expansions.

In linear accelerator notation the equivalent expression is

$$lk_{0x} + mk_{0y} = 360^\circ h, \tag{4.11}$$

with $h > 1$ describing higher harmonics of the focussing cell. As an example, for $l = m = 2$ as well as $h = 1$, this $4k_{x,y} = 360°$ resonance is discussed in linear accelerators as "fourth order space charge resonance" – also called 90° resonance. It is often assumed to be an incoherent – or single particle – resonance phenomenon assuming that coherent effects are absent.[9] However, a strict separation of space charge incoherent and coherent resonance effects is often not possible. It depends on the type of distribution function and is more likely to be justified for Gaussian than for waterbag distributions.

4.4.3 Simulation Examples

We first present an example of the fourth order structural incoherent space charge resonance obtained with a TRACEWIN simulation of a 3D near-spherical bunch in a periodic FODO lattice as described in Sect. 7.4.1. A Gaussian distribution (truncated at 3σ, with 128,000 simulation particles) is used. In this example it is assumed that the zero current transverse phase advance, $k_{0,x,y}$, is slowly changed from 100° to 90° by a tune ramp linear in time over 500 cells.[10] The initial space charge depressed rms values of tunes are $k_{x,y} = 92.2°$ (assuming equal emittances in x and y), hence still above the resonance condition.

Phase space plots in Fig. 4.3 taken at different cells show the progressive effect of the resonance. The frame at 500 cells indicates trapping of particles in the four islands of the resonance while the islands are pushed far away from the centre. It should be noted that the broad spectrum of single particle phase advances for a Gaussian is such that smaller amplitude particles are on resonance from the beginning, while other particles with large amplitude reach the resonance only towards the end of the tune ramp.

Emittance and rms envelope results of the approach to the space charge structure resonance are shown in Fig. 4.4. The dynamical tune change is slow enough to maintain good matching of the beam to the lattice at every instant as is evidenced by the smoothly (adiabatically) changing envelope. At the same time the – also smooth

[9] As shown in [7], early particle-in-cell simulations already gave evidence that this fourth order space charge resonance may occur in company with the so-called envelope instability; for a more recent discussion of such combined effects see also [8] and Sect. 7.5.

[10] Note that this particular resonance phenomenon would be also observable in the transverse phase space in a circular accelerator – apart from a possibly different influence of synchrotron motion – if the 90° were approached from above. This could be achieved, for example, by a fast bunch rotation and an associated reduction in $\nu_{x,y}$.

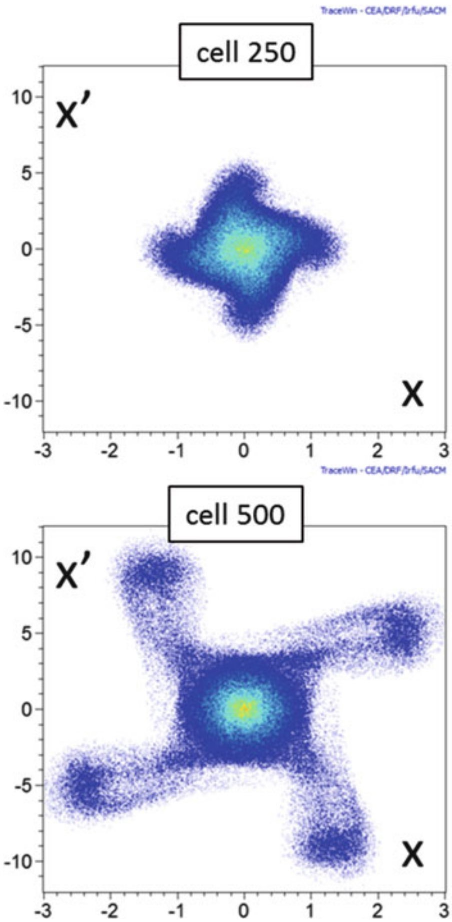

Fig. 4.3 Fourth order structural incoherent space charge resonance for dynamical tune ramp of $k_{0,x,y} = 100° \rightarrow 90°$ over 500 cells. Shown are phase space plots in $x - x'$ for cell numbers 250 (*top frame*) and 500 (*bottom frame*)

– growth of transverse rms emittances – identical in x and y – indicates the effect of the approach to the resonance.

The finding of trapped particles in the resonance islands is also reflected by the evolution of phase advance as shown in Fig. 4.5. In the absence of the resonant effect the phase advance would be space charge depressed to approximately 83° at the end of the ramp, but the presence of the resonance blocks it at about 89°, while the trapped particles gain in amplitude. This is a typical self-consistent space charge phenomenon, where decreasing charge density compensates for the enforced reduction of the zero-intensity phase advance. Note that at all phases of this tune ramp the beam remains well-matched with the lattice and follows its periodicity, which justifies the notion of incoherent resonance.

Also higher harmonics $h > 1$ of the fundamental lattice period need to be considered. An example of such a case for a 3D Gaussian bunched beam simulation in a FODO lattice is found in [9] and shown in Fig. 4.6: With a slow dynamical tune

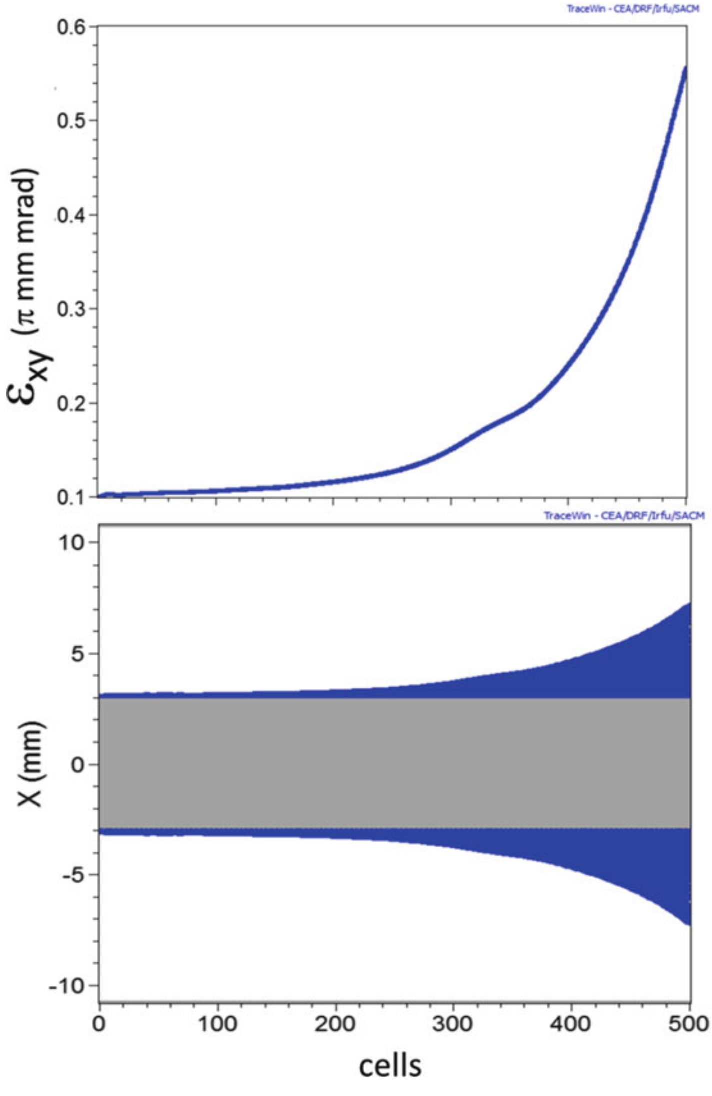

Fig. 4.4 Tune ramp of $k_{0,x,y} = 100° \rightarrow 90°$ over 500 cells as in case of Fig. 4.3. Shown are transverse rms emittances (*top frame*) and beam envelopes in x (*bottom frame*), both as function of cells

ramp for $k_{0,x,y}$ from $150° \rightarrow 130°$ a sequence of structure resonances of the type $mk_{x,y} = 360°h$ was found: a 10th order for $k_{x,y} = 144°$ and $h = 4$; an 8th order for $k_{x,y} = 135°$ and $h = 3$; and a 6th order for $k_{x,y} = 120°$ and $h = 2$. With the space charge pseudo-multipoles as driving terms it must be kept in mind that – in contrast with magnet multipoles – they are strong in the beam core, but their strength drops with increasing distance from the beam, which limits their effect.

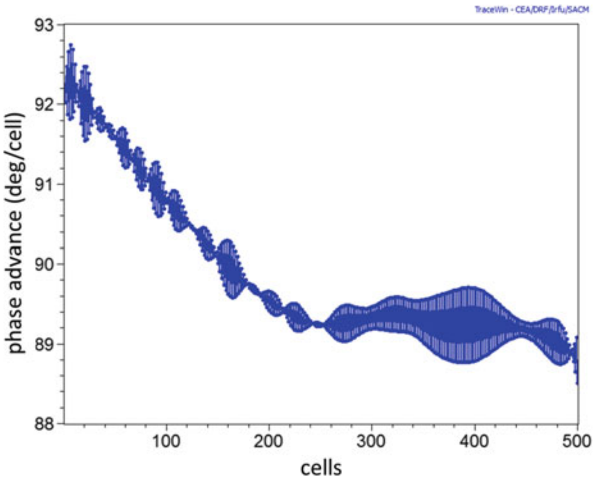

Fig. 4.5 Phase advance (including space charge) for the case of Fig. 4.4

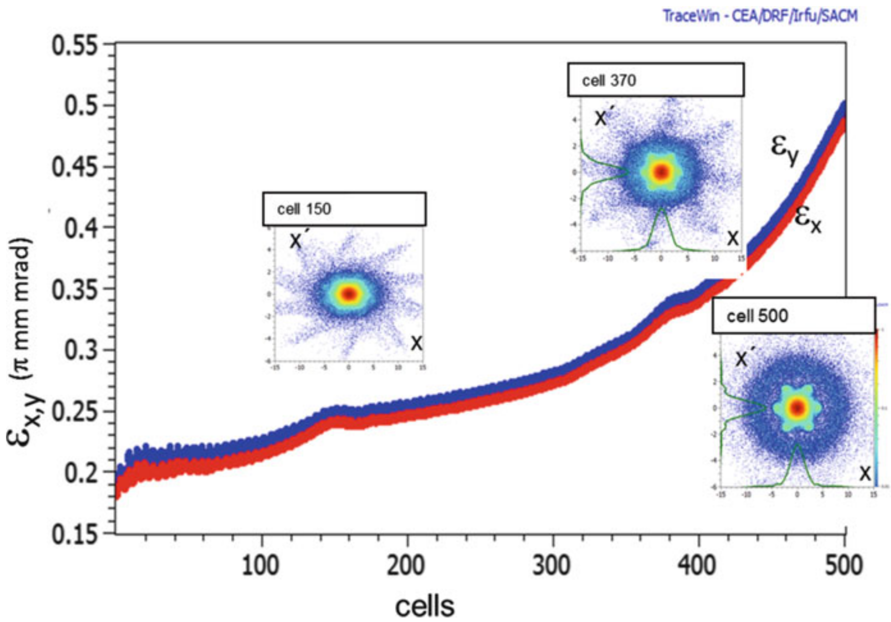

Fig. 4.6 Structural incoherent resonances driven by higher order harmonics of the lattice period for a dynamical tune ramp of $k_{0,x,y} = 150° \rightarrow 130°$ over 500 cells. Shown are transverse rms emittances and inserts with phase space plots at different cells

References

1. M. Reiser, *Theory and Design of Charged Particle Beams*, 2nd edn. (Wiley, Weinheim, 2008)
2. Y.K. Batygin, A. Scheinker, S. Kurennoy, Chao Li, Nucl. Instrum. Meth. **A816**, 78 (2016)
3. V.D. Shiltsev, Electron lenses for space-charge compensation, in *Electron Lenses for Super-Colliders*. Springer Series Particle Acceleration and Detection (Springer, Berlin/Heidelberg, 2015)
4. I. Hofmann, J. Struckmeier, Part. Accel. **21**, 69 (1987)
5. J. Struckmeier, I. Hofmann, Part. Accel. **39**, 219 (1992)
6. T.P. Wangler, *RF Linear Accelerators*, 2nd edn. (Wiley, New York, 2008)
7. I. Hofmann, Transport and focusing of high intensity unneutralized beams, in *Applied Charged Particle Optics*. Supplement 13C of Advances in Electronics and Electron Physics, ed. by A. Septier (Academic Press, New York, 1983), p. 49ff
8. I. Hofmann, O. Boine-Frankenheim, Phys. Rev. Lett. **115**, 204802 (2015)
9. I. Hofmann, 57th ICFA beam dynamics workshop HB2016, Malmoe, 3–8 July 2016, paper THPM1X01 (2016)

Chapter 5
Modes of Space Charge Interaction

Abstract The incoherent space charge effects discussed in the previous chapter are connected with matched beams, e.g. beams in – or nearly in – "equilibrium" with the focusing lattice. Beams deviating from such a matched state – for various reasons – are a source of coherent space charge effects. This chapter is dedicated to the diverse causes of coherent motion – from mismatch to instability – and a discussion of their characteristic properties. The linearised analytical Vlasov approach in constant focusing approximation is used to derive eigenmodes of coherent motion in different orders and including anisotropy, which are helpful to gain theoretical insight into the modes of space charge interaction. The concept of "negative energy modes" – analogous to the well-known "negative energy waves" of plasma streams – is introduced to characterize unstable behaviour, and the relevance of Landau damping of these modes examined by using simulation examples.

5.1 Characteristics of Space Charge Interaction

There are several mechanisms by which space direct space charge interaction may lead to beam degradation and emittance growth, and a variety of characteristic features is associated with them. Besides their spatial configuration, they can be distinguished by the nature of the mechanism, which leads to growth, and by the source of energy driving it.

5.1.1 Mechanisms of Growth

It is helpful to distinguish between three principal processes leading to changing amplitudes and emittances, which are shown symbolically in Fig. 5.1. The idea of this chart is to characterize types of interaction with the total potential, which consists of the applied one from constant or periodic focusing *and* the space charge potential.

Thus, the "potential well" stands symbolically for the total potential in a matched "equilibrium" state, while the sphere represents the beam with its space charge mode of perturbation. We distinguish between:

I. Hofmann, *Space Charge Physics for Particle Accelerators*,
Particle Acceleration and Detection, DOI 10.1007/978-3-319-62157-9_5

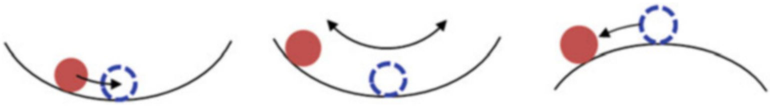

Fig. 5.1 Symbolic representation of mismatch (*left*), resonance (*center*) and instability (*right*) as principal processes responsible for emittance growth. The potential well stands for the combined potential from external forces and internal space charge forces; the sphere symbolizes a space charge mode of perturbation

- Mismatch (left graph): Here it is assumed that a stable periodic (or nearly periodic) equilibrium solution exists; perturbing it by either a focusing or defocusing kick, or by a not well-matched density profile, results in oscillations around the initial state or a new density profile. Such oscillations are usually damped – depending on the distribution function – and lead to "heating" or emittance growth of the equilibrium (see Chap. 6).
- Resonance (centre graph): Single particles or a coherent mode of an otherwise matched and stable equilibrium beam experience a periodic kick from an external magnetic field multipole, or from the periodically modulated space charge (structure resonances). Growing amplitudes result, but de-tuning effects limit the growth.
- Instability (right graph): A periodic (or nearly periodic) equilibrium solution exists in principle, but it is not stable: a small deviation – even by an infinitesimal presence of a space charge eigenmode in the initial beam – results in an exponential runaway situation due to a feedback of the perturbed charge density on the motion.

In the context of beams controlled by direct space charge – ignoring here impedance effects due to the surrounding media – instabilities are practically always tied to resonance conditions. In periodic focusing they are driven as coherent parametric resonances (Chap. 7), but also anisotropy driven resonant instabilities exist (Chap. 9). One example of *non-resonant* instabilities of mainly academic interest are the "Gluckstern-modes" called intrinsic instabilities of KV-distributions (see Sect. 7.3.2.3).

There are situations, where the above listed mechanisms are mixed or overlap with single particle phenomena. For example, mismatch may result in a periodic (or nearly periodic) coherent space charge force; as a result, single particles are driven resonantly to larger amplitudes and contribute to the beam halo (Sect. 6.1.1).

5.1.2 Sources of Driving Energy

Amplitude and emittance growth processes can also be characterized by the driving energy sources. Under the assumption of perfectly conducting boundaries, or open space boundaries conditions, the following sources are available:

- The electrostatic field energy connected with the charge density: forming a beam of a given profile needs energy to overcome Coulomb repulsion; changing the density profile may release part of this energy and drive emittance growth as well as change anisotropy, which is a fast and non-resonant process (see Sects. 6.1.1 and 6.3).
- The resonant amplitude growth of particles driven by a magnetic field multipole, or the force from the periodically modulated beam space charge (a space charge structure resonance): directional energy from the forward (or circulating) beam motion is coupled into the transverse direction; and in case of a longitudinal resonance into the longitudinal motion.
- For parametric resonances in periodic focusing systems – normally also structure resonances – a similar transfer from the forward (or circulating) motion occurs.
- Anisotropy, where different rms emittances and/or focusing strengths can give rise to a resonant transfer of oscillation energy from one plane to another.

5.2 Incoherent vs. Coherent Oscillations

A subject of central importance in the theory of space charge – more elaborated in Chap. 7 and following chapters – is the distinction between incoherent and coherent space charge effects. What is the meaning of coherent modes of oscillation or resonances in the context of space charge dominated beams, and what is their effect compared with incoherent space charge effects?

The difference between an incoherent and a coherent gradient error resonance was first recognized by Smith in [1]. Smith had pointed out that what matters for the resonance behaviour is the combined force from the external gradient error and the extra space charge force due to the coherent response. The latter shifts the condition of resonance – in favour of a higher intensity threshold (see Sect. 8).

5.2.1 Characteristics of Coherent Oscillations

Incoherent oscillations are understood as features of single particles in a matched equilibrium distribution, which may change slowly in case of a single particle resonance. Coherent oscillations are usually rapidly evolving changes of density. As such they are related to specific frequencies, which are not present in the matched equilibrium solution; this includes, for example, betatron frequencies, lattice periodicities and their harmonics or sub-harmonics, as well as the internal "beam plasma frequency", or combinations of some of them.

A sharp distinction coherent-incoherent is not always possible and depends on the actual distribution function, the type of resonance and other factors. The coasting beam KV-distribution, for example, always responds in a clearly coherent fashion to any kind of perturbation or resonance of arbitrary order. This is due to the fact that

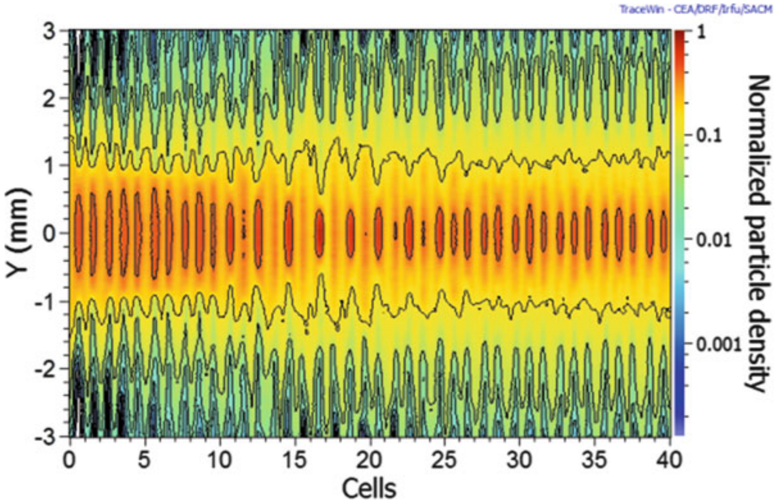

Fig. 5.2 Incoherent and coherent patterns of y-density evolution of a nearly spherical bunch within the 90° stopband. The bunch is exposed to a space charge driven structure resonance (incoherent) on the one hand, and an envelope instability (coherent) on the other hand. Shown are density levels graphically enhanced by contour lines over 40 periodic lattice cells (TRACEWIN 3D PIC simulation)

no frequency spread exists in the equilibrium beam, which will be discussed further in Sect. 7.2. Gaussian distributions have a tendency to wash out coherent density modulations due to their intrinsic frequency spread from the nonlinear space charge potential – but not always.

5.2.2 Simulation Example

To illustrate the significance of *coherent* and *incoherent* we show in Fig. 5.2 a real space density plot of an initially well-matched nearly spherical bunched beam. It is located inside the 90° stopband of a periodic lattice and modelled by a 3D TRACEWIN simulation (for details see Chap. 7). The plot shows the transverse density integrated over z and x for an initial waterbag distribution. The initial pattern up to about 10 cells reflects the equilibrium density modulation matched to the periodical lattice. Although there is already a gentle effect from a fourth order space charge driven structure resonance (Sects. 4.4.2 and 7.5) the resonant response remains incoherent and conserves the matched beam density pattern. Beyond cell 10, however, an envelope instability develops within few cells and results in a strongly coherent density modulation. Rather than following the initial lattice periodicity, the coherent pattern requires two cells to perform one period.[1] Beyond cell 25 the intrinsic mixing effects turn the coherent pattern gradually back into an incoherent pattern of the beam density, which is again well-matched to the lattice.

5.3 Vlasov Theory of Coherent Eigenmodes in Anisotropic 2D Beams

Coherent eigenmodes play an important role in the description of parametric instabilities, which are introduced in Chap. 7; they also occur – at least in second order – in the context of the magnet error driven resonances of Chap. 8. We therefore outline here their derivation from Vlasov's equation, under the assumption of anisotropic beams in two dimensions, and of constant focusing.[2]

Although the analytical method employed here is specific to KV-distributions, it provides useful insight into the structure of these coherent modes and forms the basis of further discussions and applications. Furthermore, the two dimensions are normally understood as the two transverse dimensions x and y of an infinitely long beam. For certain applications, like transverse-longitudinal anisotropy of short linac bunches in Chap. 9, it is useful to interpret one of the two dimensions as longitudinal coordinate, and the other one as transverse. Taking the remaining transverse dimension infinite is an approximation, which needs to be kept in mind, however.

5.3.1 Modes of Different Order

The envelope mode encountered in Fig. 5.2 is a second order mode of coherent oscillation. For the more general mode picture we assume a uniform density elliptical cross section and consider small deformations of the boundary with azimuthal harmonics $l = 2, 3, 4$ as shown in Fig. 5.3, where $l = 2$ relates to second order and so forth.[3] The distinction between *even* and *odd*, where "odd" stands for rotation or "tilting" in real space, and "even" for the absence of it is only meaningful in a non-rotationally symmetric beam situation. The second order even modes are solutions of the envelope equations, which cannot describe spatially tilted modes.

[1]This is an example of 1:2 coherent parametric instability discussed in more detail in Chap. 7.

[2]A generalization to periodic focusing for 2D beams with anisotropic effects is not available in the literature.

[3]In our space charge context we disregard $l = 1$ as usual dipole or displacement mode as it does not lead to a change of space charge density (ignoring image effects).

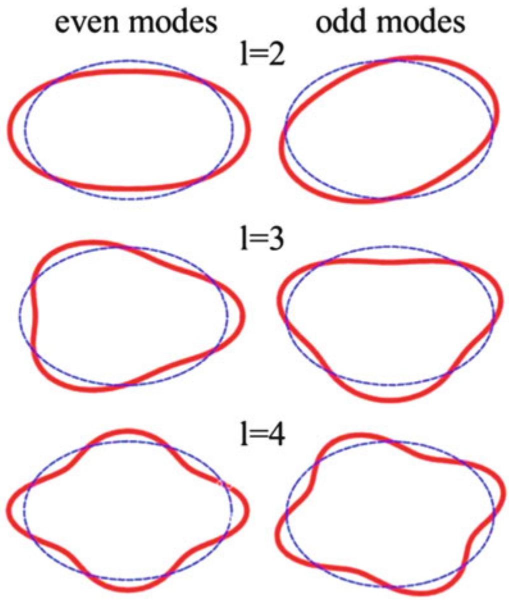

Fig. 5.3 Different orders of coherent mode perturbations of an initially uniformly populated elliptical cross section density, with l representing the azimuthal harmonic, and a distinction between even or odd (skew or tilted) mode symmetry (schematic)

As will be shown in more detail in Sect. 5.3.3 these schematic pictures can be used to characterize the actual eigenmodes of perturbation in beams. There, the picture is more complicated, however: spatial overlap of different modes of a certain order makes it more difficult to identify real space projections with certain modes, and it is easier to use the symmetry in phase planes, which is also described by l.

The eigenmodes also involve volume density inhomogeneities – except for the $l = 2$ modes of a 2d KV-distribution – and l also stands for the leading power in the space charge potential perturbation. Note that the $l = 2$ odd modes associated with skew rotation or tilting lead to a linear coupling force, which is caused by space charge (see Sect. 8.2.2).

The $l = 3$ "third order" modes are associated with pseudo-sextupolar[4] terms in the space charge potential. The $l = 4$ "fourth order" modes with pseudo-octupolar terms may appear as a result of resonance, but also due to mismatch of the density profile (see also Chap. 6).

Whether or not such modes really exist in concrete beams, and at the various orders, cannot be answered in a straightforward way. For 2D KV-distributions, for example, they can be shown to exist in all orders, but for more realistic beams with frequency spreads questions like phase mixing or Landau damping matter. Coherent modes oscillate with a frequency that is shifted away from multiples of the single particle frequencies by a so-called "coherent shift", which is of the order of the incoherent tune shift, but dependent on the type of mode. This shift is caused by the

[4]Here "pseudo-multipoles" refers to the leading term in the space charge potential, which is assumed to have the same power in x, y as the multipole term of a real magnet.

direct space charge and its deformation and should not be confused with the better known coherent shift of dipole oscillations, where only the beam centre oscillates without deforming the beam.

5.3.2 Basic Equations

We outline here the method presented in [2], where more details can be found. It is based on a perturbation theory using the linearized Vlasov equation of Eq. 3.2. For this derivation the following assumptions are made:

- 2D coasting beam approximation,
- constant, but not necessarily equal focusing strengths in x, y,
- a "generalized" anisotropic KV-distribution as unperturbed equilibrium with uniform density,
- different emittances.

While the limitation to constant focusing seems restrictive, we find that the resulting eigenmode frequencies can still be applied to describe the resonance conditions in periodic focusing by using them in "smooth approximation" coherent resonance conditions as will be shown, in particular, in Chap. 7.

For an explicit solution of the linearised Vlasov-Poisson problem we use the single particle frequencies in Eqs. 4.9 and start from the unperturbed Hamiltonian, Eq. 3.1, as well as the linearised Vlasov equation, Eq. 3.2.

Due to the absence of coupling in the KV-type equilibrium space charge potential, separate unperturbed Hamiltonians can be written for the $x-p_x$ and $y-p_y$ planes:

$$
\begin{aligned}
H_{0x} &= \frac{1}{2m\gamma}\left(p_x^2 + m^2\gamma^2\nu_x^2 x^2\right) \\
H_{0y} &= \frac{1}{2m\gamma}\left(p_y^2 + m^2\gamma^2\nu_y^2 y^2\right). \qquad (5.1)
\end{aligned}
$$

By using the property that the unperturbed orbits are harmonic oscillators with frequencies ν_x, ν_y, within the boundary ellipse given by a and b, we can define an anisotropy factor T as ratio of average oscillator energies, which is identical to the definition in Sect. 2.2.3:

$$
T \equiv \frac{a^2\nu_x^2}{b^2\nu_y^2}. \qquad (5.2)
$$

This allows us to use the two separate Hamiltonians as constants of motion to define a *generalized* anisotropic KV-distribution as

$$
f_0(x, y, p_x, p_y) = \frac{NT\nu_y/\nu_x}{2\pi^2 m\gamma a^2}\,\delta\left(H_{0x} + TH_{0y} - m\gamma\nu_x^2 a^2/2\right). \qquad (5.3)
$$

Analogous to the isotropic KV-distribution, Eq. 5.3 describes a uniformly populated ellipsoid in the 4D phase space, with uniform projections into any 2D subspace.

We now assume a small perturbation of the equilibrium beam distribution and space charge potential

$$f = f_0(H_{0x}, H_{0y}) + f_1(x, y, p_x, p_y, t)$$
$$\Phi = \Phi_0(x, y) + \Phi_1(x, y, t), \tag{5.4}$$

and obtain from Eq. 3.2 the linearised Vlasov equation

$$\begin{aligned}\frac{df_1}{dt} \equiv \frac{\partial f_1}{\partial t} + \frac{p_x}{m\gamma}\frac{\partial f_1}{\partial x} + \frac{p_y}{m\gamma}\frac{\partial f_1}{\partial y} - m\gamma\nu_x^2 x\frac{\partial f_1}{\partial p_x} - m\gamma\nu_y^2 y\frac{\partial f_1}{\partial p_y}\\ = \frac{NTq\,\nu_y/\nu_x}{2\pi^2 m^2\gamma^4 a^2}\left(p_x\frac{\partial \Phi_1}{\partial x} + T p_y\frac{\partial \Phi_1}{\partial y}\right)\\ \times \delta'\left[p_x^2 + \nu_x^2 x^2 + T(p_y^2 + \nu_y^2 y^2) - \nu_x^2 a^2\right],\end{aligned} \tag{5.5}$$

where Φ_1 is given by the perturbed density n_1

$$\nabla^2\Phi_1 = -\frac{q}{\epsilon_0}n_1 = -\frac{q}{\epsilon_0}\int f_1 dp_x dp_y. \tag{5.6}$$

Equations 5.5 and 5.6 are a closed set of linear, partial differential equations with f_1 and Φ_1 as unknown functions. Following the method of characteristics, f_1 is determined by integrating the r.h.s. of Eq. 5.5 along the unperturbed orbits. To carry out this integration it is essential that due to the linear total restoring force the unperturbed orbits are those of harmonic oscillators. For rational ratios of betatron tunes the two-dimensional unperturbed orbit is thus a periodic function characterized by an angle φ. This allows writing the total derivative of f_1 in the simplified form:

$$\frac{df_1}{dt} \equiv \frac{\partial f_1}{\partial t} + \nu_x\frac{\partial f_1}{\partial \varphi}. \tag{5.7}$$

Thus, a time harmonic ansatz can be made by introducing a mode frequency ω and writing

$$f_1 = f_1(\varphi)e^{-i\omega t},\ \Phi_1 = \Phi_1(\varphi)e^{-i\omega t}. \tag{5.8}$$

$f_1(\varphi)$ is obtained by integrating the total derivative over the full period of the two-dimensional unperturbed orbit. Moreover, due to the $\delta-$function character of the equilibrium distribution, the solutions for Φ_1 can be expressed as finite order polynomials in x and y in the interior of the beam, and as angular harmonics vanishing at infinity outside.[5] The leading order of the polynomials determines the order of the mode.

Dispersion relations for the mode frequency ω in the form of algebraic expressions are found as conditions for the existence of solutions of these equations, where Im $\omega > 0$ indicates exponential instability. For details of the solutions up to fourth order the reader is referred to [2]. It is noted that due to anisotropy the size of the algebraic expressions and the number of solutions grows substantially with the order. Some approximate examples for ω will be discussed in the following for further application in the following chapters.

5.3.3 Different Order Mode Frequencies

The above introduced space charge eigenmodes play a role in a variety of contexts. Some can be subject to instability even in constant focusing, where the instability is driven by anisotropy or emittance exchange (Chap. 9); others require periodic focusing and parametric resonance to be unstable (Chap. 7). Approximate formulae can be derived for small space charge terms, which are useful for interpreting computer simulation results; in particular, also with regards to the matter of Landau damping, the coherent mode frequency shift needs to be compared in size with the incoherent tune spread as will be discussed in Sect. 5.5.

It is helpful to introduce here several dimensionless quantities:

$$\sigma \equiv \omega/\nu_x; \quad \sigma_p \equiv \omega_p/\nu_x; \quad \alpha \equiv \nu_y/\nu_x; \quad \eta \equiv a/b; \tag{5.9}$$

where σ and σ_p are the coherent mode rsp. plasma frequencies normalized to ν_x, and α, η measure the ellipticity in focusing and in size.

The general form of solutions can be written as

$$\omega_{l,m} = l\nu_x + m\nu_y + \Delta\nu_{coh,l,m}, \tag{5.10}$$

where $|l| + |m|$ is bounded by the order of the mode, which is defined by the leading power in the perturbing space charge potential. $\Delta\nu_{coh,l,m}$ stands for the coherent tune shift,[6] which depends on space charge and the particularities of the mode.[7] Note that

[5] For a more general distribution function an infinite series expansion is needed as shown in an example in [3], besides the additional difficulty of anharmonic unperturbed orbits.

[6] Note that alternatively ω can be written in terms of zero intensity tunes $\nu_{0,x,y}$. This requires absorbing the space charge shifts from $\nu_{x,y}$ into $\Delta\nu_{coh,l,m}$.

[7] In most cases $\Delta\nu_{coh,l,m}$ is a positive number, with the exception of the "negative energy modes" discussed in Sects. 5.3.3.2 and 5.4.3. For full characterization of the mode spectrum additional parameters are needed in $\Delta\nu_{coh,l,m}$, besides l, m, to distinguish between even and odd and combinations with lower order resonant terms.

the total number of coherent mode frequencies – even and odd – rises steeply with the order: in second order it is four, in third order ten, and in fourth order it can reach twenty – depending on parameters.

For small space charge effects the various resonant denominators – increasing in number with the order – can again be assumed as small quantities leading to dominant terms. We evaluate the full dispersion relations derived in [2] up to fourth order for a small incoherent space charge tune shift, and for the highest frequency modes.

5.3.3.1 Second Order Even Modes

The second order *even* perturbations are of the envelope oscillation type and require a perturbing potential $\Phi_{1,even} = a_0x^2 + a_2y^2$ inside the unperturbed beam, where a_0 and a_2 are constants depending on focusing and emittance ratios. The scaled eigenfrequencies σ are solutions of the dispersion equation

$$(1+\eta)^2 + \sigma_p^2\left(\frac{1+2\eta}{4-\sigma^2} + \frac{2\eta+\eta^2}{4\alpha^2-\sigma^2}\right) + \sigma_p^4\left(\frac{2\eta}{(4-\sigma^2)(4\alpha^2-\sigma^2)}\right) = 0, \tag{5.11}$$

which allows only real eigenfrequencies.

For zero space charge the mode frequencies are given by the zeros of the resonant denominators, hence ω results as $2\nu_{0x}$ or $2\nu_{0y}$. For finite space charge the solutions of Eq. 5.11 also depend on α and η as measures for the anisotropy, hence the asymmetry in focusing and beam size respectively emittances. An example with values for $\alpha = \nu_y/\nu_x = 0.48$ and $\eta = a/b = 1.54$ kept fixed, hence also a fixed emittance ratio $\epsilon_x/\epsilon_y = 4.91$, is shown in Fig. 5.4 (see also [2]). The tune depression ν_y/ν_{0y} is varied, which also determines ν_x/ν_{0x}. Note that the coherent mode frequencies ω_1, ω_2 and their incoherent constituents $2\nu_x, 2\nu_y$ according to Eq. 5.10 are all normalized to ν_{0y}.

Approximate explicit formulae are easily obtained in first order of the space charge parameter $\sigma_p^2 \approx 2(1+\eta_0)\Delta\nu_x/\nu_{0x}$ by assuming that the resonant denominators $4-\sigma^2$ or $4\alpha^2-\sigma^2$ are independently small quantities.[8] For given space charge this requires that the tunes in x and y are sufficiently split, otherwise a different – more complex – expansion is needed. With the space charge tune shifts $\Delta\nu_x \equiv \nu_{0x} - \nu_x$ and $\Delta\nu_y \equiv \nu_{0y} - \nu_y$ we obtain in first order in $\Delta\nu_{x,y}$:

$$\begin{aligned}\omega_1 &= 2\nu_{0x} - 2\Delta\nu_x\left(1 - \frac{1+2\eta_0}{4(1+\eta_0)}\right)\\ \omega_2 &= 2\nu_{0y} - 2\Delta\nu_y\left(1 - \frac{2+\eta_0}{4(1+\eta_0)}\right).\end{aligned} \tag{5.12}$$

[8] Here, η_0 is understood as fixed value, hence independent of space charge.

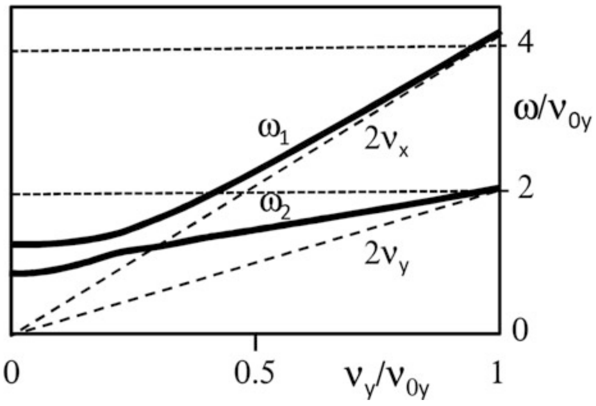

Fig. 5.4 Anisotropic second order even modes showing coherent mode frequencies ω_1, ω_2 and $2\nu_x, 2\nu_y$ as function of space charge tune depression (all divided by ν_{0y})

Equations 5.12 indicate that the repulsive character of space charge induces a downwards shift of the mode frequencies relative to their zero-current values $2\nu_{0x}, 2\nu_{0y}$.

More significant is the shift relative to $2\nu_x, 2\nu_y$. It contains the actual coherent tune shift $\Delta\nu_{coh}$, which plays a key role for the Landau damping discussion in Sect. 5.5 and is found positive for this mode:

$$\begin{aligned}\omega_1 &= 2\nu_x + \Delta\nu_{coh,2,1} = 2\left(\nu_x + \frac{1}{4}\Delta\nu_x\frac{1+2\eta_0}{1+\eta_0}\right)\\ \omega_2 &= 2\nu_y + \Delta\nu_{coh,2,2} = 2\left(\nu_y + \frac{1}{4}\Delta\nu_y\frac{2+\eta_0}{1+\eta_0}\right).\end{aligned} \tag{5.13}$$

The dependence on the ellipticity parameter η_0 is relatively weak, and for not too flat beams Eq. 5.12 can be approximated by assuming $\eta_0 = 1$, hence,

$$\omega_{1,2} = 2\left(\nu_{x,y} + \frac{3}{8}\Delta\nu_{x,y}\right). \tag{5.14}$$

In the special case of a round ($\eta_0 = 1$) beam with identical focusing, $\nu_{0x} = \nu_{0y} = \nu_0$, hence the beam is fully isotropic. In this case Eq. 5.11 yields the familiar results for "fast" and "slow" envelope modes for arbitrary intensity, and in dimensionless units:

$$\sigma_f^2 = 4 + \sigma_p^2,\ \sigma_s^2 = 4 + \frac{\sigma_p^2}{2}. \tag{5.15}$$

Solutions of Eq. 5.15 as function of ν/ν_0 are shown in Fig. 5.5.

In terms of mode frequencies, expanded for small space charge, we obtain:

$$\omega_f = 2\nu_0 - \Delta\nu = 2(\nu + \frac{1}{2}\Delta\nu);\ \ \omega_s = 2\nu_0 - \frac{3}{2}\Delta\nu = 2(\nu + \frac{1}{4}\Delta\nu). \tag{5.16}$$

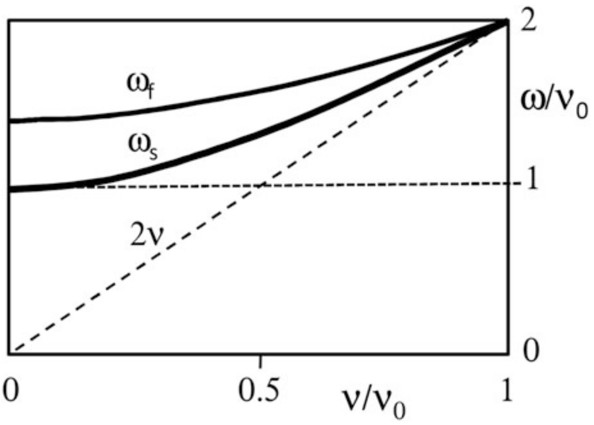

Fig. 5.5 Second order even modes coherent frequencies ω_f, ω_s and 2ν for round beam and identical focusing strength as function of space charge tune depression (all divided by ν_0)

The fast mode is also called "breathing mode" due to the periodically oscillating radius. In the slow or "quadrupolar mode" the initially circular beam is periodically flattened. The former is an in-phase mode, the latter an out-of-phase mode relating to the change of envelopes in the two planes.

5.3.3.2 Second Order Odd Modes

The less familiar second order *odd* space charge modes of Fig. 5.3 involve a skew rotation (tilting) in $x-y$ space. For this discussion a linear lattice without any external skew components is assumed here, hence the skew force is entirely due to space charge. These odd modes have a perturbed space charge potential $\Phi_{1,odd} = a_1 xy$ inside, with a_1 an arbitrary coefficient. Note that they cannot be obtained by perturbing the usual envelope equations of Sect. 3.2.1, which only describe even modes. Alternatively to our Vlasov analysis, they can be also retrieved by linearising the second order "Chernin equations" in [4].

With our Vlasov ansatz the odd mode dispersion equation is found as

$$(1+\eta)^2 + \frac{\sigma_p^2}{2}\left(\frac{(1-\alpha)(1-\eta^2/\alpha)}{(1-\alpha)^2-\sigma^2} + \frac{(1+\alpha)(1+\eta^2/\alpha)}{(1+\alpha)^2-\sigma^2}\right) = 0, \quad (5.17)$$

Inspecting the resonant denominators, a *coherent sum* (ω_{sum}) as well as a *coherent difference* (ω_d) mode are associated with the "+" and "−" sign. A solution of Eq. 5.17 for these mode frequencies and their incoherent constituents $\nu_x \pm \nu_y$ for the sum (+) respectively difference modes (−) are shown in Fig. 5.6, again for $\alpha = \nu_y/\nu_x = 0.48$ and $\eta = a/b = 1.54$. For small space charge, $\nu_y/\nu_{0y} \rightarrow 1$, the coherent sum and difference mode frequencies merge to $\nu_{0x} + \nu_{0y}$ respectively $\nu_{0x} - \nu_{0y}$.

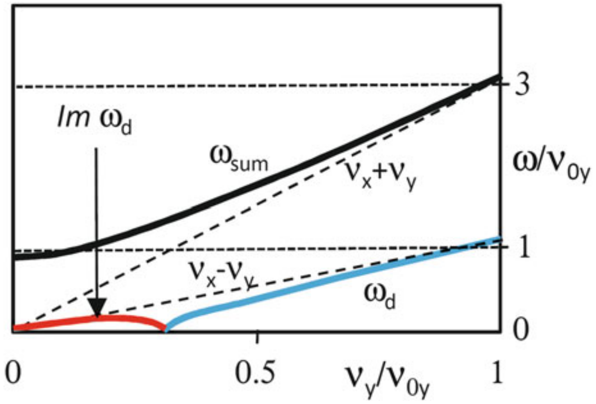

Fig. 5.6 Anisotropic second order odd modes showing coherent sum and difference mode frequencies, ω_{sum}, ω_d, and $\nu_x \pm \nu_y$ as function of space charge tune depression (all divided by ν_{0y}); ω_d is a "negative energy mode" turning into exponential instability ($Im\ \omega_d > 0$)

Noteworthy is the fact that for sufficiently strong tune depression – in our example for $\nu_y/\nu_{0y} < 0.3$ – the coherent difference mode becomes unstable with $\omega_d^2 < 0$, hence a pair of stable and unstable solutions is emerging. This occurs if for $\nu_{0x} > \nu_{0y}$, anisotropy and space charge lead to $\nu_x < \nu_y$, hence a focusing ratio reversal (equally by swapping x and y). In Fig. 5.6 the switch to instability happens at the point, where ν_{0y}/ν_{0x} changes from < 1 to > 1. This spontaneous space charge induced instability is a "self-skewing" effect, which leads to a periodical emittance exchange between x and y. A necessary condition is a sufficiently high degree of anisotropy to enable the focusing ratio reversal via different tune depressions in x and y.

Note that the difference mode ω_d is shifted downwards from the incoherent term $\nu_x - \nu_y$. It thus qualifies as "negative energy mode", which can become unstable by coupling with a "positive energy mode" – here the corresponding negative frequency mode $-\omega$ – without change of the total energy. The sum mode $\omega_s um$, instead is a "positive energy mode" due to the upwards shift from the incoherent term $\nu_x + \nu_y$. For further details on the role of these mode energies see Sect. 5.4.

In practical terms, this self-skewing mode may not be directly observable as it closely overlaps with a connected space charge phenomenon in fourth order, the "Montague resonance" at $2\nu_x - 2\nu_y \approx 0$ – see Fig. 9.2 in Chap. 9.

The dynamical behaviour of this self-skewing beyond linearised theory has been studied in some detail in [5], based on Chernin's fully nonlinear equations.

We search for explicit analytical expressions by expanding Eq. 5.17 for small space charge. For the coherent sum mode, which will find application in the sum parametric resonances of Sect. 7.7, we use the sum resonant denominator and obtain in first order in $\Delta\nu_x$[9]:

$$\omega_{sum} = \nu_x + \nu_y + \Delta\nu_{coh,2,sum} = \nu_x + \nu_y + \Delta\nu_x \left(\frac{\eta_0 - \alpha_0^2}{\alpha_0} + \frac{1}{2} \frac{\alpha_0 + \eta_0^2}{\alpha_0(1+\eta_0)} \right). \tag{5.18}$$

[9] η_0 and also α_0 are both understood as values independent of space charge.

ω_{sum} approaches $\nu_{0x} - \nu_{0y}$ in the limit of vanishing space charge, while the coherent shift, $\Delta\nu_{coh,2,sum}$, is found positive for all cases of anisotropy.

For the coherent difference mode the difference resonant denominator in Eq. 5.17 yields, expanded for small space charge (and assuming $\nu_{0x} > \nu_{0y}$),

$$\omega_d = \nu_x - \nu_y + \Delta\nu_{coh,2,d} = \nu_x - \nu_y + \Delta\nu_x \left(\frac{\alpha_0^2 - \eta_0}{\alpha_0} + \frac{1}{2} \frac{\alpha_0 - \eta_0^2}{\alpha_0(1+\eta_0)} \right). \tag{5.19}$$

ω_d approaches $\nu_{0x} - \nu_{0y}$ in the limit of vanishing space charge, but the coherent shift, $\nu_{coh,2,d}$, is found negative for all values $\nu_{0x} > \nu_{0y}$, hence we deal with negative energy modes as in the example of Fig. 5.6.

5.3.3.3 Third Order Modes

For the full dispersion relation expression we refer to [2]. For sufficiently split tunes, and the highest frequency mode (assuming $\nu_{0x} > \nu_{0y}$ without loss of generality), only terms with resonant denominators of the kind $9-\sigma^2$ need to be retained. Hence, in first order in $\Delta\nu_x$ we find[10]:

$$\omega_3 = 3\left(\nu_x + \frac{\Delta\nu_x}{24} \frac{3 + 9\eta_0 + 8\eta_0^2}{(1+\eta_0)^2}\right). \tag{5.20}$$

As already in second order, the dependence on η_0 in this and the following examples is again relatively weak, thus an expression for approximately round – not too flat – beams is obtained by setting $\eta_0 = 1$, in which case the coherent frequency is:

$$\omega_3 = 3\left(\nu_x + \frac{5}{24}\Delta\nu_x\right), \tag{5.21}$$

which yields only slightly different results from Eq. 5.20. The coefficient in front of $\Delta\nu_x$ changes typically by $< 10\%$ for a change of η_0 by $\pm 25\%$ away from unity.

Explicit calculation of frequencies is straightforward for identical focusing constants and a round beam. This leads to four solutions branching off from the zero-intensity mode frequencies $3\nu_0$ as well as ν_0, which are written here for arbitrary intensity, and in dimensionless units:

$$\sigma_{1,2}^2 = \frac{10 + \sigma_p^2 \pm \sqrt{64 + 20\sigma_p^2 + \sigma_p^4}}{2}$$
$$\sigma_{3,4}^2 = \frac{20 + \sigma_p^2 \pm \sqrt{256 + 16\sigma_p^2 + \sigma_p^4}}{4}. \tag{5.22}$$

[10] Note that in third order the distinction even-odd is equivalent to an exchange between x and y.

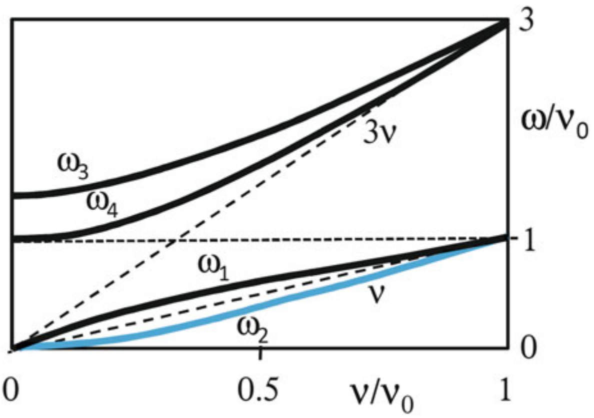

Fig. 5.7 Third order coherent mode frequencies ω_i ($i = 1 \ldots 4$) and their incoherent constituents 3ν and ν as function of space charge tune depression, for round beam and identical focusing strengths (all divided by ν_0)

Solutions of Eqs. 5.22 as function of ν/ν_0 are shown in Fig. 5.7. Note that the lowest order mode ω_2 is shifted downwards with respect to ν. Hence, it qualifies as negative energy mode similar to the second order odd mode in Sect. 5.3.3.2, but in this case it is always stable.[11]

For the highest frequency mode, and in first order in $\Delta\nu$, this results in

$$\omega_3 = 3\left(\nu + \frac{1}{4}\Delta\nu\right). \tag{5.23}$$

5.3.3.4 Fourth Order Modes

Similar to third order, and for sufficiently split tunes, the fourth order even mode dispersion relation in [2] yields for the highest frequency mode, and in first order in $\Delta\nu_x$ (again assuming $\nu_{0x} > \nu_{0y}$):

$$\omega_4 = 4\left(\nu_x + \frac{\Delta\nu_x}{64}\frac{5 + 20\eta_0 + 29\eta_0^2 + 16\eta_0^3}{(1+\eta_0)^3}\right). \tag{5.24}$$

For approximately round – not too flat – beams, we set again $\eta_0 = 1$ and find

$$\omega_4 = 4\left(\nu_x + \frac{35}{256}\Delta\nu_x\right). \tag{5.25}$$

The case with identical tunes and a round beam leads to five solutions, again for arbitrary intensity and in dimensionless units:

[11] With anisotropy also third order modes may become unstable – see Chap. 9.

$$
\begin{aligned}
\sigma_1^2 &= 16 + \sigma_p^2 \\
\sigma_{2,3}^2 &= \frac{20 + \sigma_p^2 \pm \sqrt{(20 + \sigma_p^2)^2 - 4(64 - 2\sigma_p^2)}}{2} \\
\sigma_{4,5}^2 &= \frac{40 + \sigma_p^2 \pm \sqrt{(40 + \sigma_p^2)^2 - 8(128 + 10\sigma_p^2)}}{4}.
\end{aligned}
\tag{5.26}
$$

Here, $\sigma_{1,2,4}$ are branching off from the zero-intensity mode frequency $4\nu_0$, and $\sigma_{3,5}$ from $2\nu_0$.

For the highest frequency mode, σ_2, this yields in first order in $\Delta\nu_x$:

$$
\omega_4 = 4\left(\nu + \frac{3}{16}\Delta\nu\right). \tag{5.27}
$$

Of theoretical interest is the lowest frequency branch mode, σ_3, which yields[12]

$$
\omega_3 = 2\left(\nu - \frac{1}{4}\Delta\nu\right). \tag{5.28}
$$

The "–" sign in front of the coherent shift indicates a negative energy mode. Using the full expression in Eq. 5.26 for all intensities shows that for this branch σ_3^2 becomes negative, hence unstable, for sufficiently high intensity. The transition occurs for $\nu/\nu_0 < 0.24$, which is the lowest order case of the so-called "Gluckstern modes" derived in [6]. It is a particular feature of the KV-distribution, with a more detailed discussion in Sect. 7.3.2.

5.3.4 *Overview on Coherent Mode Frequencies*

For an overview we summarize here some the above results, in first order of the space charge shift, and written in the form $\omega_k = k\,(\nu_x + F_k\Delta\nu_x)$. The factors F_k are listed in Table 5.1 for the highest frequency branches of even modes up to fourth order. They determine the intensity dependent shift away from $k\nu_x$, which is given for equal focusing strengths as well as for split focusing, and beams not too far from round. For completeness we also add the first order dipole mode, which is not pursued further here.

It is noted that in all orders the coherent shifts away from $\nu_{x,y}$ are always largest for the un-split tunes cases. This is apparently due to the fact that equal tunes allow density deformations, which are in phase in both degrees of freedom – like in the

[12] The index of ω is only numbering the different options in fourth order; the r.h.s. factor "2" has to do with the symmetry of this particular fourth order mode.

Table 5.1 Coefficients F_k in coherent frequency expressions $\omega_k = k(\nu_x + F_k \Delta\nu_x)$ for highest frequency branches and equal as well as significantly split focusing

	First order	Second order	Third order	Fourth order
k:	1	2	3	4
F_k: $(\nu_{0x} = \nu_{0y})$	1	$1/2$	$1/4$	$3/16$
F_k: $(\nu_{0x} \neq \nu_{0y})$	1	$3/8$	$5/24$	$35/256$

case of the envelope breathing mode ($F_2 = 1/2$). Also, these shifts are all upwards with space charge, which qualifies them as positive energy modes. Negative energy modes can only occur with the lower frequency branches.

5.4 Negative Energy Modes and Free Energy

The concept of waves of "negative energy" is widely used in plasmas, where dissipation allows growth of such a wave under total energy conservation (see, for example, a review by Lashmore-Davies in [7]). In accelerators negative energy waves find direct application for example in the "resistive wall instability" of longitudinal waves on a beam. In the context of beam particles confined by a focusing potential, where propagating waves are replaced by oscillatory modes, the subject of negative energy is conceptually more challenging.

5.4.1 Basic Concept

The concept that waves of negative energy in plasmas can couple with positive energy waves and create a so-called "reactive" (non-dissipative) instability was originally developed by Kadomtsev et al. in [8].

Some general and very useful principles to understand this concept have been presented by Landau and Lifschitz in [9] with the observation that in a plasma in thermal equilibrium – like a Gaussian distribution – excitation and relaxation of a wave always means "positive energy": the energy of the system with the wave excited is higher than that of the equilibrium. Under total energy conservation such a wave cannot grow, and stability is a consequence.

Of direct applicability to charged particles confined in a time-independent focusing potential is the so-called "Newcomb-Gardner theorem" discussed by Fowler in [10]. According to it a system described by a monotonically decreasing function of the Hamiltonian – hence also isotropic – is stable. In such a system the highest density layer in phase space is close to zero energy, and layers with increasing total particle energy have lower density. Fowler argues that in this case there is no source of free energy to drive an instability.

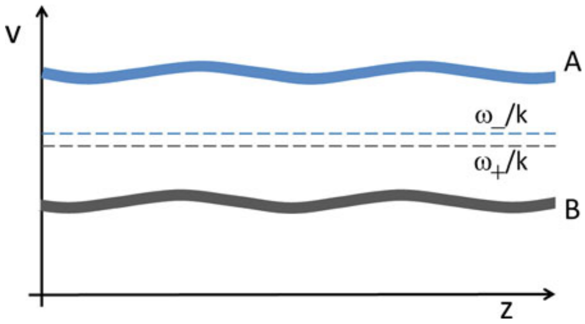

Fig. 5.8 Principle of two-stream instability in longitudinal phase space between plasma stream A with slow wave and B with fast wave

A different situation arises for a drifting plasma or a beam, which is not isotropic in the laboratory frame. Looking at waves, the energy of a wave also depends on the frame of reference. A backwards moving "slow" wave in the beam frame becomes a negative energy wave in the laboratory frame: in the presence of the wave the total energy is reduced compared with the unperturbed beam. With dissipation, like a finite wall resistivity, unstable growth occurs as "resistive wall instability" (see, for example, in [11]).

Since energy conservation must hold, growth of a negative energy wave is either possible by dissipation of the electromagnetic field energy as in the resistive wall instability, or by coupling with a positive energy wave. The coupled waves become a "zero energy system", which can grow without violating energy conservation.

The second case is schematically shown in Fig. 5.8 for the well-known two-stream instability of streaming plasmas or beams with a velocity difference (see, for example, Chen in [12]). A wave with wave number k on the plasma stream A (velocity v_A) with plasma frequency ω_p and velocity opposite to the direction of A, a so-called "slow wave"

$$\omega_- = kv_A - \omega_p, \tag{5.29}$$

is a negative energy wave[13] in the frame of the average velocity of beams A and B as its excitation requires lowering of the total energy of A; the opposite is the case for the forwards moving "fast wave" on plasma stream B (velocity v_B)

$$\omega_+ = kv_B + \omega_p, \tag{5.30}$$

which is a positive energy wave. If v_A and v_B get close enough the two waves couple, which results in growth of their amplitudes.

[13]Note the connection with the sign in front of the "coherent shift" ω_p – in analogy with the behaviour in a potential in Sect. 5.4.3.

5.4.2 Multi-stream Instability of Phase Space Filaments

An interesting application of interacting "streams" of charged particles and coupling of positive and negative energy waves is found in the subject of filamentary fine structures in phase space, which is worth noting here.

It was shown theoretically in [13] that after injection of a bunched beam from a linear accelerator into a circular accelerator, where the bunch structure is not maintained by a suitable rf, the expanding filaments in longitudinal phase space eventually become unstable due to a multi-stream instability driven by space charge. The process is analogous to the above described two-stream mechanism in Fig. 5.8.

This was proven experimentally in the GSI synchrotron SIS18 by Appel and Boine-Frankenheim in [14]. First the problem was studied by multi-particle simulation, and Fig. 5.9 shows the 36 MHz periodic bunch structure of the injected beam, which is allowed to de-bunch if no rf voltage is applied. The de-bunching process starts right after injection, which creates a rising number of increasingly fine near-by filaments in longitudinal velocity space as shown in Fig. 5.10. The length of these filaments is increasing, while the momentum displacement between neighbouring filaments as well as their width are shrinking. The top frame in Fig. 5.10 at 0.04 ms indicates a point of transition, where the "laminar" filamentary flow in phase space turns into a "turbulent" flow, which eventually smears out the void between filaments as shown in the bottom graph of Fig. 5.10 at 0.13 ms. The point of such a transition is reached, when neighbouring filaments satisfy the "multi-stream instability" threshold derived in [13].

Figure 5.11 confirms this process by experimental Schottky noise data obtained and using a 36 MHz Ar^{18+} beam in the SIS18 injected at 11.4 MeV/u (with lower intensity than assumed in simulations). There is good agreement between the experiment and the theoretical picture noting that a broad coherent Schottky noise spectrum starts growing beyond the dotted line on the r.h.s. graph, which is the theoretically calculated time threshold for the given beam current in the experiment.

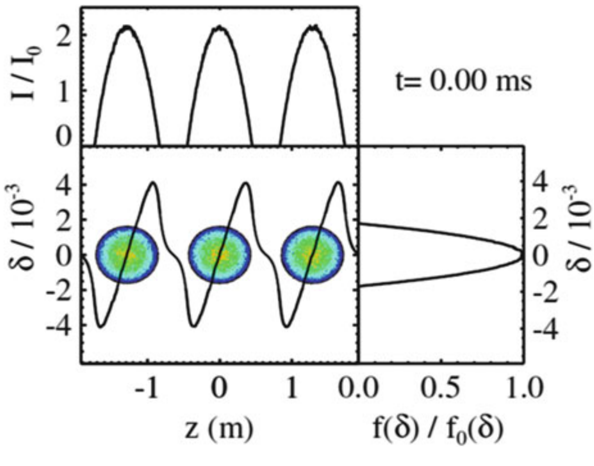

Fig. 5.9 Initial longitudinal phase space of a sequence of bunches at injection into the SIS18 (Source: [14])

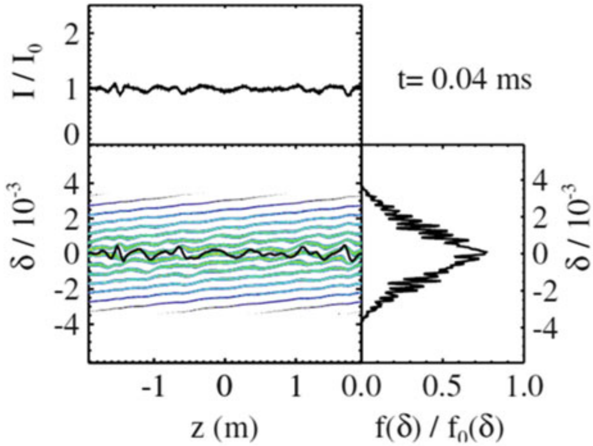

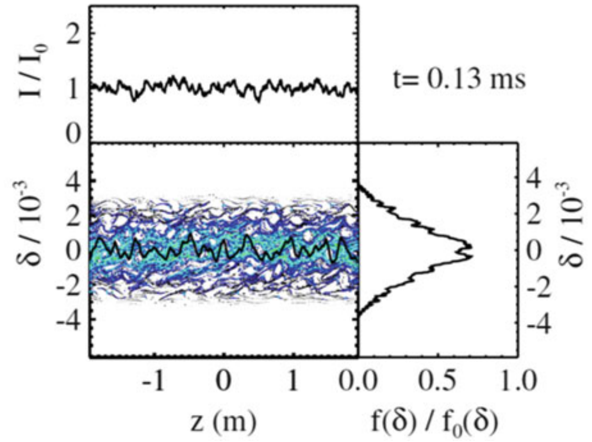

Fig. 5.10 Simulation results at 0.04 ms (*top graph*) and 0.13 ms (*bottom graph*) after injection showing onset of multi-stream instability (Source: [14])

For completeness we also mention that the lengthening filaments at some point may also become subject to longitudinal resistive impedance driven instability. This is due to the fact that the local current of a single filament shrinks proportional to its momentum width, hence the corresponding threshold for resistive instability – with the current proportional to the square of the momentum width (see, for example, in [11]) - is exceeded at some point. Which one of these instability processes – multi-streaming or longitudinal resistive – dominates in a given situation needs to be checked.

5.4.3 Negative Energy Modes in a Potential

An analogous approach to interpret coherent space charge instabilities of beams in a *focusing potential* was suggested in [15]. In this case one deals with coupling

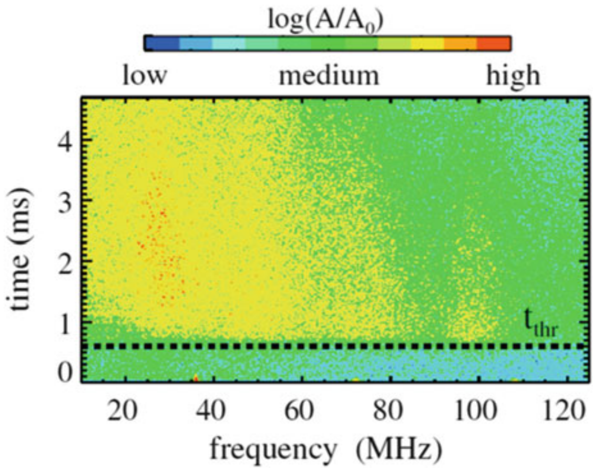

Fig. 5.11 Experimental results with frequency spectrum of coherent Schottky noise rising right after the theoretically calculated time of onset as indicated by the *dotted line* (Source: [14])

of (non-propagating) negative energy modes of oscillation with positive energy modes, which is conceptually challenging. The ansatz in [15] was in terms of a dielectric function – in analogy with the wave problem in [8] – applied to the special case of the "Gluckstern" type KV-instabilities discussed in Sect. 7.3.2.3. The characterisation of the mode energy as positive or negative was made in [15] – analogous to [8] – according to the sign of the derivative of the dielectric function with respect to the mode frequency.

This is applied in [3] to the behaviour of the negative energy modes in the transition from the highly non-monotonic KV-distribution to a monotonically decreasing distribution function. In this work the perturbed space charge potential in constant focusing and for 2D axisymmetric beams is expanded in an infinite series of Legendre polynomials.[14] For analytical tractability the nonlinear part of the equilibrium space charge potential is assumed compensated by a suitable external potential.

As shown in Fig. 5.12, four cases of distribution functions are distinguished, where "A" stands for the completely hollow KV-distribution, "B" for a semi-hollow non-monotonic distribution, "C" for a waterbag and "D" a strictly monotonic distribution. B, C and D are defined as superpositions of a continuous spectrum of KV-distributions with radius a and weight function $g(a^2)$. It is suggested in [3] that sufficiently hollow (non-monotonic) distributions in phase space have the free energy to drive an instability. In the mode picture such instabilities are enabled by a confluence of a negative energy with a positive energy oscillation. The confluence allows growth of the amplitude of the coupled oscillation without violating energy conservation.

[14]This extends the procedure by Gluckstern in [6] for a KV-distribution, where due to the δ-function nature only a finite series of Legendre polynomials is needed.

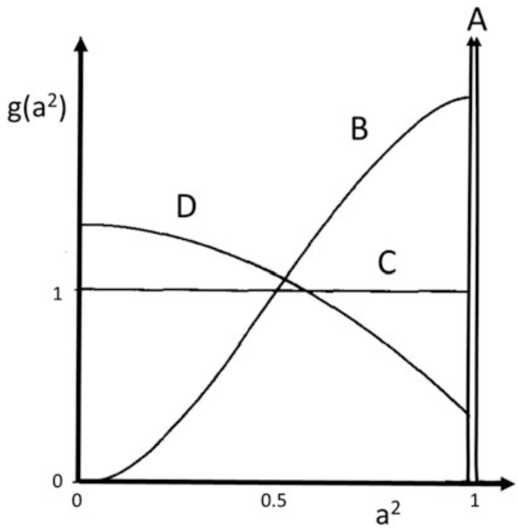

Fig. 5.12 Definition of different axisymmetric distribution functions A, B, C and D as superpositions of a spectrum of KV-distributions with radius a and weight $g(a^2)$, used as basis for a Vlasov stability analysis (Source: [3])

The spectrum of the axisymmetric modes is shown in Fig. 5.13 for above cases A, B and C. From [15] a mode of given order $2j$ can be characterized as negative energy oscillation, if $\omega/(2j\nu) < 1$, and as positive energy oscillation, if $\omega/(2j\nu) > 1$. Hence, for negative (positive) energy oscillation ω/ν is decreasing (increasing) with increasing intensity.[15] Applied to the KV-distribution, case A of Fig. 5.12, the following results: in fourth order the negative energy oscillation ω_{21} couples with the corresponding negative frequency mode as positive energy mode.[16] This happens for $\omega_p/\nu = 5.66$ ($\nu/\nu_0 = 0.24$), and beyond this point instability emerges. In sixth order the same between ω_{32} and ω_{31} for $\omega_p/\nu > 3.39$ ($\nu/\nu_0 < 0.39$), and similar in higher order. The semi-hollow Case B shows only short patches of instability, with tiny growth rates; the waterbag case C shows that the negative energy oscillations have entirely disappeared (similar for Case D, not shown), and stability results. Note that the remaining "fast" modes ω_{jj} – characterized by a large and positive coherent tune shift, hence positive energy oscillations – are also retrieved in the fluid model of Sect. 5.6. Instead, the additional (also positive energy) oscillations ω_{31} etc. are kinetic, but have almost vanishing coherent tune shifts. It is concluded that this switch in stability behaviour from case A to D is fully consistent with the Newcomb-Gardner theorem in [10].

The appearance of negative energy oscillations is not limited to KV-type or hollow distributions. Negative energy modes also play a role for anisotropic distributions, where apparently the "negative energy" stems from anisotropy. Instability is found accordingly as is the case in the second order odd mode example of Sect. 5.3.3.2 – see also Chap. 9.

[15] Note that it is essential here to compare ω with the *space charge shifted* ν.

[16] This mode is identical with ω_3 in Sect. 5.3.3.4.

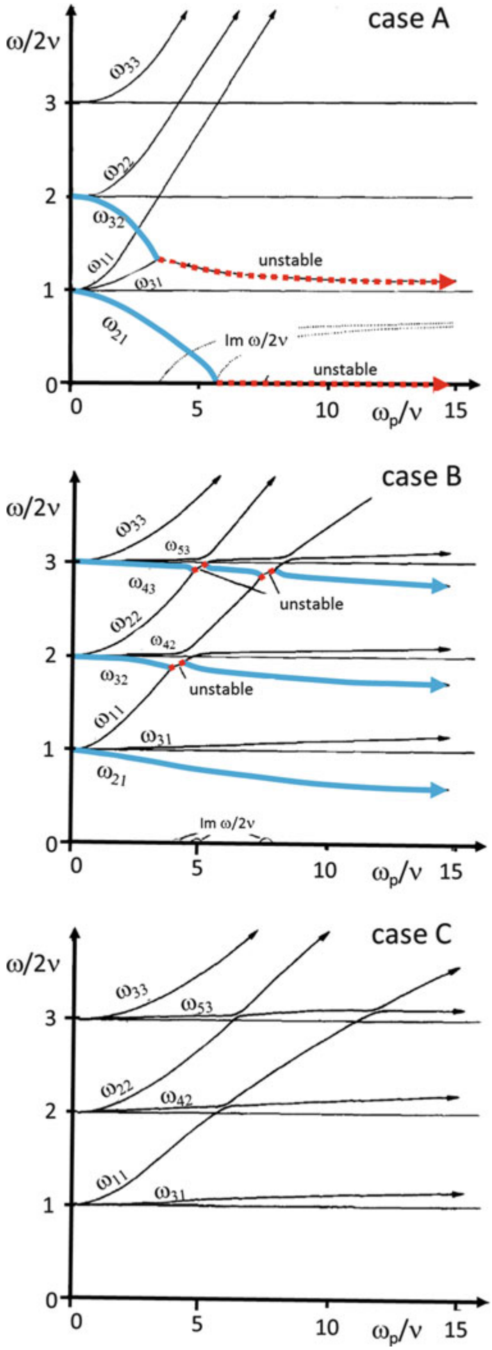

Fig. 5.13 2D axisymmetric coherent mode frequencies (divided by 2ν, continuous lines) for KV-distribution (case A, *left graph*), semi-hollow phase space distribution (case B, *centre graph*) and waterbag distribution (case C, *right graph*) as function of intensity parameter ω_p/ν. Note that the order of a mode is given by $2j$, where j is the first index of ω_{jn}; while the second index is an additional azimuthal mode number; negative energy mode frequencies *thick* (*blue*) *continuous lines*, on instability *thick dashed* (*red*) *lines* (Source: [3])

5.5 Landau Damping

Conceptually, Landau damping in multi-dimensional beams is not a simple phenomenon, and its interpretation can be a challenging problem. The concept of Landau damping of a longitudinal wave in a plasma – or on a coasting beam – by freely streaming particles cannot directly be applied to non-propagating eigenmodes in a potential. We draw an analogy and describe this problem as interaction between coherent modes of oscillation and the spectrum of single particle tunes trapped in the transverse potential well. The assumption that damping of these modes works similar to that of waves – depending on the overlap between coherent frequency and the distribution of single particle tunes – is built on this analogy and requires validation by simulation.

5.5.1 General Observations

In circular accelerators the primary source of a spread in the spectrum of single particle tunes can be a magnetic octupole, or the momentum spread combined with chromaticity. We focus here on dominant space charge effects and ignore the effects of octupoles or chromaticity. For non-KV beams at high intensity we thus assume the spread of single particle frequencies is only due to the space charge nonlinearity. Furthermore, we limit the discussion to internal modes of beams – leaving aside the dipole modes, where space charge plays a different role.

In the presence of mechanisms to excite coherent oscillations, like parametric resonances in periodic focusing or coherent magnet error driven resonances, the following questions arise:

- Under what conditions can the tune spread work as Landau damping and prevent the instability of certain modes – here the parametric resonances? (Chap. 7)
- Are similar conditions also applicable if these modes are excited by external sources, like in the case of coherent magnet error resonances? (Chap. 8)
- What is the role of Landau damping if a coherent resonance is "mixed" with single particle resonances?

Quantitative criteria for Landau damping are not straightforward for beams in a confining – possibly time-dependent – potential. It is helpful for the present discussion to compare the spectral distribution of single particle frequencies with the location of expected coherent frequencies calculated by smooth approximation, which is shown schematically in Fig. 5.14. Particles with frequencies in the vicinity of a coherent mode frequency ω may interact with the mode and cause damping – analogous to the velocity comparison between particles and waves in the usual Landau damping mechanism for propagating waves. It is essential here that beams with monotonically decreasing distribution function have their highest density in the beam centre. Thus, due to space charge repulsion the lowest frequencies in

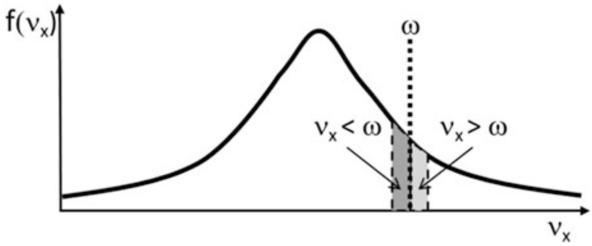

Fig. 5.14 Principle of Landau damping of an eigenmode ω by a spectral distribution of single-particle tunes ν_x

the distribution are associated with the smallest betatron oscillation amplitudes. Particles with lower frequency than that of the coherent oscillation gain amplitude to synchronize with the oscillation, while higher frequency particles lose amplitude. If the location of the coherent frequency ω on the spectral distribution occurs at a sufficiently large negative slope – as indicated in Fig. 5.14 – more particles gain energy, and the net effect is a damping of the coherent oscillation.[17]

Two necessary conditions for Landau damping can be adopted from the analogy with waves:

- A sufficient overlap of the spectrum of single particle frequencies with the coherent mode frequency ω under consideration,
- and a positive shift of ω with regard to the peak of the spectral distribution, which ensures the negative slope.

Note that in beams the peak of the spectral distributions is largely identical with the rms value of single particle frequencies ν. Following Sect. 5.4.3 a positive shift is thus a feature of positive energy modes, while a negative shift would indicate negative energy modes.

5.5.2 Tune "Footprints" with Space Charge

These conditions can be tested by determining analytically the coherent mode frequencies and plotting them on a spectral chart of single particle frequencies of a well-matched beam. Such "tune footprints" are shown here by using the 2D beam option of the TRACEWIN multi-particle simulation code (for TRACEWIN see also Sect. 2.3.2).

The tune footprints for rms equivalent Gaussian (truncated at 3.2σ) and waterbag distributions of 2D coasting beams[18] are compared in Fig. 5.15. The footprint is a

[17] A sign of caution is in place here: coherent frequencies calculated for KV-distributions are compared with single particle tune spectra of non-KV beams, which ultimately requires validation by computer simulation.

[18] The structure of the FODO lattice used here is defined in Fig. 7.2 of Sect. 7.4, but its details are not significant here.

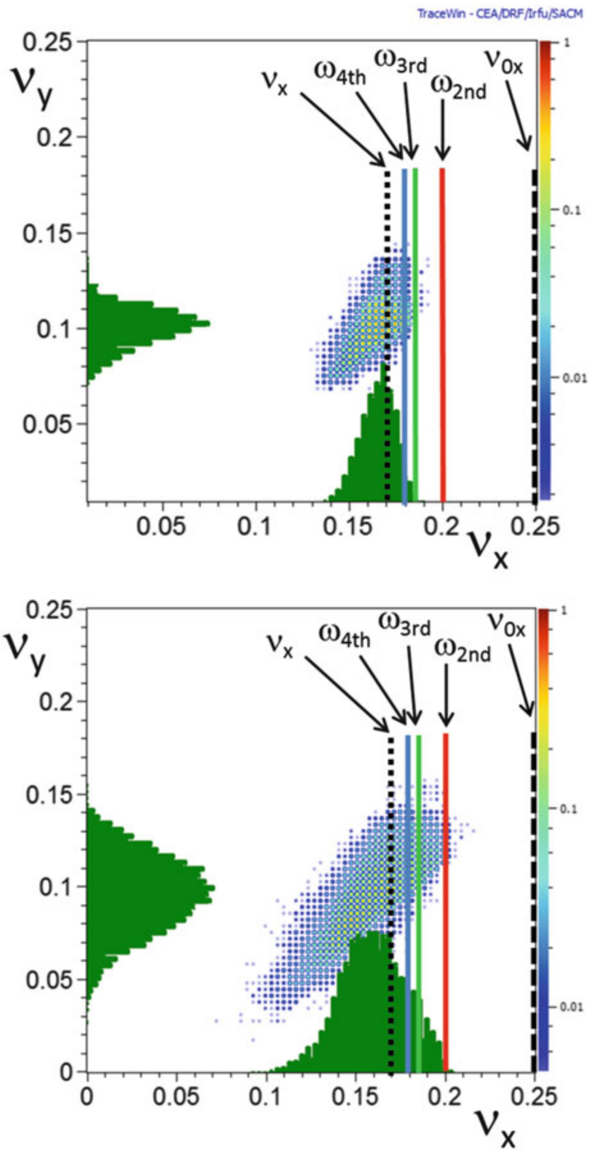

Fig. 5.15 Tune footprint for rms equivalent waterbag (*top*) and truncated Gaussian (*bottom*) distributions and tunes $\nu_{0,x,y} = 0.25/0.19$, with rms tunes $\nu_{x,y} = 0.17/0.11$. Also shown are the highest frequency coherent space charge mode frequencies ("even" transverse modes in x, divided by the order k, up to fourth order) and tune density projections; the *vertical dotted line* indicates the rms tune $\nu_x = 0.17$

colour coded density plot of tunes of all involved particles (a TRACEWIN option), including projections of tune spectral densities. For k-th order[19] space charge modes the coherent frequencies of the highest frequency branches are plotted in normalized form as $\omega/k = \nu_x + F_k \Delta\nu_x$, where F_k are the algebraic factors determined in

[19] Where $k = 2j$ compared with Sect. 5.4.3.

Sect. 5.3.4, evaluated for approximately round beams with split tunes, and ν_x is the rms tune. For reference, the bare tune $\nu_{0,x} = 0.25$ is also plotted; likewise the corresponding space charge shifted value $\nu_x = 0.17$, which is obtained as tune of an rms-equivalent KV-beam.

Note that for the Gaussian beam the lower edge of the single particle spectra in x and y, related to the small amplitude particles, is shifted twice as much downwards from $\nu_{0,x,y}$ as the rms $\nu_{x,y}$. This is in agreement with the doubled electric field gradient in the centre of a Gaussian, compared with the rms equivalent KV-beam, as shown in Fig. 4.1.

Conclusions from Fig. 5.15 are summarized as follows:

- The coherent shift (relative to the rms ν_x) for the plotted "even" modes is always in the positive direction.
- The shift is the larger the lower the order of the mode, where the second order envelope mode falls definitely outside the single particle tune spectrum for the waterbag, but it is close to the edge of the truncated Gaussian beam.[20]
- No Landau damping can be expected for the envelope mode of both, Gaussian and waterbag distributions. This is important with regard to the parametric resonances of Chap. 7 and the externally driven betatron resonances of Chap. 8.
- Third and fourth order modes slightly overlap with the particle tune spectrum of the waterbag case, and efficient Landau damping cannot be expected; for the Gaussian case the overlap is significant, hence a necessary condition for Landau damping would be fulfilled. This issue is further examined by the coasting beam parametric resonance simulations in Sect. 7.4.

5.6 Fluid Models

It is interesting to reduce the kinetic Vlasov model to a much simpler non-kinetic "real space fluid" model. This is achieved by integrating Vlasov's equation over momentum space. The corresponding moments like density, flow velocity, pressure, heat flow etc. form an infinite chain. Its truncation results in a loss of the kinetic nature of the "phase space fluid".

Lund and Davidson have calculated in [16] the spectrum of axisymmetric coherent modes of a 2D "warm-fluid" model beam. Figure 5.16 shows their results compared with the axisymmetric "Gluckstern-modes" as obtained from the kinetic Vlasov-approach for KV-beams (see also Sect. 5.4.3 as well as Sect. 7.3.2.3). The lowest order "Gluckstern-modes" are the fourth order modes, $j = 2$, with instability for $\nu_x/\nu_{0,x} < 0.24$; and in sixth order, $j = 3$, for $\nu_x/\nu_{0,x} < 0.39$ (both in agreement with Fig. 5.13, where ω is normalized to ν rather than ν_0.) In the fluid mode spectrum – not unexpectedly – all the unstable negative energy modes are absent.

---

[20] The largest shift is with the dipole mode in free space, which oscillates with the zero intensity tune $\nu_{0,x}$.

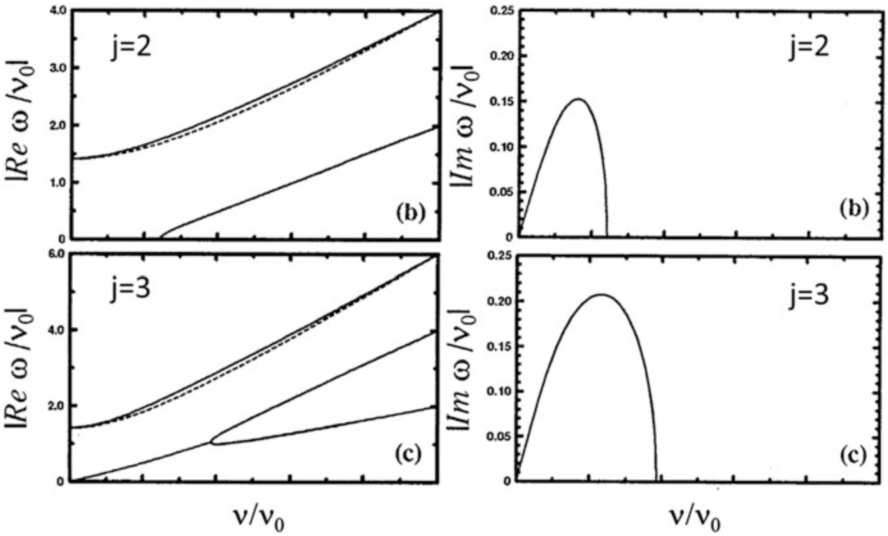

Fig. 5.16 Plot of warm-fluid model coherent mode frequencies (*dotted lines*) and 2D axisymmetric ("Gluckstern type") mode frequencies for KV-distribution (*continuous lines*) versus tune depression and for orders $2j$, with $j = 2, 3$. Shown are normalized real parts of coherent frequencies for both types (*left graphs*); also imaginary parts for the non-fluid "Gluckstern modes" (*right graphs*) (From [16])

Only the highest frequency – positive energy – Vlasov modes are retrieved by the fluid model. Almost coinciding frequencies for these two approaches are noted in Fig. 5.16, which equally applies to higher orders.

References

1. L. Smith, in *Proceedings of the International Conference on High Energy Accelerators*, Dubna, 1963, p. 897 (1963)
2. I. Hofmann, Phys. Rev. E **57**, 4713 (1998)
3. I. Hofmann, Phys. Fluids **23**, 296 (1980)
4. D. Chernin, Part. Accel. **24**, 29 (1988)
5. G. Franchetti, I. Hofmann, M. Aslaninejad, Phys. Rev. Lett. **94**, 194801 (2005)
6. R.L. Gluckstern, in *Proceedings of the Linac Conference 1970* (Fermilab, Batavia, 1970), p. 811
7. C. Lashmore-Davies, J. Plasma Phys. **71**(2), 101–109 (2005)
8. B.B. Kadomtsev, A.B. Mikhailovskii', A.V. Timofeev, Zh. Eksp. Teor. Fiz. **47**, 2266 (1964) [Sov. Phys. JETP 20, 1517 (1965)]
9. L.D. Landau, E.M. Lifschitz, *Electrodynamics of Continuous Media* (Pergamon Press, Oxford, 1960)
10. T.K. Fowler, in *Advances in Plasma Physics*, vol. I, ed. by A. Simon, W.P. Thomson (Interscience, New York, 1968), p. 201. See also R.C. Davidson, N.A. Krall, Phys. Fluids **13**, 1543 (1970)

11. K.Y. Ng, *Physics of Intensity Dependent Beam Instabilities* (World Scientific, Singapore, 2006)
12. F.F. Chen, *Introduction to Plasma Physics and Controlled Fusion*, 2nd edn. (Plenum Press, New York, 1984)
13. I. Hofmann, Part. Accel. **34**, 211 (1990)
14. S. Appel, O. Boine-Frankenheim, Phys. Rev. ST Accel. Beams **15**, 054201 (2012)
15. I. Hofmann, Part. Accel. **10**, 253 (1980)
16. S.M. Lund, R.C. Davidson, Phys. Plasmas **5**, 3028 (1998)

Chapter 6
Beam Mismatch and Halo

Abstract In the presence of space charge perfect matching of the beam is a desirable goal, in particular in high current and high average power linear accelerators. However, discontinuities in focusing geometry, rf frequency or phase etc. are often inevitable sources of mismatch, which result in emittance growth, beam halo and loss. This chapter discusses some basic aspects of the role of rms mismatch with regards to beam halo. Interpreting mismatch and halo is a complex interplay between coherent beam motion, single particle parametric resonance with the core and chaotic motion. A further mechanism – although quantitatively less significant – is density profile mismatch, which is also outlined. Application of this chapter is primarily to linear accelerators, whereas in circular accelerators beam halo is normally understood as a result of nonlinear dynamics driven by external nonlinearities, which are not considered here.

6.1 Fundamental Mechanisms

The danger of producing unacceptable levels of beam loss and thus radioactivity, also in connection with matching, was already recognized in the early pioneering work at LAMPF in Los Alamos in the 1970's–1990's, where much effort went into understanding the origin of halo and beam loss as reported by Jameson in [1] and [2]. The main point of this halo model is that the beam core oscillates in an envelope mode at twice the frequency of the resonant single particle and thus excites a 1:2 parametric resonance.[1] Note that in circular accelerators the subject of beam halo is normally understood as a matter of single particle nonlinear dynamics driven by external nonlinearities, which are not in the focus of this book.

Historically, Reiser was the first to discuss in [3] the conversion of the energy from rms mismatch into emittance growth as a starting point to quantify the connection between rms mismatch and halo.

The model that halo is a mechanism, where the oscillating beam core drives particles to large amplitude due to the 1:2 single particle parametric resonance was

[1]This is a *single particle* parametric resonance, in spite of the coherent beam motion of the driving core, to be distinguished from the *coherent* parametric resonances in Chap. 7.

I. Hofmann, *Space Charge Physics for Particle Accelerators*,
Particle Acceleration and Detection, DOI 10.1007/978-3-319-62157-9_6

found by Jameson in [2]. The important step of quantifying the halo radius by the outer separatrix of the parametric core and that of the mismatch radius was made in this paper as well as in O'Connell et al. in [4].

Further analytical description of the halo and mismatch mechanism was worked out by Gluckstern in [5], and by Gluckstern et al. in [6]. A number of simulation studies by Wangler in [7, 8], Chen and Jameson in [9], Okamoto and Ikegami in [10], Fedotov et al. in [11] and others gave important insight into questions like halo size, the role of different distribution functions and of various focusing configurations. Lagniel in [12] elucidated the role of overlapping resonances in high intensity beams as source of chaotic motion driving particles to large amplitudes by Arnold diffusion.

6.1.1 Characterization of Core and Halo

In the absence of space charge and external nonlinearities, an ideally matched beam has a density profile following its initial distribution, and a distinction between beam "core" and "halo" is unnecessary.

In space charge dominated beams with rms mismatch this is no longer the case. In the literature, primarily of high intensity linear accelerators, different interpretations of the terms core, tail or halo exist. Although a sharp distinction is often not possible, a useful set of definitions is discussed by Jameson in the context of round beams, where the space charge force has a peak at some radius, and drops like $\propto 1/r$ at great distance (Jameson, Los Alamos National Laboratory Report No. LA-UR-94-3753, 1994, unpublished) (see also Fig. 4.1):

- Core: the part of beam within the radius, where the space charge force peaks
- Tail: the region beyond this peak as part of the "natural" distribution[2]
- Halo: particles, which go beyond the tail region due to the action of a space charge induced resonance.

In real beams in concrete linear accelerators the matter of a suitable definition of halo can be more complicated, and other definitions of it have been suggested. In Ref. [13], for example, a method for precisely determining the core-halo boundary is proposed, that allows characterizing the halo and the core regions independently.

6.1.2 Rms Mismatch Conversion

Reiser showed in [3] that an rms mismatched beam has a higher total energy than if it were matched, which includes the potential and the kinetic part of the energy. Under certain circumstances this extra energy can be relaxed into incoherent motion

[2]Jameson calls it "natural", which can be understood also as "initial", hence up to typically 3–4 times the rms width.

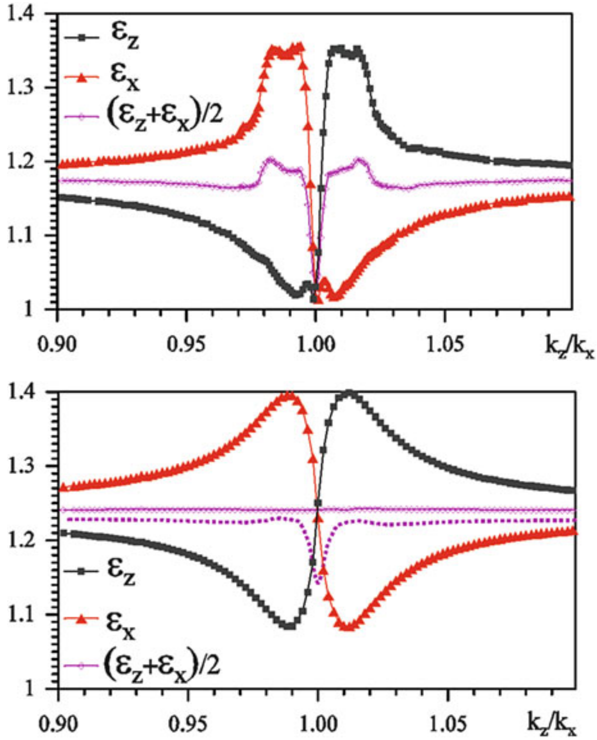

Fig. 6.1 Final rms emittance growth factors in z and x as a function of tune ratio k_z/k_x, for 40% mismatched 2D beam with $k_x/k_{0,x} = 0.95$. Compared are a waterbag (*top*) and untruncated Gaussian (*bottom*) distributions; also shown is averaged emittance growth in z and x (*continuous*), including Gaussian truncated at 1.7σ (*dotted line*) (From [14])

of particles – including formation of a halo – and an associated rms emittance growth. In Reiser's model for isotropic 2D round beams, with equal focusing in both directions, this emittance growth is found to depend primarily on the amount of mismatch, and to a lesser degree on the tune depression.

For multi-dimensional and anisotropic beams the simple round beam models cannot be applied. Franchetti et al. show in [14] that the transfer of mismatch energy into halo in the different degrees of freedom is strongly influenced by the difference in tunes. This is explained in terms of the distance of fixed points from the core, which varies significantly with the splitting of tunes and with anisotropy. An example is shown in Fig. 6.1 for $k_x/k_{0,x} = 0.95$ and a 40% mismatch ($\epsilon_z/\epsilon_x = 1$). The top figure shows curves of ϵ_x, ϵ_z and the average emittance growth, as a function of k_z/k_x, for a waterbag distribution. The bottom figure shows the analogous curves for a non-truncated Gaussian distribution, and in addition it contains a curve of average emittance growth for a Gaussian truncated at 1.7 σ. Each marker is a simulation over 190 betatron periods, long enough to reach saturation.

Note that the averaged rms emittance growth is 24% for the non-truncated Gaussian, independent of the tune splitting. This value is in agreement with an analytical calculation from Reiser's model for round beams [3]. For the truncated Gaussian, instead, the averaged emittance growth (dotted line) drops, and vanishes nearly completely for the waterbag distribution. This is explained as follows: The chosen initial mismatch is in-phase in x and y, which means only the fast (breathing) mode is excited, which has a mode frequency shifted further away from the single particle frequencies than that of the slow quadrupolar mode (compare Eq. 5.15). Thus, the breathing mode cannot sufficiently interact with truncated distributions – compare also with the discussion in Sect. 6.2.2.

6.1.3 Core-Test-Particle Model

In this model the beam core is assumed to keep its density profile unchanged, for example a uniform one, and only rms size oscillations are allowed. Test particles are introduced, which – depending on their amplitudes – can move through the core and also the outside region as described in [2, 4, 7].

For a round and uniform density beam a possible mode of mismatch oscillation is the envelope breathing mode of Eq. 5.16. A particle oscillating beyond the core sees a linear force in r inside the core and, following Fig. 4.1, a strongly nonlinear force proportional to $1/r$ outside, which is weakening the space charge tune shift. A sufficiently large amplitude can shift the tune of a particle closer to the condition $\nu = \omega_f/2$, where the core frequency is twice the single particle frequency. This enables the 1:2 parametric resonance of the single particle type, driven by the mismatch coherent mode (see Ikegami et al. in [15]).

Such an example by Ryne et al. in [16] is shown in the top graph of Fig. 6.2, for $\nu/\nu_0 = 0.5$ in a constant focusing lattice, and an initial radius of the core 0.62 times the matched radius, hence a significant mismatch. A stroboscopic plot of 32 particles, where particles are plotted only at the minimum of the exactly periodic breathing oscillation, is shown over 1000 such periods. Particles, which are initially seeded outside the linear force core region, hence in the tails of the distribution, eventually reach the separatrix marked by the two unstable fixed points. Further on they are carried to large amplitudes by moving along the outer branch of the separatrix. The peanut-shaped boundary just beyond the unstable fixed points gave this kind of diagram the name "peanut-diagram". Note that for stronger tune depression the separatrix turns into a chaotic band.

The bottom graph of Fig. 6.2 shows the corresponding self-consistent simulation for a KV-distribution, which confirms the peanut boundary of the core-test-particle model. The core is unstable under the action of the large mismatch, which proliferates particles into the originally unpopulated tail region, from where they can access the halo region as analysed by Jameson in [2] and Gluckstern in [6].

The peanut-shaped boundary is used by Wangler in [8] to derive scalings for the maximum halo radius of round beams. The dominant parameter in this model is the mismatch parameter μ, defined as ratio of the initial core radius (where the phase space ellipse is upright) to the matched beam radius. In Fig. 6.3 the ratio of the maximum particle amplitude from simulation to the rms size of the matched beam is plotted versus the mismatch parameter μ. The space charge tune depression has a

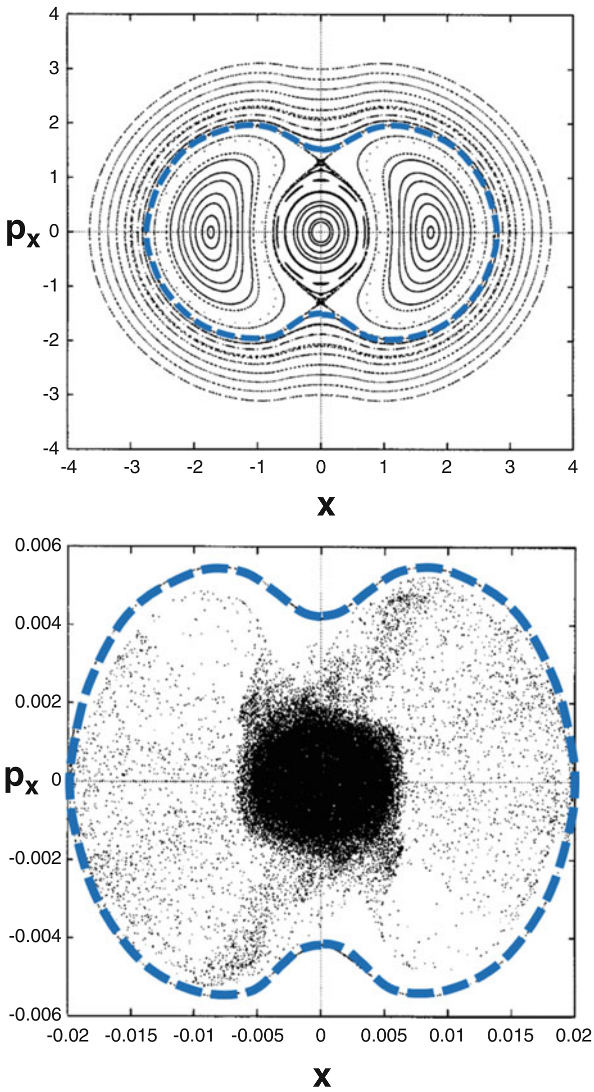

Fig. 6.2 Comparison of core-test-particle model (*top graph*) and azimuthally symmetric selfconsistent simulation (*bottom graph*) for a round KV-beam in constant focusing with $\nu/\nu_0 = 0.5$, and mismatched by the factor 0.62. The outermost peanut-shaped boundary in the bottom graph is taken over from the first curve (*dashed line*) bounding the outer branch of the separatrix in the top graph (Source: [16])

minor effect, also the halo radius predicted by this model is quite insensitive to the choice of initial distribution.

For non-isostropic beams additional factors may influence halo formation and halo sizes, which lead to different criteria. The role of anisotropy on mismatch conversion as introduced in Sect. 6.1.2 can change the simple round beam criteria. Mismatch modes confined to one, or two phase planes with identical parameters, lead to halos up to typically three times the core edge radius; this rule no longer applies if coupled mismatch modes between transverse and longitudinal degrees are

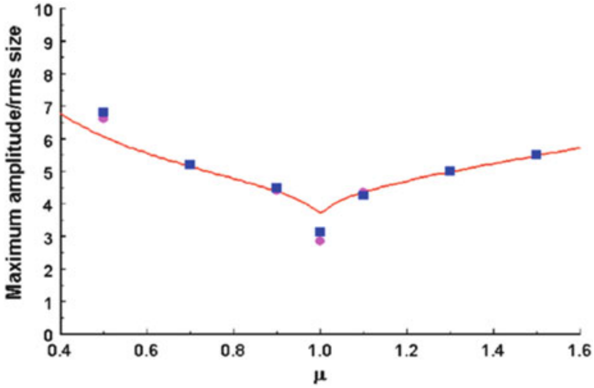

Fig. 6.3 Comparison of maximum halo radius from the core-test-particle model (*curve*) with multiparticle simulations for a waterbag distribution (*squares* and *circles* from different space charge routines) as function of mismatch parameter μ, and for a round beam in continuous focusing (Source: [8])

involved, including anisotropy. Qiang et al. find in [17] that, in cases where the longitudinal focusing exceeds the transverse focusing, certain choices of focusing parameters may lead to a coupled-plane resonance with a theoretically unlimited transverse amplitude.

6.2 Examples of Self-consistent 2D Simulation

The conversion of mismatch into halo, in particular the role of coherent mismatch frequencies and their overlap with the distribution function in this context, is illustrated in the following by comparing TRACEWIN simulations of a Gaussian and a waterbag distribution.

6.2.1 Mismatch Conversion

To characterize the self-consistent interplay between distribution tails and halo formation we first show in Fig. 6.4 an example of a mismatched 2D coasting beam simulation with TRACEWIN and $\nu_{0,x,y} = 0.18$, $\nu_{x,y} = 0.155$ ($k_{0,x,y} = 65°$, $k_{x,y} = 56°$) over 250 FODO cells: The initial mismatch is chosen as 20% increase of the amplitude in x in both cases, which excites a mix of fast as well as slow envelope eigen modes. The resulting coherent envelope mismatch oscillation decays much faster for the Gaussian distribution than for the waterbag. The mismatch energy gets transformed into halo as shown by the phase space plots. For the Gaussian (left centre graph) a more progressed evolution of halo is seen if compared with the waterbag (right centre graph). Likewise, the bottom graphs show approximately 10% rms emittance growth for the Gaussian, but only 6%, and further downstream, for the waterbag.

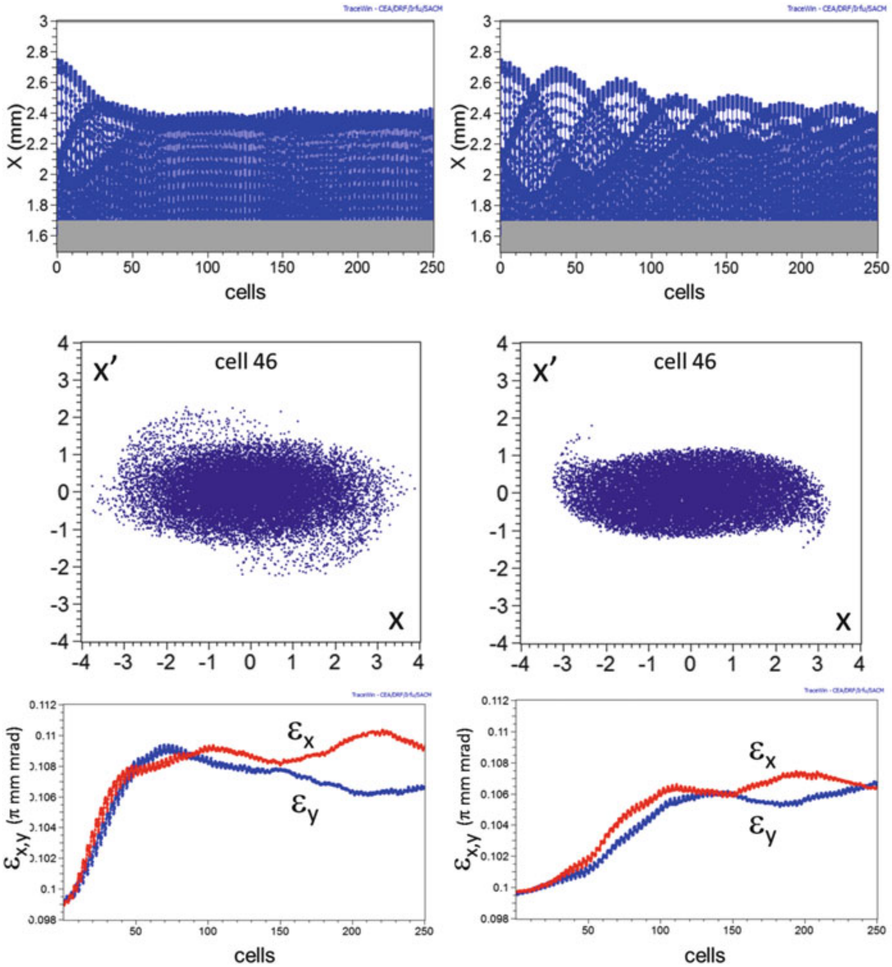

Fig. 6.4 Rms mismatch evolution for Gaussian (*left column graphs*) and waterbag (*right column graphs*) distributions for coasting beam in FODO lattice, $\nu_{0,x,y} = 0.18$, $\nu_{x,y} = 0.155$. *Top*: rms envelopes; *Centre*: Phase space projections in $x - x'$ at cell 46; *Bottom*: rms emittances

6.2.2 *Interpretation*

To visualise the possible interaction of the mismatch oscillation with the particle distribution in phase space we use the tune footprint tools presented in Sect. 5.5.2. In Fig. 6.5 the tune footprints for the case of Fig. 6.4 are shown, but in the absence of mismatch, hence there is no active Landau damping. The coherent frequencies of the fast and slow envelope modes (Sect. 5.3.3.1), divided by two, are plotted as well to evaluate their possible interaction with the single particle spectrum in case of mismatch. For the Gaussian (truncated at 3σ) it is noted that the fast mode sits

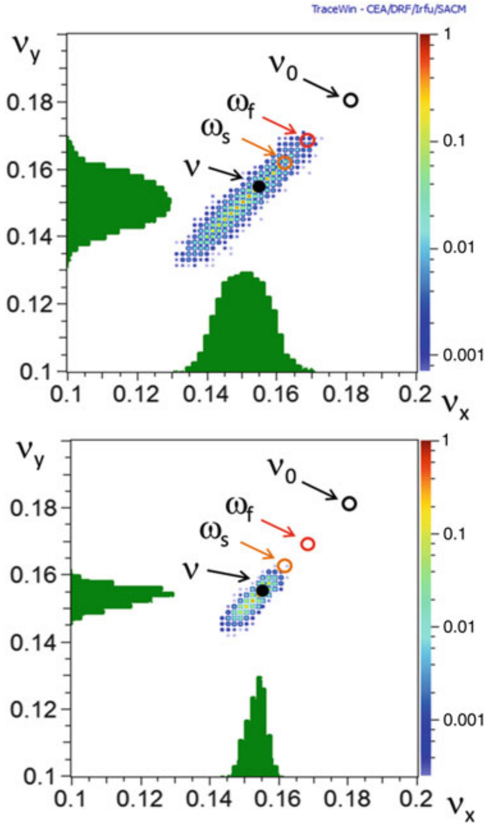

Fig. 6.5 Tune footprint for Gaussian (*top graph*) and waterbag distributions (*bottom graph*) for Fig. 6.4 case, but without mismatch. Also shown are theoretical locations of envelope mode frequencies for the fast and slow envelope modes, $\omega_f/2$, $\omega_s/2$

at the edge of the distribution, and the slow mode in the interior; for the waterbag, both fall outside.

As a consequence, for a beam with mismatch, there are sufficiently many particles directly interacting with the coherent oscillation in the case of the initial Gaussian: they gain amplitude and damp the envelope oscillation with an accompanying rms emittance growth. The initial waterbag distribution, instead, has practically no tails and thus no or only few particles, which immediately get into a halo.[3] Consistently the envelope oscillation is sustained for a longer distance, and only gradually more particles are caught by the resonance. Accordingly, the damping of the mismatch as well as the halo population set in more slowly.

[3]In fact, as pointed out by Jameson in Private communication, it is not necessary for halo particles to be initially far out in the distribution.

6.3 Density Mismatch and Nonlinear Field Energy

Struckmeier et al. introduced in [18] the idea that each density profile is associated with a certain amount of electrostatic field energy. Under certain circumstances it can get "thermalized", i.e. relaxed to incoherent motion with a corresponding increase of the rms emittance. This is the case if at injection into a focusing lattice the density profile is only matched in the rms sense, but not matched to the intrinsic nonlinear space charge potential. For a given distribution function and due to space charge repulsion, the self-consistent density profile is the flatter the stronger the tune depression. Choosing an initial density profile without taking this effect into account, enforces a charge redistribution towards a more uniform one, while the difference in electrostatic field energy gets converted into emittance.[4]

Wangler in [20] suggested an analytical expression for this "nonlinear field energy conversion" in the case of a round beam in constant focusing on the basis of the envelope equations.[5] Using numerical simulation it is also shown that this conversion occurs on the rapid time scale of about $\frac{1}{4}$ of a plasma oscillation, which is typically one focusing cell in a high-current beam. Thus, this relaxation process is much faster than all resonant processes discussed so far.

The model gives an upper limit for the rms emittance growth if full conversion of the nonlinear field energy is assumed. In practical terms the effect is significant only for strong tune depression as in high-current linear accelerators. In [19] it is shown that, based on 3D envelope equations, an analogous model can be developed for 3D bunches. For a spherical bunch in constant focusing, the emittance growth in all directions of 3D is estimated by a similar relation as in 2D,

$$\frac{\epsilon_f}{\epsilon_i} \approx \left[1 + \frac{1}{3}\left(\frac{\nu_0^2}{\nu^2} - 1\right)\left(U_i - U_f\right)\right]^{1/2}, \tag{6.1}$$

where U_f and U_i are normalized measures for the electrostatic field energy of the final, respectively initial state. For a uniform initial density beam $U_i = 0$, a parabolic profile $U_i = 0.057$, and for a Gaussian one $U_i = 0.26$, while – for getting an upper limit estimate – one simply assumes $U_f \approx 0$.

Practically speaking this source of emittance growth is always an issue if the focusing density changes abruptly, and the self-consistent density profile is not allowed to gradually adjust itself. As suggested by Eq. 6.1, this mechanism is particularly relevant for high intensity linear accelerators, where $\nu^2 \ll \nu_0^2$, which means that the electrostatic part in the total energy (in the moving frame) is significant.

---

[4] It is shown in [19] that among all rms equivalent charge distributions the uniform one has the lowest Coulomb energy content.

[5] A similar relation was previously obtained by Lapostolle [21].

References

1. R.A. Jameson, IEEE Trans. Nucl. Sci. NS-**28**(3), 2408 (1981)
2. R.A. Jameson, *Beam-Halo from Collective Core/Single-Particle Interactions*, Los Alamos Report LA-UR-93-1209, Mar 1993; R.A. Jameson, *Self-Consistent Beam Halo Studies and Halo Diagnostic Development in a Continuous Linear Focusing Channel*, LA-UR-94-3753, Los Alamos National Laboratory, Nov 1994, *AIP Proceedings of the 1994 Joint US-CERN-Japan International School on Frontiers of Accelerator Technology*, Maui, 3–9 Nov 1994, World Scientific, pp. 530–560
3. M. Reiser, J. Appl. Phys. **70**, 1919 (1991); A. Cucchetti, M. Reiser, T.P. Wangler, in *Proceedings of the Particle Accelerator Conference*, San Francisco (IEEE, Piscataway, 1991), p. 251
4. J.S. O'Connell, T.P. Wangler, R.S. Mills, K.R. Crandall, in *Proceedings of the 1993 Particle Accelerator Conference*, 1993, ed. by S.T. Corneliussen (IEEE, New York, 1993), p. 3657
5. R.L. Gluckstern, Phys. Rev. Lett. **73**, 1247 (1994)
6. R.L. Gluckstern, W. Cheng, H. Ye, Phys. Rev. Lett. **75**, 2835 (1995)
7. T.P. Wangler, in *Computational Accelerator Physics*, ed. by R. Ryne, AIP Conf. Proc. No. 297 (AIP, New York, 1994), p. 9
8. T.P. Wangler, K.R. Crandall, R. Ryne, T.S. Wang, PRSTAB **1**, 084201 (1998)
9. C. Chen, R.A. Jameson, Phys. Rev. E **55**, 4694 (1997)
10. H. Okamoto, M. Ikegami, Phys. Rev. E **52**, 3074 (1995)
11. A.V. Fedotov, R.L. Gluckstern, S.S. Kurennoy, R.D. Ryne, Phys. Rev. ST Accel. Beams **2**, 014201 (1999)
12. J.M. Lagniel, Nuclear Instrum. Methods Phys. Res. Sect. A **345**, 46 (1994). See also J-M. Lagniel, Chaotic behaviour and halo formation from 2D space-charge dominated beams, LNS/SM/93-42, Dec 1993 and NIM-A vol. 345, no. 3, p. 405, 1994
13. P.A.P. Nghiem, N. Chauvin, M. Comunian, O. Delferriere, R. Duperrier, A. Mosnier, C. Oliver, D. Uriot, Nuclear Instrum. Methods Phys. Res. Sect. A **654**, 63 (2011)
14. G. Franchetti, I. Hofmann, D. Jeon, Phys. Rev. Lett. **88**, 254802 (2002)
15. M. Ikegami, s. Machida, T. Uesugi, Phys. Rev. ST Accel. Beams **2**, 124201 (1999)
16. R.D. Ryne, T.P. Wangler, *AIP Conference Proceedings*, vol. 346 (AIP, New York, 1995), p. 383
17. J. Qiang, I. Hofmann, R.D. Ryne, in *Proceedings of the 19th IEEE Particle Accelerator Conference*, Chicago, 18–22 Jun 2001, p. 1735
18. J. Struckmeier, J. Klabunde, M. Reiser, Part. Accel. **15**, 47 (1984)
19. I. Hofmann, J. Struckmeier, Part. Accel. **21**, 69 (1987)
20. T.P. Wangler, K.R. Crandall, R.S. Mill, M. Reiser, IEEE Trans. Nucl. Sci. NS **32**, 2196 (1985)
21. P.M. Lapostolle, CERN report CERN-ISR-DI/71-6 (1971); also translated as LANL report LA-TR-80-8 (1980)

Chapter 7
Coherent Parametric Instabilities

Abstract This chapter applies the coherent mode framework of Chap. 5 to periodic focusing, where coherent space charge eigenmodes can be subject to parametrically driven, resonant instability as in the case of the well-known envelope instability. Their main characteristic is that they follow a *half-integer* resonance condition between a *coherent eigenmode* of oscillation and the periodic focussing – in contrast with the (also half-integer) single particle parametric resonances discussed in the mismatch context. The subject will be discussed here from various points of view: as Vlasov perturbation theory; in smooth approximation; using the nonlinear rms envelope equations; and finally with multiparticle simulation comparing 2D and 3D models. This chapter is particularly relevant to periodic lattices in linear high intensity accelerators, but in a variety of aspects also to circular accelerators.

Historically, the envelope instability was the first – second order – case of such a coherent instability driven by space charge. Due to its expected occurrence in a stopband at 90° phase advance it was adopted as a serious limit in lattice design for linear accelerators and discussed in much detail, for example in [1–4]. The general theoretical basis for higher than second order modes – also a theory background paper for parts of this chapter – is found in [2].

The terminology *coherent parametric instabilities* is used here to distinguish this particular kind of "space-charge induced instabilities" – as they were called in [2] – from single particle resonant or parametric phenomena. The present notation follows largely a recent review of this subject in [9]. In the literature they are also called *space charge structural instabilities* to account for the importance of the lattice structure as driving mechanism.

The coherent parametric instabilities differ significantly from the *magnet error driven* resonances with space charge to be discussed in Chap. 8, or from the single particle structural space charge resonances in Sect. 4.4.2 for two reasons:

1. They grow exponentially from an initial presence of the corresponding eigenmode on the noise level, or by a suitable mismatch;

I. Hofmann, *Space Charge Physics for Particle Accelerators*,
Particle Acceleration and Detection, DOI 10.1007/978-3-319-62157-9_7

2. They follow a half-integer resonance condition[1] which is also typical for parametric resonances in other areas.

7.1 Parametric Instability Conditions

We start with the well-known single particle parametric resonance. Although all cases considered here are resonant processes, it will be seen that the term *instability* is more appropriate as it characterizes the exponential growth from a small initial excitation.

7.1.1 Single Particle Parametric Resonances

The Mathieu stability diagram (see also [5]) of a single particle in periodic focusing is a well-known example, where a parametric resonance occurs. A particle with an arbitrarily small off-axis perturbation suffers exponential instability if its oscillation frequency ω is subject to the condition

$$\omega = \frac{n}{2}\omega_0, \tag{7.1}$$

with ω_0 the focusing periodicity and n a positive integer expressing the parametric order. The most pronounced case of this parametric resonance – with the widest stopband – is the half-integer case for $n = 1$. In the literature on parametric resonances this 1:2 parametric resonance is frequently called "parametric instability", also "sub-harmonic instability", see in [6].

Another example in beams – in constant as in periodic focusing – is the so-called 1:2 core-test-particle resonance, where the beam core is assumed to perform an periodic envelope oscillation at some frequency ω_0, which drives a single particle with frequency ω out of the core and into a halo (see Sect. 6.1.3).

7.1.2 Coherent Parametric Instabilities

We focus on the *coherent* version of such a parametric instability. An example is the envelope instability in one plane, or in two planes with identical tunes, where instead of a single particle the whole ensemble of particles takes coherently part in

[1]Note that half-integer is relative to a linac focussing or a ring structure period; also integer cases cannot be excluded, but they are much weaker.

the resonant process. Here the 1:2 relationship, as described by Eq. 7.1, is between the focusing periodicity ω_0 and the *coherent* envelope eigenfrequency ω.

Such coherent parametric resonances may also be found in higher order – possibly not beyond fourth order – except for KV distributions, where they are present in arbitrarily high order.

7.1.3 Sum Parametric Instabilities

In parametric resonance theory of mechanical or electrical systems one often deals with several coupled equations, and so-called "combination" resonances are known to exist [6, 7]: two or more eigenmodes of the isolated systems are coupled and jointly enable a parametric resonance via, for example, a sum resonance condition of the kind:

$$\omega_1 + \omega_2 = \omega_0. \tag{7.2}$$

As an example consider two pendula, which are weakly coupled by a spring. Due to coupling a joint periodical length modulation can drive a sum parametric instability if according to Eq. 7.2 the modulation frequency ω_0 is twice the arithmetic average of the individual frequencies $\omega_1,\ \omega_2$.

In the context of beams, sum parametric instabilities can occur between *coherent eigenmodes* of the beam, if the coupling is sufficiently strong. So far this mode has been found to occur between envelope oscillations in different planes, where efficient coupling between the eigenmodes is provided by the direct space charge (see Sect. 7.7).

7.2 Smooth Approximation Approach

Under periodic focusing conditions a fully self-consistent analytical analysis of coherent parametric instabilities is a challenging issue. As will be described in Sect. 7.3, this has so far been undertaken in a rigorous way only for KV-distributions.

An very useful approximation is the "smooth approximation" approach: using the above derived constant focusing eigenfrequencies a parametric resonance condition between these frequencies and the lattice periodicity can be formulated, which will be validated by subsequent computer simulation results.

We make an analogous ansatz to *single particle* nonlinear resonances as in Eq. 4.10, but now the l.h.s. stands for the coherent mode frequency ω for constant focusing following Eq. 5.10. In the notation of circular accelerators, we write the smooth approximation coherent parametric resonance condition as

$$\omega = l\nu_x + m\nu_y + \Delta\nu_{coh,l,m} = \frac{n}{2}N, \tag{7.3}$$

with l, m integers and $\Delta\nu_{coh,l,m}$ the respective coherent tune shift. The factor $\frac{n}{2}$ on the r.h.s is essential for the parametric character of the resonance, where n describes its order, and N stands for the number of structure cells (super periods) per ring circumference. Note the $\frac{1}{2}$, which is crucial: it is absent in the single particle resonance condition Eq. 4.10 and is a characteristic feature of parametrically driven instabilities.[2] For $n = 1$, for example, it stands for the 1:2 coherent parametric envelope instability of Eqs. 5.12.

The analogous expression in linac notation, where $k_{0x,y}$ stands for the phase advance in degrees per lattice period, and $\Delta k_{coh,l,m}$ again for the coherent shift, is

$$\omega = lk_x + mk_y + \Delta k_{coh,l,m} = \frac{n}{2}360°. \tag{7.4}$$

Resonance conditions by using this smooth approximation model are increasingly correct in the limit of weak periodic interruptions, for example for long solenoids with short interruptions, which would yield correspondingly short resonance stopbands. For periodic lattice structures with strong flutter, like alternating gradient, one can still obtain useful guidance about stopband centres as will be shown in the remainder of this chapter and in Chap. 8.

7.3 Vlasov Approach to Coherent Parametric Instabilities

In this section we outline the self-consistent, linearized Vlasov approach to resonant parametric instabilities in periodic focusing as a basis for comparison with multiparticle simulation and more realistic distribution functions.

7.3.1 1D Beams

In [8] Okamoto and Yokoya have explored coherent parametric instabilities in a linearised Vlasov approach for a 1D sheet beam model, assuming a waterbag phase space distribution in an alternating gradient focusing system. Ignoring the spread of betatron frequencies, the model permits deriving approximate expressions for stopbands and growth rates. No instability is found for constant focusing. For periodic focusing they obtain half-integer and integer parametric resonances. They are compared with multiparticle simulation for a 1D Gaussian distribution with the suggestion that high order stopbands are unlikely to play a role in practice.

[2] It is equally absent in the coherent betatron resonances of Chap. 8.

7.3.2 2D Beams

For 2D beams so far only one case of linearised Vlasov analysis of coherent parametric instabilities in periodic focusing exists in the literature, which is the stability analysis of a KV-distribution in a FODO channel in [2].[3]

As already discussed in the constant focusing study of Sect. 5.3, the advantage of using KV-distributions stems from the fact that they allow an analytical integration of Vlasov's equation without further approximation. Similar to the constant focusing case, the eigenmodes can be characterized again by finite order polynomials of the space charge perturbation potential in x, y, where the leading power describes the order of the mode. A third order mode, for example, is characterized by a third order expression in x, y as leading term, with additional lower order terms.[4]

The analysis of [2] assumes a symmetric periodic focusing with equal tunes as well as emittances in both degrees of freedom. Stopbands are defined as regions, where non-zero exponential growth rates are obtained. The main results are summarized in Fig. 7.1, where only even modes from second to fourth order are shown. For easier comparison with the following TRACEWIN simulation results, which are in linac notation, we use here $k_{0,x,y}$, $k_{x,y}$ to characterize betatron tunes in degrees per focusing period.

7.3.2.1 Envelope Modes

In second order the envelope instability stopbands are retrieved. Instability requires $k_{0,x,y} > 90°$, where all stopbands start for $k_{x,y}$ slightly under 90°, with a width shrinking to zero for $k_{0,x,y} \rightarrow 90°$. The smooth approximation expression is $\omega = 2k_{x,y} + \Delta k_{coh,2} = \frac{1}{2}360°$, which should describe the location of the stopband centre and reflect the half-integer 1:2 character of the mode. The asymmetry of the stopbands with respect to 90° confirms the existence of the coherent tune shift $\Delta k_{coh,2}$, which describes the downwards shift of the stopband centre. For further details on this stopband see Sect. 7.4.

7.3.2.2 Third and Fourth Order Modes

The third order mode has a clear three-fold symmetry in phase space, and an asymmetry in real space. It was unexpectedly discovered in a 2D KV-beam transport simulation in periodical focusing by Haber as reported in [10] at a time, when

---

[3] In [2] these modes where simply called space-charge induced instabilities, and the notion *parametric* was not used. The term *parametric* more precisely describes their nature; moreover it distinguishes them from the so-called "Gluckstern mode" instabilities (see Sect. 7.3.2.3) also found in [2], which are not parametric, but intrinsic to the non-monotonic KV-distribution.

[4] The presence of such lower order terms does not mean lower order *modes* are included.

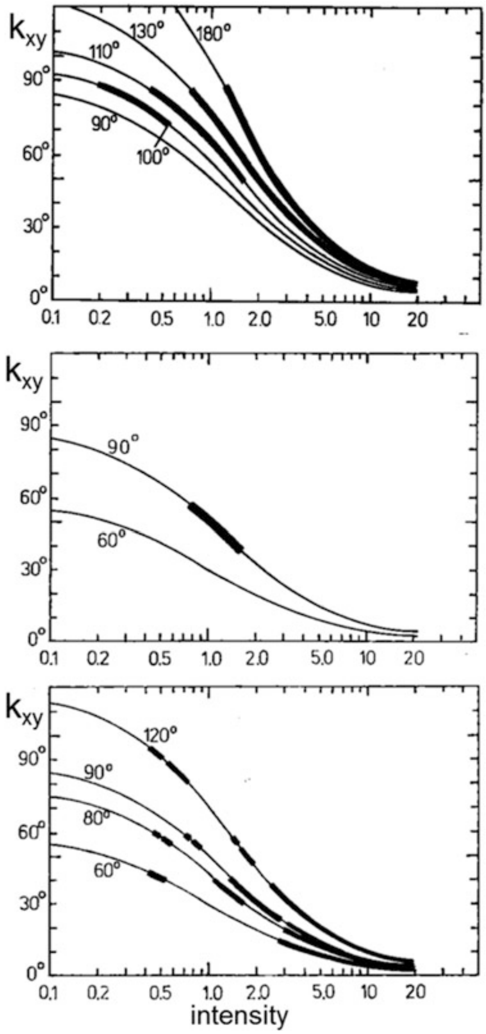

Fig. 7.1 Stop-bands (indicated by *thick lines*) of parametric instabilities obtained by analytical Vlasov analysis for a 2d KV-beam in periodic focusing. Shown are second order (*top*, envelope instability), third order (*centre*) and fourth order (*bottom*) parametric instabilities as function of a dimensionless intensity parameter. Each curve relates intensity to $k_{x,y}$ for a fixed value of $k_{0,x,y}$ in degrees (From [9], original data from [2])

most people in the accelerator community made space charge calculations with an assumed four-fold symmetry in real space.

The third order mode stopband[5] for $k_{0,x,y} = 90°$ starts closely under $k_{x,y} = 60°$. It generally requires $k_{0,x,y} > 60°$ and is found to occur only for $k_{x,y} < 60°$ – analogous to the envelope mode behaviour at 90°. Note that the width of the stopband shrinks to zero for $k_{0,x,y} \rightarrow 60°$. This resonance can be described by $\omega = 3k_{x,y} + \Delta k_{coh,3} = \frac{1}{2}360°$, hence again a half-integer 1:2 coherent parametric instability. For completeness we mention that a further branch of a third order mode

[5]Following [2] this stopband is actually composed of several bands with gaps in between.

starting from $\omega = k_{0,x,y}$ at vanishing intensity is predicted in [11]; this resonance is avoided if – as is usually the case – $k_{0,x,y} < 180°$.

In fourth order a larger number of stop-bands is found, which can be described by $\omega = 4k_{x,y} + \Delta k_{coh,4} = \frac{n}{2}360°$ for different values of n. For $k_{0,x,y} = 120°$ a pair of nearly adjacent stopbands for $k_{x,y} \approx 90°$ is identified, and its width shrinks to zero for $k_{0,x,y} \to 90°$. Different from the above envelope and third order examples, these $n = 2$ modes obey an *integer* parametric relationship. The curve for $k_{0,x,y} = 60°$ suggests that also a fourth order $n = 1$ half-integer mode exists for $k_{x,y}$ slightly under 45°. It is connected with 45° and disappears for $k_{0,x,y}$ below 45°.

Another pair of fourth order stopbands is recognized on the curves for $k_{0,x,y}$= 80°, 90° and 120°, with $k_{x,y}$ somewhat below 60°. Note that according to [11] two well separated branches[6] of modes exist in fourth order, a high frequency one with $\omega_h = 4k_{x,y} + \Delta k_{coh,4,h}$, and a low frequency one – also fourth order – with $\omega_l = 2k_{x,y} + \Delta k_{coh,4,l}$. It can be assumed that a sum parametric resonance $\omega_f + \omega_s = 360°$ helps explaining this pair of stopbands, which is connected with $k_{0,x,y} = 60°$ for vanishing intensity.

7.3.2.3 The “Gluckstern-modes”

This non-parametric instability was found by Gluckstern in a theoretical analysis of round beams in constant focusing in [12].[7] In the fourth order graph of Fig. 7.1 it is described by extended regions of instability for low values of $k_{x,y}$ – theoretically for all values of $k_{x,y}/k_{0,x,y}$ below 0.24, and even below 0.39 for higher than fourth order (see also Sect. 5.4).

It is an artefact of the KV-distribution for sufficiently strong space charge, which is only populated on an *energy surface* in the four-dimensional phase space, and void inside. Two related interpretations have been given (for details see Sect. 5.4): one as coupling between a *negative* and a *positive energy* mode in [13], which allows instability without an extra source of energy; another one in [14] in terms of the strongly non-monotonic character of the δ-function KV-distribution. This provides a source of *free energy* for growth – absent for monotonically decreasing distribution functions. Accordingly, this behaviour of a KV-distribution is found to exist independent of the type of focusing structure.

7.3.3 Comments on Non-KV Distributions

It cannot be overlooked that the diagrams of Fig. 7.1 are only based on KV-beam perturbation theory, also with the restriction of symmetrical emittances and

[6] Precisely speaking, each branch splits further into two adjacent modes.

[7] A historical side note: this instability – frequently called “Gluckstern mode” – was of major concern in the pioneering time of space charge studies for linacs in the 1970s, until it was later recognized as irrelevant for realistic beams.

focussing, hence isotropic. No self-consistent analytical generalization beyond this level has so far been suggested for 2D beams and periodic focusing systems.

The difficulties encountered have to do with the presence of a confining potential and the complicated unperturbed orbits – characteristic of the underlying partial differential equation – as soon as the equilibrium beam is anisotropic or non-KV.

Thus, computer simulation remains the most important tool to model the behaviour of space charge dominated beams. Nonetheless, predictions from KV-theory on coherent parametric instabilities remain a valid tool to examine and interpret computer simulation output. There is evidence in Sect. 7.5.2 that this even applies to the transverse plane of short 3D bunches, where Landau damping appears to work less effectively than in coasting beams.

7.4 KV Envelope Approach

The envelope instability near 90° phase advance has been the subject of numerous detailed theoretical studies over more than three decades, like Struckmeier and Reiser in [4], where different focusing configurations are compared; Lund and Bukh in [15] exploring the fine structure of these modes under a diversity of conditions; and, more recently, Li and Zhao in [16].

Envelope instabilities are also useful to further explore the nonlinear features of a parametric beam instability. Furthermore, they are also a valid starting point for comparison with the multiparticle simulations. We use the 2D and 3D KV-envelope options of the TRACEWIN code for this purpose.

7.4.1 Model Lattice for Simulations

As an example for the KV envelope and following multiparticle TRACEWIN simulations we consider an initially well-matched beam in a symmetric periodic FODO array of quadrupoles, where longitudinal focusing – if needed – is provided by two thin rf gaps in the centre of drift spaces. For simplicity we choose equal emittances in both transverse planes, unless otherwise mentioned. As an example, we set $k_{0,x,y} = 100°$ and show the sample lattice in Fig. 7.2.

Note that for the coasting beam cases in this chapter the rf voltage is set to zero.

7.4.2 Comparison with 2D Vlasov Stopband

Here we use the coasting beam 2d KV-envelope option of the TRACEWIN code and examine the case $k_{0,x,y} = 100°$ in the top graph of Fig. 7.1. Raising the current level in small steps, a visible evidence of envelope instability is found for $k_{x,y} = 88°$.

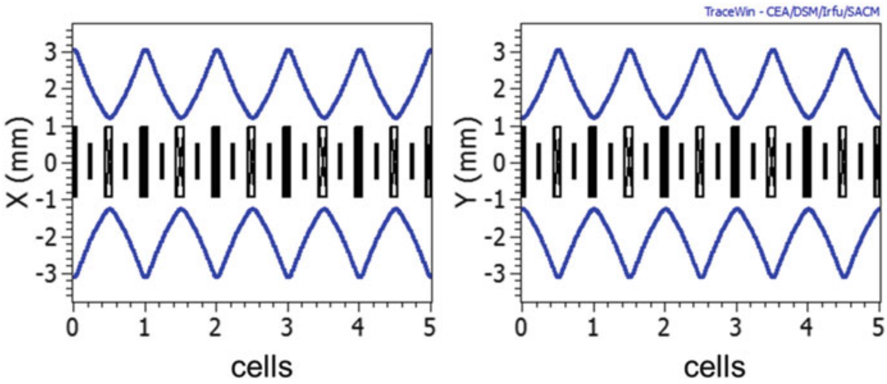

Fig. 7.2 Matched envelopes in sample FODO lattice showing locations of symmetrically positioned rf gaps, and for $k_{0,x,y} = 100°$

The onset of the instability at the opposite, lower edge of the stopband is found for $k_{x,y} = 73°$. Thus, both edges agree very well with the predictions of the perturbation analysis. Corresponding envelopes are shown in Fig. 7.3. The lower edge case shows that the initial growth takes a long distance with many e-foldings, until a sudden rise happens with significant growth. An aperiodic, chaotic pattern with large envelope excursions continues due to the space charge coupling between envelopes. Starting the simulation at this edge of the stopband has an *attractive* effect: a small dilution of space charge due to a growing envelope reduces the space charge defocusing and pushes the system further into the stopband. This continues self-consistently, until the effective $k_{x,y}$ reaches the opposite (low intensity) edge of the – also dynamically evolving – stopband. Starting at the low intensity upper edge, instead, has a *repulsive* effect: the beginning of a dilution of space charge pushes the effective $k_{x,y}$ backwards to smaller values, and growth stops at a small level of envelope perturbation as is shown in the bottom graph of Fig. 7.3.

7.4.3 Envelope Instability for Split Tunes

The so far considered envelope instabilities have occurred simultaneously in x and y due to equal tunes and emittances, which is mostly relevant to linacs.

In circular accelerators horizontal and vertical tunes are usually split by either a fraction of an integer, or an integer or several ones. As example we consider a case, where $k_{0,x}$ is sufficiently above, and $k_{0,y}$ below 90°, hence no envelope instability is expected in y. Figure 7.4 shows the envelope instability for $k_{0,x,y} = 100/80°$ and an intensity such that $k_{x,y} = 82/60°$. Noticeable is the fast exponential rise of the x-envelope from a small initial envelope mismatch with an estimated e-folding of about 10 cells, with no visible increase of the envelope during the first few

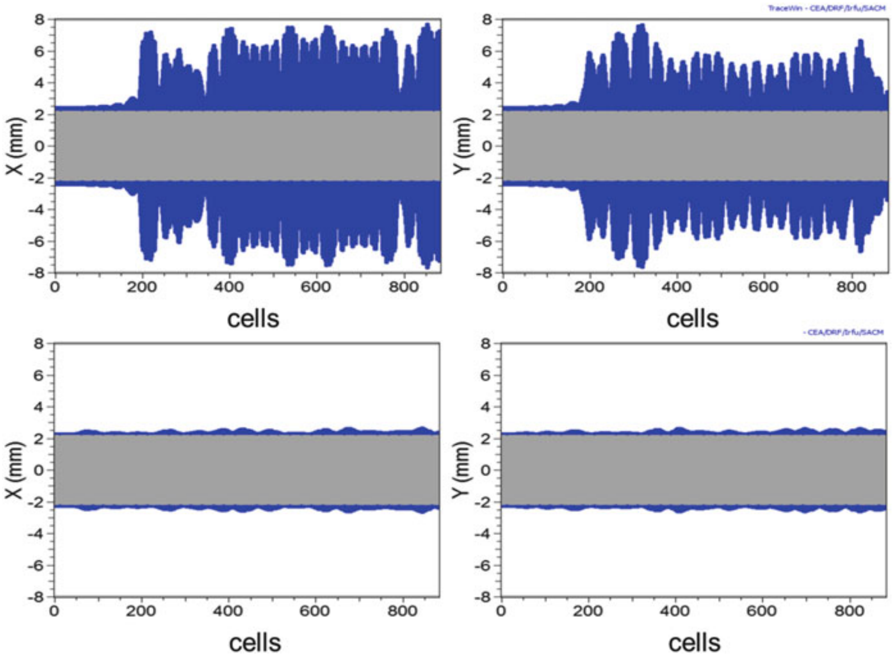

Fig. 7.3 Evolution of envelopes versus cell number for $k_{0,x,y} = 100°$. *Top graph*: at lower (high intensity) edge of stopband with $k_{x,y} = 73°$; *Bottom graph*: upper (low intensity) edge, with $k_{x,y} = 88°$

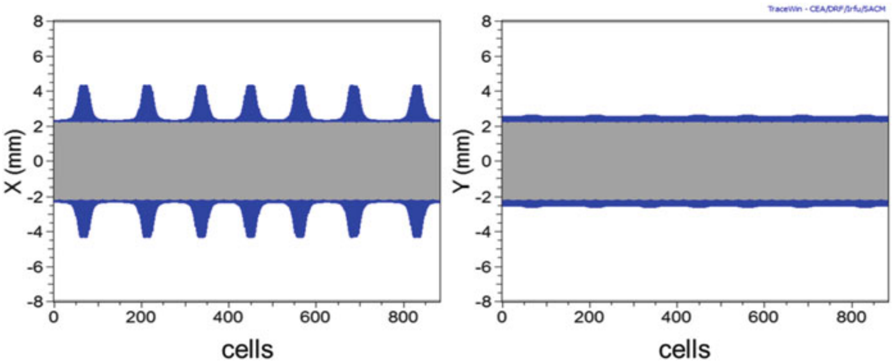

Fig. 7.4 Evolution of KV-envelopes versus cell number for split tunes $k_{0,x,y} = 100/80°$, $k_{x,y} = 82/60°$

e-foldings. Thereafter, a highly periodic pattern of rising and decreasing amplitudes associated with space charge dependent selfconsistent detuning and re-tuning is noted. This periodic, recurrent feature is related to the appearance of a single mode and the absence of any Landau damping effects in the envelope approach. The $x - y$

space charge coupling in the envelope equations causes only a slight modulation in the y-envelope, and the nonlinear chaotic coupling between x and y as in the top graph of Fig. 7.3 is absent.

Note that the separation of modes requires that the space charge tune shift is sufficiently small compared with the tune split.

7.4.4 3D Envelope Instability

For linac applications the envelope instability of 3D short ellipsoidal bunches is of interest. At this level we consider separate envelope modes transversely and longitudinally and leave the coupled sum modes to Sect. 7.7.

7.4.4.1 Transverse 90° Stopband

Results shown in Fig. 7.5 for $k_{0,x,y} = 100°$ and $k_{x,y} = 80°$ reflect a similar behaviour as in the top graph of Fig. 7.3 for 2D, with again a highly aperiodic exchange between x and y amplitudes due to the space charge coupling term in the envelope equations. For the third dimension we have chosen $k_{0,z} = 60°$ – low enough to avoid envelope interaction with the transverse direction. Thus, z plays a minor role here and mainly leads to minor change of the width of the stopband.

We evaluate the maximum amplitudes over a 500 cell long lattice and scan over different $k_{x,y}$, which yields the full stopband as shown in Fig. 7.6. Note that the maximum is usually reached between cells 50 and 100, or much earlier, if a larger initial mismatch is chosen. Comparing with the 2D curve for $k_{0,x,y} = 100°$ from Fig. 7.1 (top graph), it is noted that the 3D stopband in Fig. 7.6 extends about 10°

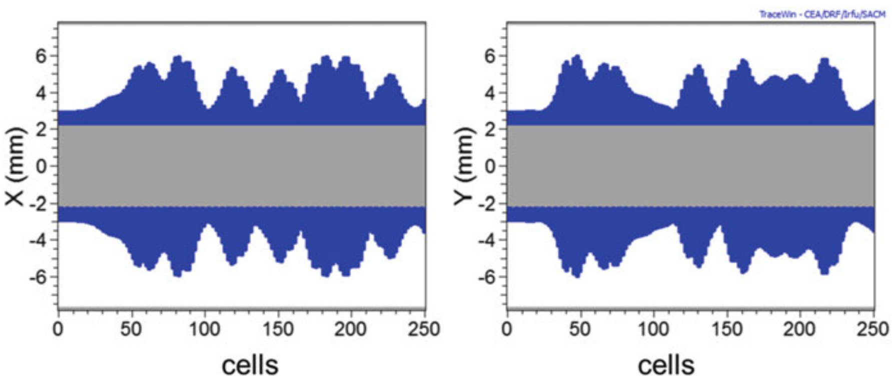

Fig. 7.5 Evolution of KV-envelopes versus cell number for $k_{0,x,y} = 100°$, $k_{x,y} = 80°$

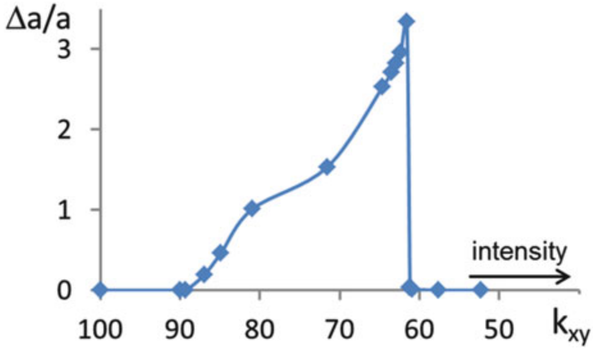

Fig. 7.6 Complete stop-band with relative growth of rms envelopes for $k_{0x,y} = 100°$ as function of $k_{x,y}$ (From [9])

further at the high intensity side. This is due to a difference in the space charge geometry factor for 2D and 3D, which enters into the envelope equations.

The response curve is highly asymmetric, with significant maximum amplitude growth at the high intensity edge. Note the sharp maximum at this edge, with a steep drop to zero for slightly higher intensity, which is a strong coherent effect. This is once again the attractive effect already discussed in Sect. 7.4.2, along with the repulsive effect at the soft opposite edge.

Width and height of this stopband are not independent of each other: it has been shown recently that the emittance growth can be related to the time needed for crossing this stopband [16].

7.4.4.2 Longitudinal 90° Stopband

The behaviour in the longitudinal plane is comparable if $k_{0,z}$ is raised above 90°.

Caution is needed as to the appropriate definition of the cell period, which is not necessarily the transverse period. This matter will be discussed further in the applied discussion of Chap. 10.

7.5 Multiparticle Simulation

Self-consistent PIC-simulation is necessary to model the fully nonlinear behaviour of coherent parametric instabilities. The TRACEWIN code (see Sect. 2.3.2) is employed in the following examples by using the lattice of Sect. 7.4.1.

As first example we evaluate a 2D coasting beam to check the predictions of Fig. 7.1. In practical terms, the 2D coasting beam model can be applied to long bunches in circular accelerators, if the transverse processes are fast enough on the time-scale of the synchrotron period.

In Sect. 7.5.2 we continue with a closer examination of the 90° and higher order stopbands in the case of short 3D short ellipsoidal bunches with reference to linear accelerator applications.

For further aspects of this subject, in the context of interpreting the theoretical and practical significance of the 90° stopband for linear accelerator design we refer to Chap. 10.

7.5.1 2D Coasting Beams

It is of interest to compare the behaviour of simulated non-KV coasting beams with the various stopbands of Fig. 7.1. Although coasting beams cannot be compared directly with short bunched beams in linear accelerators, their behaviour serves as a valuable bridge to the corresponding phenomena in fully 3D beams.

To start with, the resonant features near a quarter integer tune, $k_{0,x,y} \approx 90°$, have some interesting properties of competition between second order and fourth order effects.[8] They are quite different at the upper and the lower edge of the stopband and illustrate the difference between predominantly incoherent, at the upper edge, and coherent response at the lower edge.

7.5.1.1 90° Degree Stopband – Upper Edge

As first example we simulate in Fig. 7.7 a Gaussian distribution beam, with tails cut off at 3σ, and take $k_{0,x,y} = 118°$ ($\nu_{0,x,y} = 0.328$) equally in x and y. The intensity is chosen such that $k_{x,y} = 90.5°$ ($\nu_{x,y} = 0.251$), which – according to Fig. 7.1 – is slightly above the upper edge of the envelope instability stopband.

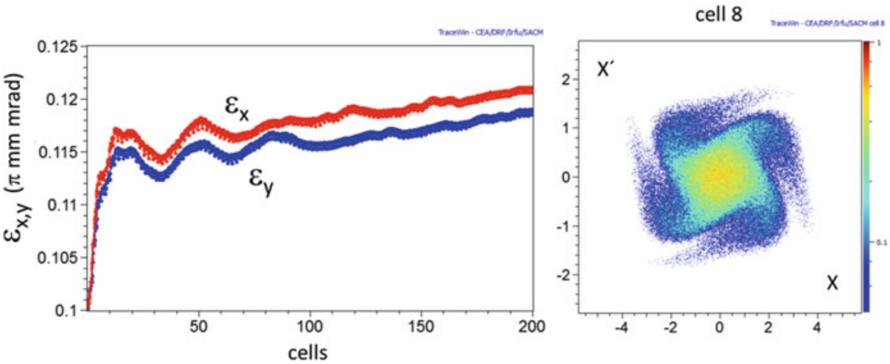

Fig. 7.7 PIC simulation of 2D Gaussian distribution with $k_{0,x,y} = 118°$ and $k_{x,y} = 90.5°$: shown are rms emittances as function of cells (*left graph*) and a $x - x'$ phase space distribution at cell 8 (*right graph*)

[8]Mentioned already in early simulations of a coasting waterbag beam in [17].

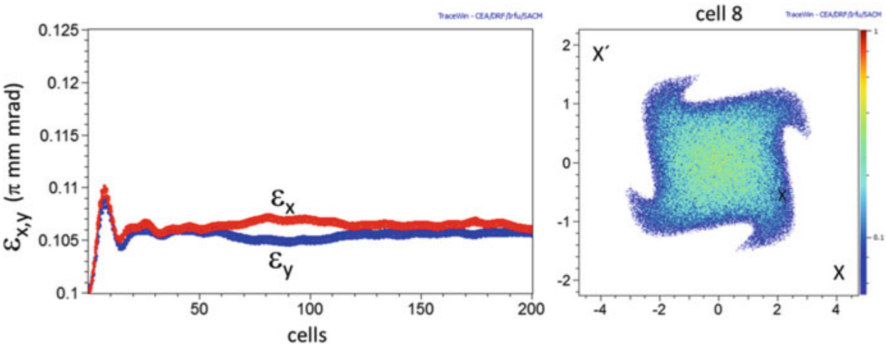

Fig. 7.8 Same as Fig. 7.7 for waterbag distribution

The rapid initial rms emittance growth of 15% is explained as fourth order single particle space charge structure resonance $4k_{x,y} = 360°$, following Eq. 4.10 with $n = 1$ and $N = 1$. As structure resonance it is driven by the relatively strong space charge pseudo-octupole, which is present in the initial Gaussian density profile. All particles overlapping with the resonance stopband initially contribute to the first rise. The resulting space charge dilution leads to gently rising tunes, and more particles enter the stopband from below. The slow continuing growth of the rms emittance must be attributed to this progressive, self-consistent effect on this incoherent resonance.

The waterbag distribution in Fig. 7.8, with its weaker initial space charge pseudo-octupole, shows only slightly more than 5% initial growth, again driven by the same incoherent resonance.

In order to visualize the difference between Gaussian and waterbag it is useful to compare the tune footprints for both cases. The tune spectrum in Fig. 7.9 is obtained over 500 cells, including the dynamical initial phase. In the Gaussian case the incoherent fourth order resonance $4\nu_{x,y} = 1$ results in a migration of particles from initially below $\nu_{x,y} = 0.25$ across this value, which is reflected by the pronounced "wings". This effect is much weaker for the waterbag. It has particles initially within the $\nu_{x,y} = 0.25$ stopband, but not below, and de-tuning stops the resonance at relatively small amplitude.

It is also interesting to locate in Fig. 7.9 the smooth approximation value of fast and slow envelope eigenfrequencies[9]: the fast envelope mode has $\omega_f/2 = 0.29$, the slow one (not shown) $\omega_s/2 = 0.27$. Hence, both are sufficiently far from the parametric resonance condition. The latter would require $\omega/2 = 0.25$, which is consistent with the absence of any coherent envelope instability.

[9]Noting that in a symmetric FODO-channel the slow and fast envelope modes are actually not separate modes.

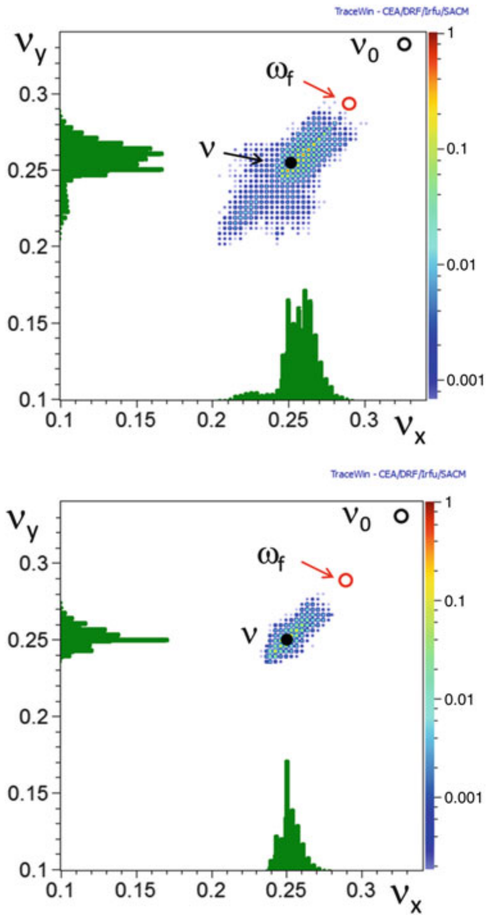

Fig. 7.9 Tune footprints for coasting beams at upper edge of 90° stopband for Gaussian in Fig. 7.7 (*top graph*) and for waterbag in Fig. 7.8 (*bottom graph*), with $\nu_{0,x,y} = 0.328$ and $\nu_{x,y} = 0.251$; also shown is the theoretical location of the envelope mode frequency ω_f (divided by 2), which cannot be excited in this case

7.5.1.2 90° Degree Stopband – Lower Edge

We keep the intensity unchanged, but reduce $k_{0,x,y}$ to 100° such that the resulting $k_{x,y} = 74.2°$ coincides with the lower edge of the envelope instability stopband in Fig. 7.1. The resulting coherent frequency $\omega_f/2 \approx 87°$ (=0.24) is sufficiently close to the smooth approximation coherent resonant condition $\omega_f/2 \approx 90°$.

For the simulation of a Gaussian distribution results in Fig. 7.10 show a strong rms emittance growth exceeding 300% in both planes. The rms value of phase advances (including space charge) shown in the bottom graph of Fig. 7.10 rises due to the emittance growth and levels off – after an intermediate overshoot – at 90°, which indicates the upper edge of the stopband.

Noteworthy is the *intermediate plateau* in the rms emittance between cells 20, 30 and 150, which marks a switch in the type of resonance. For this purpose we compare the phase space plots in $x - x'$ at cell 20 and 50 as shown in Fig. 7.11.

Fig. 7.10 PIC simulation of 2D Gaussian distribution in 90° stopband, with $k_{0,x,y} = 100°$ and $k_{x,y} = 74.2°$: shown are rms emittances (*top graph*) and phase advances (in degrees per cell) as function of cells

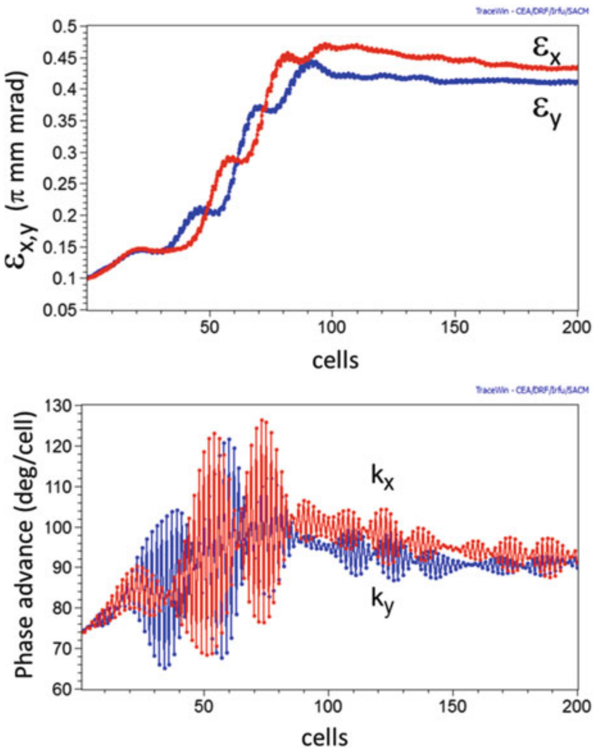

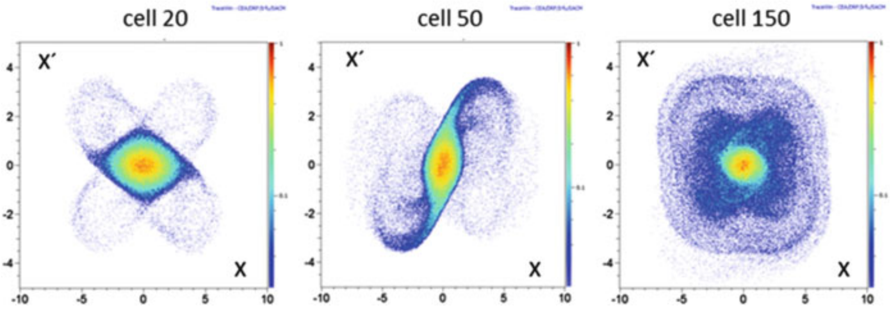

Fig. 7.11 Phase space distributions in $x - x'$ for Fig. 7.10 at cells 20, 50 and 150

Up to the plateau, we identify the incoherent fourth order single particle resonance of Sect. 7.5.1.1, which is followed by the significantly stronger coherent envelope instability.

These findings are further supported by the time evolution of the so-called mismatch and halo parameters, e.g. M_x, M_y and H_x, H_y as shown in Fig. 7.12. M_x, M_y quantify the deviation from the initial values of the matched envelopes [18]. The H_x, H_y are defined as ratios of a fourth order moment to a second order moment,

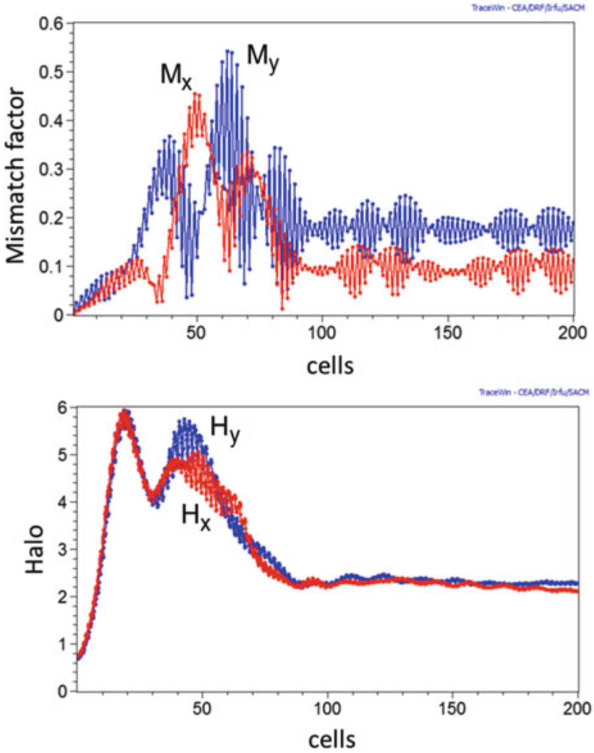

Fig. 7.12 Mismatch and Halo parameters as function of cells for Fig. 7.10

and normalized to zero for uniform density [19]. For a non-truncated Gaussian distribution they are 1, and for a water bag distribution 0.25. Results in Fig. 7.12 indicate a peak of the H_x, H_y between cells 10 and 20, where the fourth order resonance plateau is reached. A peak of M_y between cells 30 and 40 is followed by a peak of M_x, which are a clear measure of the unstable envelope. This growth is accompanied by rising values of the respective rms emittances.

Comparing the details of evolution of rms emittances is also noteworthy: up to the first plateau in Fig. 7.10 both, ϵ_x and ϵ_y grow synchronized, which is due to the single particle fourth order structure resonance. As it is driven by the initial space charge pseudo-octupole, it acts synchronously in x and y. Note that the further growth in the following phase (beyond cell 30) is un-synchronized in x and y. This is typical for an instability situation, where the initial (random) mismatch matters and influences, which emittance grows first.

For comparison, the waterbag distribution, with otherwise identical parameters, yields a somewhat higher emittance growth than the Gaussian as is shown in Fig. 7.13. The initial fourth order activity, however, is completely absent, and the envelope instability starts exponentially from the low-level initial mismatch. Un-synchronized (in x and y) rms emittance growth becomes visible after 30 cells, accompanied by a strong mismatch signal.

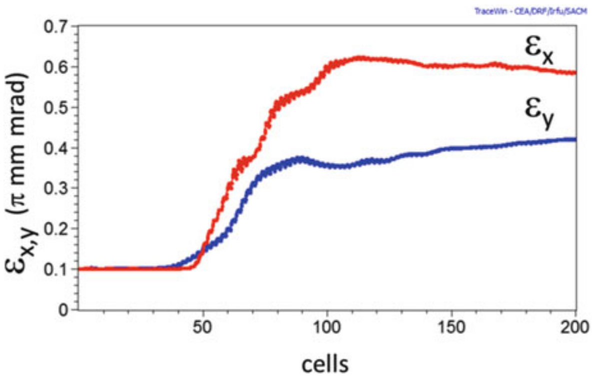

Fig. 7.13 Rms emittances for waterbag distribution in 90° stopband, parameters same as Fig. 7.10

This difference in behaviour between a waterbag and a Gaussian distribution can be illustrated with reference to the tune footprint of Fig. 7.9. Note that the tune distribution of the Gaussian reaches up to ω_f, but not for the waterbag. The coherent resonance cases of Figs. 7.10 and 7.13 are obtained by shifting the footprint with all associated frequencies to the coherent resonance point, where $\omega_f/2 \approx 0.25$ (90°). Then, for the waterbag distribution, no particles overlap with the stopband, and the fourth order single particle resonance phenomenon is absent; for the Gaussian, instead, the r.h.s tail particles overlap, which is consistent with the initial fourth order activity preceding the envelope instability.

In [20] the analogous behaviour, with competing coherent second order and incoherent fourth order resonances close to 90°, is also found in the transverse plane of short 3D ellipsoidal bunches, which is relevant to linac applications (see also Chap. 10).

7.5.1.3 Higher Order Stopbands

The existence of higher order parametric resonances predicted in Fig. 7.1 for KV-beams is examined for non-KV distributions.

Using the definitions of Sect. 7.2 and Eq. 7.4, a third order mode parametric resonance of the kind $\omega_3 = 3k_x + \Delta k_{coh,3} = \frac{1}{2}360°$ (similar in y) is considered. It is associated with 60° phase advance and predicted in Fig. 7.1, where it is calculated for $k_{0,x,y} = 90°$ and an approximate range $40° < k_{x,y} < 60°$. We use similar parameters and choose the intensity such that $k_{x,y} = 47.3°$, thus within the predicted stopband, but close to the lower edge of it.

For a waterbag distribution a clear indication of coherent parametric instability rising from noise is identified in Fig. 7.14, with a 60% rms emittance saturated growth. The three-fold symmetry of the phase space distribution clearly identifies this mode. This picture flips by 180° from cell to cell, hence two cells are needed per period, which also confirms the half-integer parametric nature of the instability. The accompanying self-consistent rms phase advance grows during the evolution of the

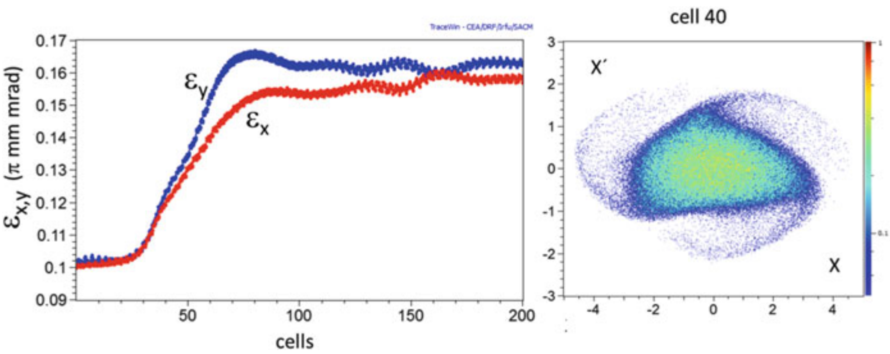

Fig. 7.14 Rms emittances for third order parametric resonance of waterbag distribution with $k_{0,x,y} = 90°$, $k_{x,y} = 47.3°$ and phase space distribution in $x - x'$ at cell 40

instability and reaches saturation at a point, where $k_{x,y}$ has dynamically come close to 60°. By slightly raising the intensity in the simulation to an initial $k_{x,y} = 40°$, the maximum of about 80% rms emittance growth is obtained, and this is the simulation lower edge of the stopband. Surprisingly good agreement is found by comparing this with the Vlasov theory stopband prediction of Fig. 7.1.

For comparison, a Gaussian distribution of the same case, simulated at various points in the assumed stopband, has no indication of parametric instability, with rms emittance growth always <2%.

This difference in behaviour is consistent with the findings of Sect. 5.5 on Landau damping of coherent oscillations. According to Fig. 5.15 the waterbag tune spectrum shows at best marginal overlap with the third order coherent eigenfrequency; in the presence of parametric resonance, Landau damping is insufficient. The Gaussian distribution, in contrast, shows effective overlap with the third order coherent eigenfrequency in Fig. 5.15, which is consistent with the suppression of the parametric instability.

The stopbands in the bottom graph of Fig. 7.1 also predict a fourth order coherent parametric instability $\omega_4 = 4k_x + \Delta k_{coh,4} = \frac{1}{2}360°$. It is associated with 45° and identified in Fig. 7.1 for $k_{0,x,y} = 80°$, within an approximate stopband $30° < k_{x,y} < 40°$. We assume $k_{0,x,y} = 70°$, $k_{x,y} = 37°$ and a waterbag initial distribution. The result of Fig. 7.15 confirms the existence of the predicted fourth order parametric resonance, although with a modest rms emittance growth of 8% only:

As for the third order mode, a Gaussian distribution with the same parameters shows an upper limit of <1% rms emittance growth, hence no evidence of such a resonance. Comparing with Fig. 5.15 the same argument applies as before: the good overlap of the distribution tail with the coherent fourth order frequency again fulfils a necessary condition for Landau damping. The modest overlap for the waterbag distribution – more than in the third order case – might be seen as indication for the reduced growth of the rms emittance in this case.

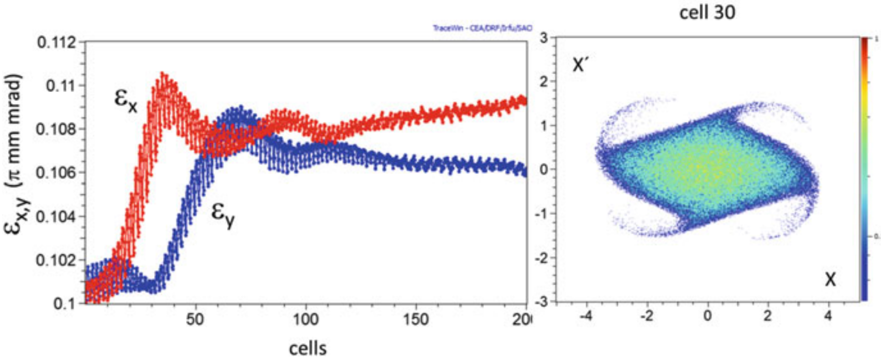

Fig. 7.15 Rms emittances for fourth order coherent parametric instability of waterbag distribution with $k_{0,x,y} = 70°$ and $k_{x,y} = 37°$ and phase space distribution in $x - x'$ at cell 30

Summarizing, Landau damping by the tails of the tune distribution appears to play a decisive role, in particular for Gaussian distribution beams. For the latter, higher than second order coherent parametric instabilities can be assumed benign or absent. For a well-truncated distribution, like waterbag, some moderate effects must be expected.

Questions on the validity of this Landau damping argument for bunched beams with fast synchrotron motion will be raised in the following section.

7.5.2 3D Ellipsoidal Bunches

The space charge issues discussed for 2D coasting beams can provide useful guidance to understand what new elements become important in short 3D bunched beams.[10] First, the additional third dimension allows additional modes of coherent space charge response; second, it also modifies the transverse modes of interaction due to the extra motion of single particles in the longitudinal direction and its possible influence on transverse Landau damping.

The coasting beam findings of Sect. 7.5.1 to a large extent confirm the results of [9, 20] for short 3D ellipsoidal bunches. This includes, for example, the absence of higher than second order coherent parametric instabilities in Gaussian distributions.

Comparison with waterbag simulations, however, raises additional questions. The fourth order parametric resonance near 45° in the waterbag coasting beam simulation of Fig. 7.15 can be compared with the TRACEWIN simulations of short 3D bunches in [9], where a 6D waterbag distribution is used with equal rms

[10]With reference to linacs; long bunches as in synchrotrons or storage rings require different approaches in the third dimension.

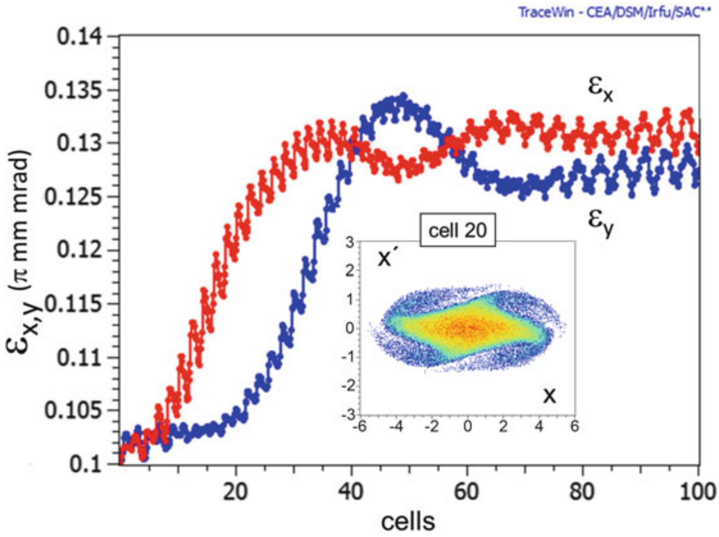

Fig. 7.16 Rms emittances versus cell number showing fourth order coherent parametric instability in 45° stopband, for $k_{0,x,y} = 70°$, $k_{x,y} = 35°$, $k_{0,z} = 120°$ and waterbag distribution (From [9])

emittances in all planes. The same mode is retrieved there for the transverse plane. Its growth is, however, not independent of the phase advance in the longitudinal plane:

- With a moderate longitudinal focusing of $k_{0,z} = 50°$ and $k_z = 17°$, a weak evidence of this mode is found, with only 4% rms emittance growth.
- Raising $k_{0,z}$ to 120°, and keeping the same tunes transversely, the rms emittance growth increases to 30%.

This unexpected result is shown in Fig. 7.16. A possible explanation is that the roughly five times faster effective longitudinal tune k_z in the second example plays a decisive role here. The additional mixing from this fast longitudinal motion could possibly make transverse Landau damping less effective and delay early saturation of the parametric growth.

For additional modes of coupled interaction in short 3D bunches we refer to Sect. 7.7.2, where the sum parametric modes for longitudinal-transverse coupling are introduced; and to Chap. 9 dealing with emittance exchange modes.

7.6 Experimental Evidence of the 90° Stopband

Interpreting space charge effects in the 90° stopband cannot easily be done unambiguously without experimental data. In fact, the discussion about a competitive interplay between a fourth order space charge resonance and the coherent envelope instability gained new momentum with measurements, which are challenging by themselves.

The first measurement of this 90° stopband in an operating RF linear accelerator was reported by Groening et al. in [21] who used the GSI heavy ion linear accelerator UNILAC. For this purpose the first tank of the drift tube linac (DTL) was used, with 15 cells corresponding to approximately 4 full betatron periods within a length of 12 m. The experiment was enabled by the possibility to vary the transverse phase advance over a broad range, for which purpose the relatively light ion $^{40}Ar^{10+}$ was chosen.

Measurements of the transverse emittance were performed with the slit-grid method for a transverse phase advance varied between 60° and 120° and compared with simulations using the DYNAMION code as shown in Fig. 7.17. The four-fold resonance structure is clearly visible in both, the slit-grid experimental data (upper row), and the DYNAMION multi-particle simulation (lower row) for the zero-current phase advance of 100°, where the phase advance with current is 84.6°.

The full width of this stopband was quantitatively confirmed by comparing measured with simulated (using DYNAMION, PARMILA and TRACEWIN) output rms emittances shown in Fig. 7.18. Due to the phase space analysis of Fig. 7.17 there is clear evidence that in this experiment the 90° stopband is dominated by the fourth order resonance, with no indication of the envelope instability, which would have been a theoretical possibility.

The matter was further analysed more recently in [20], where it is re-emphasized that the dominance of the fourth order space charge resonance in the UNILAC experiment is consistent with the relatively short length of the experiment; however, it is also suggested that in measurements over a larger number of cells (typically doubled or less if the initial envelope is not well-matched) the envelope instability can be expected to overtake the fourth order phenomenon as a stronger, but initially delayed phenomenon (see also the related discussion in Sect. 7.5.1).

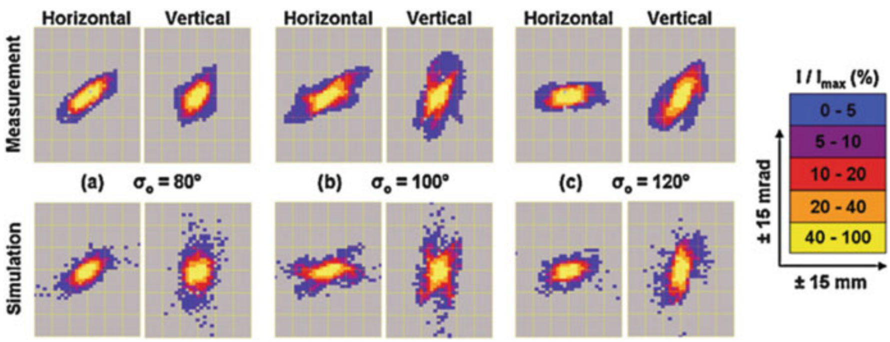

Fig. 7.17 *Upper row*: measured horizontal/vertical phase space distributions at exit of DTL for transverse zero current phase advances 80°, 100° and 120°; *Lower row*: simulations with DYNAMION code (color code referring to beam intensity) (Source: [21])

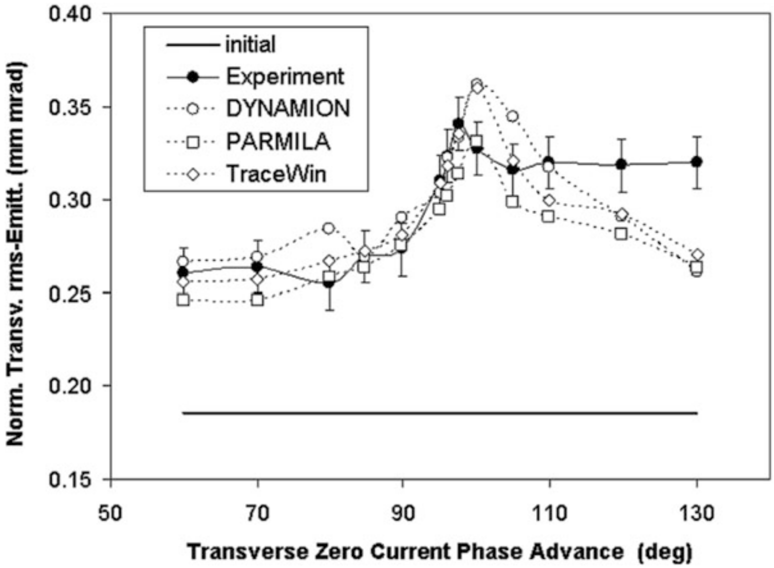

Fig. 7.18 Average of horizontal and vertical rms emittances as a function of the transverse zero current phase advance, with *horizontal line* indicating the initial emittance value. Measured results are compared with simulations by DYNAMION, PARMILA and TRACEWIN codes (Source: [21])

Jeon et al. in [22] interpret their 3D PARMILA code simulations and suggest that for certain parameter conditions "the envelope instability is excited from the mismatch generated by the fourth order resonance".

More experimental data, possibly taken over a larger number of cells, could help resolving the details of space charge physics in this or similar stopbands. Indispensable are clear phase space signatures to identify the mode resonance order, and a careful comparison with theoretical models.

7.7 Sum Parametric Instabilities

The envelope instability near 90° phase advance per cell as *single mode* phenomenon is only a special case of a larger class of coherent parametric instabilities. The existence of additional coherent *sum envelope* instabilities was shown only recently by Boine-Frankenheim et al. in [23]. Following the overview in Sect. 7.1.3, it is the collective analogue to sum parametric instabilities known in theoretical mechanics. As derived in [23] for 2D, and generalized to 3D by Hofmann and Boine-Frankenheim in [24], two even envelope modes in different degrees of freedom can couple via space charge and become unstable under conditions where the individual envelope modes would be stable.

Note here that the single particle second order sum resonance $\nu_x + \nu_y = nN$, known to occur in circular accelerators, is driven by external skew quadrupole components and therefore follows an *integer* resonance condition. It is thus fundamentally different from the *coherent* half-integer resonance condition of the sum parametric envelope mode, which obeys

$$\nu_{0,x} + \nu_{0,y} - \Delta\nu_{coh,s} = \frac{1}{2}N, \tag{7.5}$$

where the coupling force stems only from the coherent space charge force.[11]

7.7.1 Transverse Sum Modes

Following [23] the space charge term in the standard $x-$ and $y-$ rms envelope equations (Sect. 3.2.1) provides the coupling needed for sum instabilities due to the dependence of the force in x on the beam dimension in y, and vice versa.

An approximate resonance condition can be written in smooth approximation by using the expansion of mode frequencies in first order in the tune space charge tune shift, Eq. 5.12, as derived in [23]. For beams not too far from round, and expressing the coherent tune shift of this mode in terms of Δk_{inc}, which is the average incoherent space charge tune shift in x and y, we obtain

$$k_{0,x} + k_{0,y} - \frac{5}{4}\Delta k_{inc} = 180°. \tag{7.6}$$

This equation also indicates that the coherent tune shift of this mode has the same sign as the incoherent space charge tune shift Δk_{inc}, which is assumed as a positive number here. Thus, a sufficient condition to avoid the sum mode is $k_{0,x}+k_{0,y} < 180°$.

The connection with the conventional envelope instability near 90° phase advance per cell as well as the comparison with the smooth approximation criterion of Eq. 7.6 is shown in the "tune scan" of Fig. 7.19 from [23]. It is evaluating the output of envelope simulations in x and y for an initially not perfectly matched beam in a FODO lattice. The resulting mismatch by growing envelopes is plotted colour-coded for a scan in tunes in the $k_{0,x} - k_{0,y}$ plane, with an tune depressed in x and y by an averaged value of $\Delta = 17.5°$. The horizontal and vertical bars indicate the 90° envelope instabilities, which are shifted upwards or to the right due to space charge. The negative diagonal reflects the sum instability, which is also shifted upwards. Note the good agreement with the $\Delta = 17.5°$ smooth approximation result from Eq. 7.6.

[11] Note that in this sum mode section the resonance condition is written using tunes without space charge, and the space charge shifts are absorbed in the correspondingly modified $\Delta\nu_{coh,s}$ of Eq. 7.5.

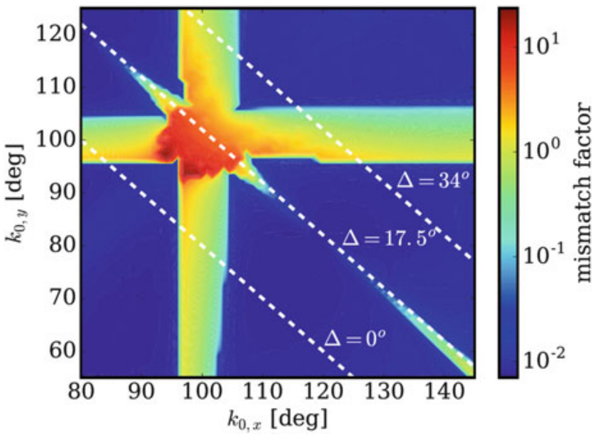

Fig. 7.19 Tune scan of envelope mismatch factors for envelope and sum parametric envelope instabilities (colour coded) for $\Delta = 17.5°$, obtained after 200 cells in a FODO lattice. Also shown (*dashed lines*) theoretical smooth approximation values for different Δ (From [23])

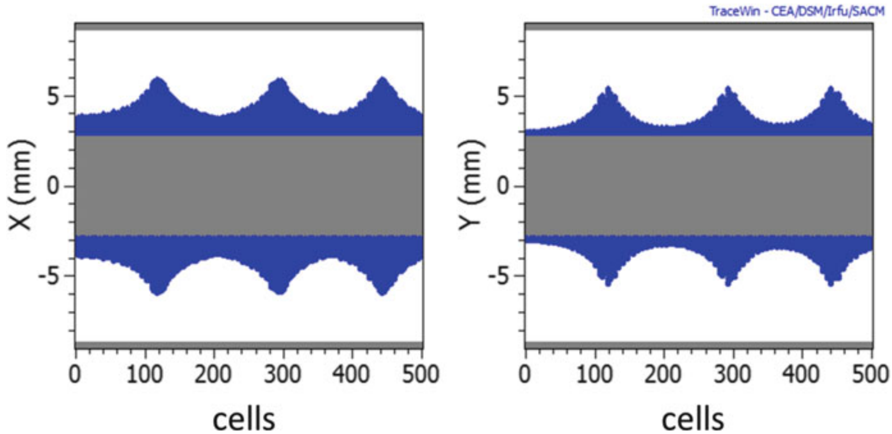

Fig. 7.20 Transverse KV-envelopes versus cell number in FODO lattice for sum parametric envelope instability, with $k_{0,x} = 60°$, $k_{0,y} = 140°$ (From [9])

In [9] the occurence of the sum instability is extended to the transverse plane of an ellipsoidal bunch. Figure 7.20 shows an example based on the KV-envelope equations of a transverse sum mode in a short ellipsoidal bunch. The split phase advances are chosen as $k_{0,x,y} = 60/140°$, $k_{x,y} = 40/123°$. The longitudinal focusing – of minor importance here – is set to $k_{0,z} = 50°$. The pattern of the KV-envelope evolution resembles very much the highly periodical picture of the single envelope instability of Fig. 7.4, where instability and detuning alternate. For the sum mode this happens in both planes, where the coherent phase in the second plane is exactly in phase with the first plane to match the resonance condition.

A 3D waterbag PIC simulation of the same case as in Fig. 7.20, shown in Fig. 7.21, indicates an exponentially rising growth of both rms emittances. The inherent phase space mixing in a PIC simulation suppresses the periodical return

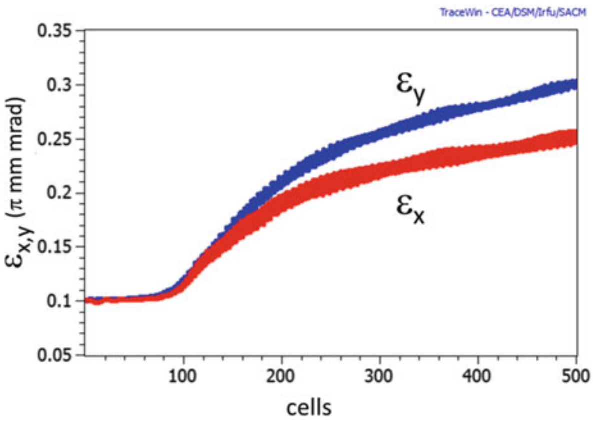

Fig. 7.21 PIC simulation of sum envelope instability case in Fig. 7.20, showing rms emittances growth versus cell number for an initial waterbag distribution (From [9])

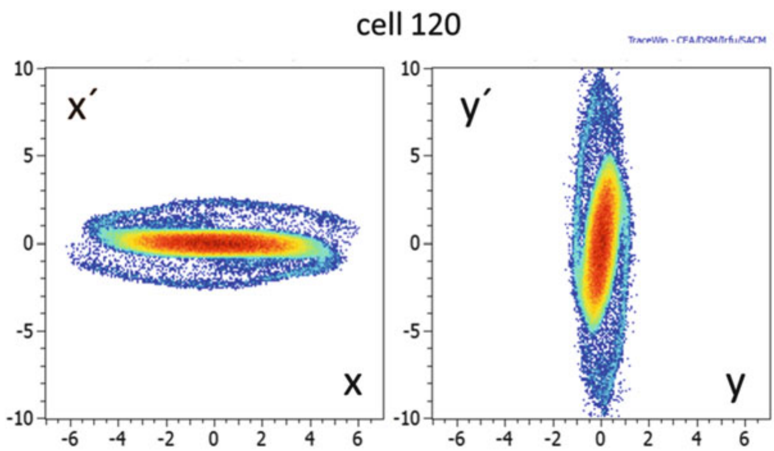

Fig. 7.22 Phase space plots at cell 120 for sum envelope instability of Fig. 7.21 (From [9])

of the KV-envelopes and leads to a significant emittance degradation. Phase space pictures in $x-x'$ and $y-y'$ shown in Fig. 7.22 for the early phase of growth show the stretched ellipses of the coupled mode, which confirms the second order character.

For completeness note that the corresponding equation in circular machine notation, with N superperiods, is

$$\nu_{0,x} + \nu_{0,y} - \frac{5}{4}\Delta\nu_{inc} = \frac{N}{2}. \tag{7.7}$$

This also reflects the difference from the well-known expression for a sum resonance with external skew components.

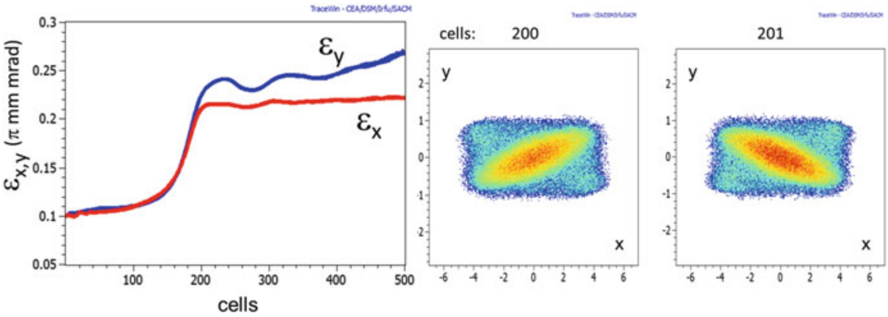

Fig. 7.23 PIC simulation of odd mode sum envelope instability for $k_{0,x} = 60°$, $k_{0,y} = 145°$ and initial waterbag distribution, with rms emittance growth (*left graph*) and real space plots (*right graph*) at consecutive cells 200/201 (From [9])

However, it should be kept in mind that the envelope sum mode would appear in a stopband very close to the fourth order single particle structure resonance $2\nu_x + 2\nu_y = N$, which is normally avoided by a suitable choice of working point.

In addition to the sum mode employing the coupling between two envelope modes, it is found in [23] that a similar coherent sum parametric resonance condition can be obtained if the odd mode in Sect. 5.3.3.2 is considered. From Eq. 5.18 we obtain for equal rms emittances, and not too far from round beams, the approximation

$$k_{0,x} + k_{0,y} - \frac{3}{2}\Delta k_{inc} = 180°. \tag{7.8}$$

Compared with Eq. 7.6, this suggests a coherent term about 20% larger, which amounts to an extra shift of about 4°.

This theoretical result is in good agreement with waterbag simulations in [9] shown in Fig. 7.23. Here, $k_{0,y}$ is increased to 145° to compensate the expected larger coherent tune shift, and a clear evidence of the odd mode sum resonance is recognized. The odd mode is characterized by a self-skewing of the $x{-}y$ projections, which is confirmed by the real space plots in Fig. 7.23. Comparing the plots at the consecutive cells 200 and 201 also confirms that the phase of this coherent self-skewing mode advances by 180° per cell.

7.7.2 Longitudinal-Transverse Sum Modes

Not surprisingly, as shown in [24], a similar sum mode exists between the longitudinal and the transverse directions of a short ellipsoidal bunch, with possible application to linac beam dynamics.

In this case the analogous smooth approximation for the coupling between z and x, y reads as

$$k_{0,z} + k_{0,x,y} - \Delta k_{s,coh} = 180^\circ, \tag{7.9}$$

applied to both, x and y, jointly.[12] Similar to the transverse case, the coherent shift is again positive here, and a sufficient condition to avoid the longitudinal-transverse sum mode is $k_{0,z} + k_{0,x,y} < 180^\circ$.

This is studied in detail in [24], where a FODO lattice as described in Sect. 7.4.1 is used. Based on the 3D KV-envelope equations, an example for $k_{0,z} = 120^\circ$, $k_{0,x,y} = 85^\circ$ and $\Delta k_{inc} = 20^\circ$ is shown in Fig. 7.24. All three envelopes are closely coupled to each other to comply with the sum mode condition, similar as for the purely transverse case.

Again, the 3D PIC simulation for a waterbag shows that the rms emittance growth is significant as shown in Fig. 7.25 (left graph). Surprising is the observation in [24] that the parametric driving force does not need to act on all three degrees of freedom involved in the motion. Acting on one or two of them is enough to

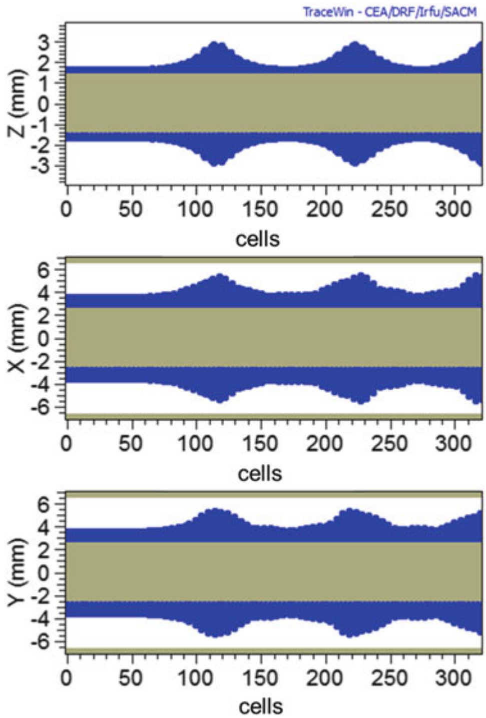

Fig. 7.24 Longitudinal and transverse KV-envelopes versus cell number for 3D parametric sum envelope instability, with $k_{0,z} = 120^\circ$, $k_{0,x,y} = 85^\circ$ (From [24])

[12]Here it is assumed that transverse tunes and emittances are identical, which is roughly the case in linacs.

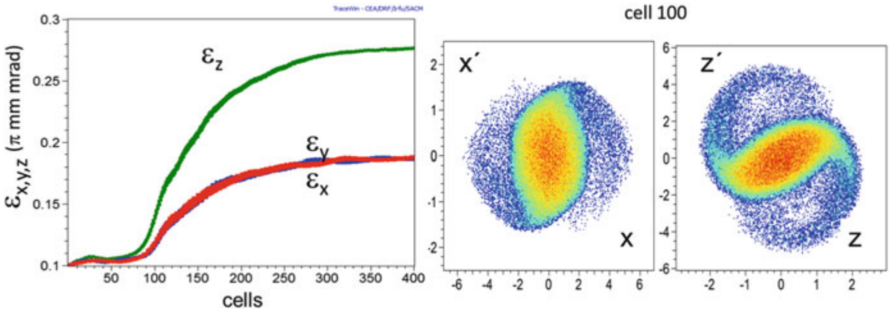

Fig. 7.25 PIC simulation of longitudinal-transverse sum envelope instability in Fig. 7.24, showing rms emittance growth versus cell number for an initial waterbag distribution (*left graph*) and phase space plots at cell 100 (*right graph*) (From [24])

Fig. 7.26 Phase advance evolution across stopband versus cell number for longitudinal-transverse sum envelope instability in Fig. 7.25 (From [24])

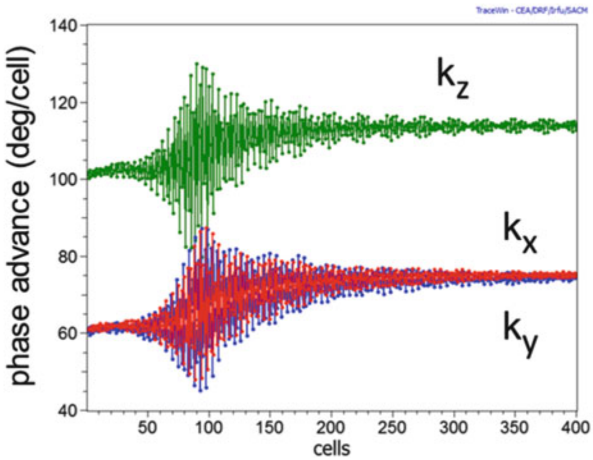

comply with the resonance condition, and the space charge coupling between all three is sufficient. The longitudinal period can, for example, be half the length of the transverse period as is the case in the lattice used here. The rule here is that for the longitudinal-transverse coherent sum instability to occur it is sufficient for the parametric action that the coupled mode eigenfrequency is half the *transverse* lattice periodicity, whereas the longitudinal periodicity can adopt any value, and vice versa.

The emittance growth in z of 170% is significant and equal to the sum of individual growths in x and y, which agree with each other. Note that this is consistent with the fact that the longitudinal degree of freedom has to keep balance with two transverse degrees of freedom. Accordingly, phase space plots in Fig. 7.25 show that the envelope deformation in z is much larger than in x or y.

The stopband of this mode during the evolution of the instability is simultaneously crossed in the longitudinal and transverse directions as shown in Fig. 7.26, where an effective stopband width of over 10° is suggested.

7.8 Dispersion-Induced Envelope Instability

Most of the work on the envelope instability has been focussing on straight lattices – without the effect of dispersion as in circular accelerators. This is largely due to the fact that the 90° condition (e.g. >90° for the zero-current phase advance per lattice period, and <90° for the space charge shifted one) for instability of the usually considered envelope mode has been considered of relevance primarily for linear accelerators.[13]

The *combined effect* of space charge and dispersion on *matched beams* in circular accelerators has been the subject of numerous studies, for example by Venturini and Reiser in [25], Lee and Okamoto in [26]; and by Ikegami et al. in [27] who considered stable (coherent) dispersion modes.

Recently, Yuan et al. reported in [28] about a coupling phenomenon between the envelope mode and the coherent dispersion mode in circular accelerator lattices as another type of sum parametric resonance. They find that due to a confluence of the usual envelope mode with the coherent dispersion mode an additional 120° instability condition emerges: a zero-current phase advance below this value is safe – with regard to this mode –, while a higher value is subject to an instability stopband by the envelope-dispersion coupling. Based on a mode analysis of the coupled system of transverse envelope equations with the dispersion equation, the phenomenon is described by a sum resonance condition – in analogy with the sum envelope modes in Sect. 7.7 – of the kind

$$\Phi_{1,2} + \Phi_3 = 360^\circ, \tag{7.10}$$

where $\Phi_{1,2}$ stands for the phase advance of the envelope modes, and Φ_3 for the dispersion mode. Results from the perturbation theory, compared with the full envelope model and particle-in-cell simulation are shown in Fig. 7.27. The confluence of the envelope mode Φ_1 and the dispersion mode is recognized in the (shaded area) stopband. It is noted that the particle-in-cell result without dispersion only yields an emittance growth for $k_x < 90^\circ$ due to the usual envelope instability; with dispersion a significant growth is obtained within the stopband, which well overlaps with the growth factor $|\lambda|$. Note that the confluence disappears for $k_0 < 120^\circ$.

7.9 Overview Chart on Coherent Parametric Instabilities

The different options of space charge driven coherent parametric instabilities versus zero-current phase advances per structure cell for two planes are schematically

[13]Noting that in circular accelerators lattices a 90° phase advance condition is usually avoided for reasons of structural resonances.

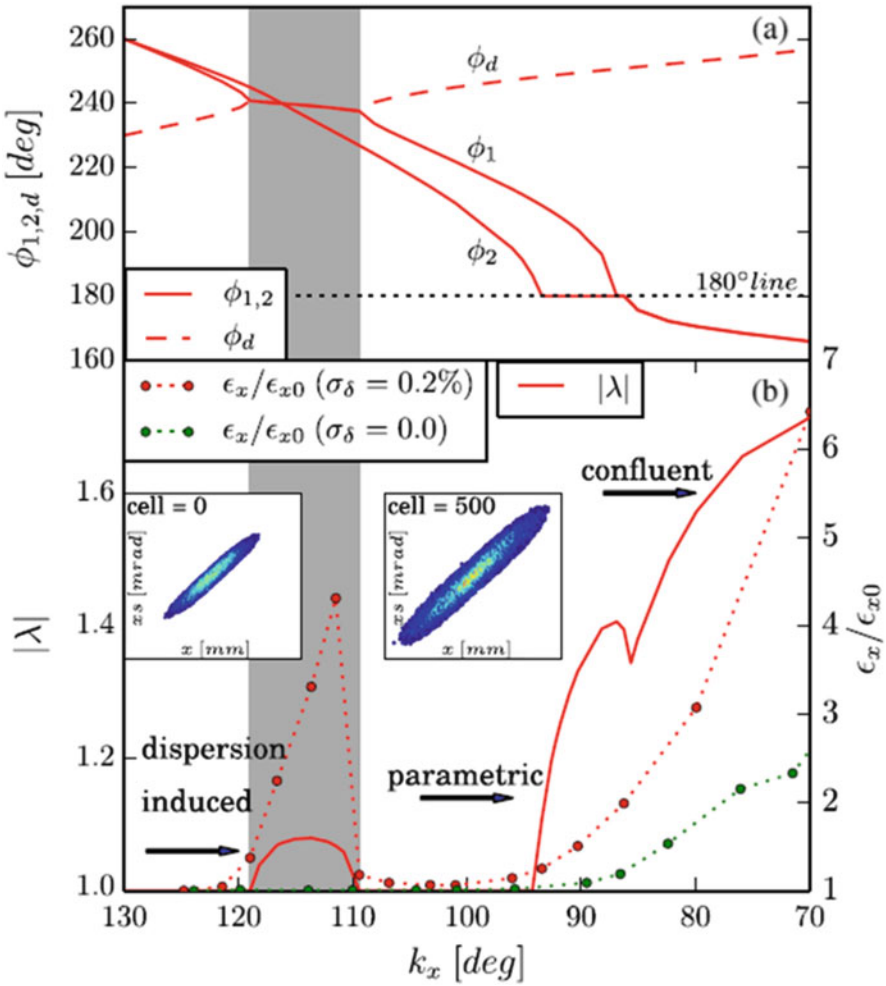

Fig. 7.27 Coupled envelope and dispersion mode instability in periodic lattice with dispersion for transverse $k_0 = 130°$: (**a**) Phase shifts Φ_1, Φ_2 (*solid lines*) and Φ_d ($= 360° - \Phi_3$, *dashed line*) versus space charge depressed phase advance k_x, including dispersion; (**b**) growth factor $|\lambda|$ (*solid line*) from numerical calculation, and normalized emittance growth factor ϵ_x/ϵ_{x0} (*dotted line*) from PIC simulation versus depressed phase advance k_x with and without dispersion, with *shaded area* denoting the stop band of the dispersion-induced instability. *Insets*: $x - x'$ phase space distribution at periodic cells 0 and 500 (Source: [28])

shown in Fig. 7.28. The planes are marked by the second index of $k_{0,i}$, where 1/2 stands either for longitudinal/transverse or horizontal/vertical. The bars have a width and a (positive) shift from zero-intensity limits, which express only schematically the effect of space charge.

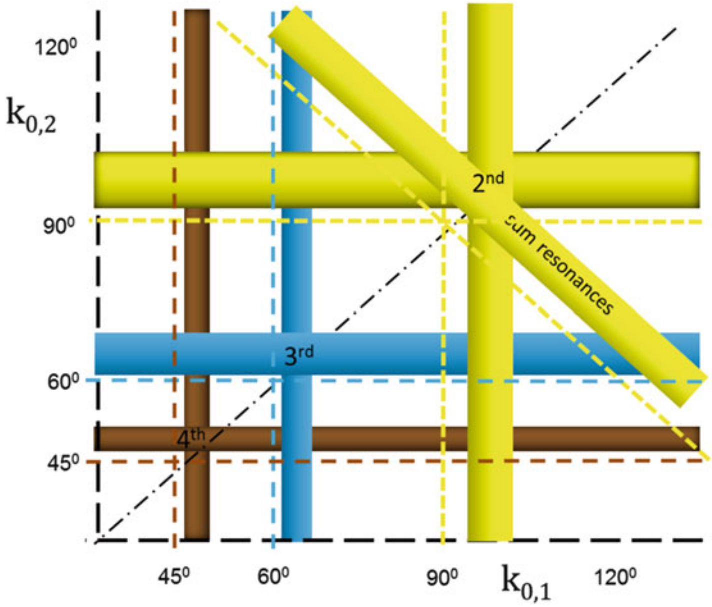

Fig. 7.28 Schematic overview on parametric instabilities identified by simulation, from second to fourth order in plane of zero-current phase advances $k_{0,1}/k_{0,2}$ (longitudinal/transverse or horizontal/vertical). *Dashed lines* in each order indicating location of zero-intensity limits, with bars shifted by space charge (only schematically)

Simulation shows that second order coherent modes, including sum modes, are basically independent of the distribution function. Third and fourth order instabilities, instead, are identified in simulations with waterbag distributions, but with little or no evidence for Gaussian distributions.

Note that single particle resonances of a given order – not shown on this graph – would occur at *twice the phase advances* (besides space charge shifts), which marks the difference between parametric instability and single particle resonance. Also note that the envelope instability stopbands nearly overlap with the fourth order structural space charge resonance discussed above.

References

1. G.R. Lambertson, L.1. Laslett, L. Smith, IEEE Trans. Nucl. Sci. NS-**24**, 933 (1977)
2. I. Hofmann, L.J. Laslett, L. Smith, I. Haber, Part. Accel. **13**, 145 (1983)
3. M.G. Tiefenback, D. Keefe, IEEE Trans. Nucl. Sci. **32**, 2483 (1985)
4. J. Struckmeier, M. Reiser, Part. Accel. **14**, 227 (1984)
5. M. Reiser, *Theory and Design of Charged Particle Beams*, 2nd edn. (Wiley, Weinheim, 2008)
6. F. Verhulst, in *Mathematics of Complexity and Dynamical Systems*, ed. by A.R. Meyers (Springer, New York, 2011), pp. 1251–1264

7. I. Hoveijn, Z. Angew. Math. Phys. **46**, 384 (1995)
8. H. Okamoto, K. Yokoya, Nucl. Instrum. Methods Phys. Res. Sect. A **482**, 51 (2002)
9. I. Hofmann, O. Boine-Frankenheim, Phys. Rev. Accel. Beams **20**, 014202 (2017)
10. L.J. Laslett, L. Smith, I. Haber, Comparison of Instability Theory with Simulation Results, in *Proceedings of the Heavy Ion Fusion Workshop*, Argonne National Laboratory, Argonne, Sept 1978, ANL-79-41, p. 321, Argonne (1978); also I. Haber, IEEE Trans. Nucl. Sci. NS-26, Vol. 3, 3090 (June 1979)
11. I. Hofmann, Phys. Rev. E **57**, 4713 (1998)
12. R.L. Gluckstern, in *Proceedings of the Linac Conference*, Fermilab, Batavia, 1970, p. 811
13. I. Hofmann, Part. Accel. **10**, 253 (1980)
14. I. Hofmann, Phys. Fluids **23**, 296 (1980)
15. S.M. Lund, B. Bukh, Phys. Rev. ST Accel. Beams **7**, 024801 (2004)
16. C. Li, Y.L. Zhao, Phys. Rev. ST Accel. Beams **17**, 124202 (2014)
17. I. Hofmann, Transport and focusing of high intensity unneutralized beams, in *Applied Particle Optics*, Supplement 13C of Advances in Electronics and Electron Physics, ed. by A. Septier, p. 106 ff (1983)
18. T.P. Wangler, RF Linear Accelerators, 2nd ed. (Wiley-VCH, New York, 2008)
19. C.K. Allen, T.P. Wangler, Phys. Rev. ST Accel. Beams **5**, 124202 (2002)
20. I. Hofmann, O. Boine-Frankenheim, Phys. Rev. Lett. **115**, 204802 (2015)
21. L. Groening, W. Barth, W. Bayer, G. Clemente, L. Dahl, P. Forck, P. Gerhard, I. Hofmann, M.S. Kaiser, M. Maier, S. Mickat, T. Milosic, D. Jeon, D. Uriot, Phys. Rev. Lett. **102**, 234801 (2009)
22. D. Jeon, J.H. Jang, H. Jin, Nucl. Instr. Methods A, **832**, 43 (2016)
23. O. Boine-Frankenheim, I. Hofmann, J. Struckmeier, Phys. Plasmas **23**(9), 090705 (2016)
24. I. Hofmann, O. Boine-Frankenheim, Phys. Rev. Lett. **118**, 114803 (2017)
25. M. Venturini, M. Reiser, Phys. Rev. Lett. **81**, 96 (1998)
26. S.Y. Lee, H. Okamoto, Phys. Rev. Lett. **80**, 5133 (1998)
27. M. Ikegami, S. Machida, T. Uesugi, Phys. Rev. ST Accel. Beams **2**, 124201 (1999)
28. Y.S. Yuan, O. Boine-Frankenheim, G. Franchetti, I. Hofmann, Phys. Rev. Lett. **118**, 154801 (2017)

Chapter 8
Magnet Error Driven Resonances

Abstract This chapter considers space charge effects in connection with *externally excited* resonances in circular accelerators. The main focus is on *coherent* phenomena, which are evident in second order gradient as well as skew error driven resonances, and in particular for coasting beams. A direct consequence are *coherent shifts* of resonance conditions beyond the incoherent space charge tune shifts as well as the phenomenon of "coherent advantage" suggesting that the shifts allow higher intensity than would result from an incoherent resonance condition. These externally excited second order resonances are described by coherent *integer resonance conditions* – in contrast with the half-integer resonance conditions of the parametric instabilities. In the field of higher order magnet error driven resonances, in particular when applied to bunched beams with Gaussian distributions, the current understanding is that of dominance of *incoherent* space charge effects, which is briefly discussed in connection with an experimental observation.

Image effects are ignored here, only direct space charge with its intrinsic density perturbations is considered. Image effects are of a certain relevance in dipole modes not considered here (see, for example, the discussion by Kornilov et al. in [1]). Also not under consideration is the role of synchrotron motion except for the discussion in Sect. 8.4, which is not yet sufficiently explored theoretically in the context of resonances and space charge.

8.1 Overview

We consider 2D coasting beams, including anisotropy, and make use of the coherent mode framework as well as the smooth approximation principle from Sects. 5.3 and 7.2. For 1D beam approximations, which have a simpler structure in comparison with 2D, we refer to [2–4].

I. Hofmann, *Space Charge Physics for Particle Accelerators*,
Particle Acceleration and Detection, DOI 10.1007/978-3-319-62157-9_8

8.1.1 Coherent Effects

The importance of space charge in defining intensity limits in proton synchrotrons was understood relatively early. First, at the single particle level, the effect of space charge was only seen as a shift and spread of betatron tunes of individual particles. The importance of *coherent* effects was pointed out by Morin in [5] and Lapostolle in [6] in connection with integer resonance crossing. They realised that what matters is the coherent tune – the tune of the centre of mass – and not the single particle one shifted by space charge. A significant step was the finding of Smith in [7], who claimed that also for second order gradient error resonances of round beams the tune of the *coherent* envelope mode is decisive. The conclusion was that more particles should be acceptable if the coherent mode on resonance matters rather than the single particle tune with space charge.

8.1.2 Smooth Approximation

As for the coherent parametric instabilities, we assume here again smooth approximation resonance conditions, and allow for two-dimensional anisotropic beams, where focusing and emittances may be different in x and y. Such a smooth approximation with space charge and multipole errors in circular machines was studied by Venturini and Gluckstern in [8], based on a perturbation approach of Vlasov's equation. Arbitrarily large space charge effects were assumed with the assumption of isotropic focusing – besides the errors – and round beams. Their not unexpected conclusion is that the "forced" coherent frequencies associated with lattice resonances are part of the "free" eigenfrequency spectrum of the beam as discussed in Chap. 5. Obviously, deviations must be expected, if the constant focusing of the smooth approximation is replaced by alternating gradient focusing.

For second order errors Aslaninejad has extended this in [9] to anisotropic beams, allowing for arbitrary tune and/or emittance ratios as well as including linear coupling modes with space charge.

This justifies the smooth approximation conjecture that coherent resonance takes place whenever an eigenmode of a given order has an integer tune, which brings the mode into a resonance with a suitable error harmonic. For convenience we write the condition in the form (using space charge dependent single particle tunes here)

$$\omega = l\nu_x + m\nu_y + \Delta\nu_{coh,l,m} = n. \tag{8.1}$$

$\Delta\nu_{coh,l,m}$ is the coherent space charge tune shift depending on the specific mode, and n the Fourier component of the error driving the resonance.[1] The main difference

[1] Alternatively nN, if the driving term comes from a structure resonance.

from the parametric resonances of Chap. 7, where the driving force is entirely from space charge, is the absence of the r.h.s. factor $\frac{1}{2}$ characteristic for the 1:2 parametric resonance.

In real accelerators the subject of coherent gradient error resonances and its observation is complex. An overview of Warsop et al. in [10], based on numerical models and observations at the ISIS synchrotron, claims that the gap between models and observations on beam loss is still not closed.

8.2 Second Order Resonances

Basic aspects of coherent effects in second order resonances are described by the following examples, including gradient error and skew error (linear coupling) effects. The former are related to the even modes, the latter to the odd modes of Sect. 5.3.3.

8.2.1 Examples of Gradient Error Resonance

The coherent nature of resonances with gradient errors in an idealized model is demonstrated with examples of KV envelope simulations carried out in the context of early design options of the Spallation Neutron Source (SNS) storage ring in [11]:

- A constant focusing lattice is assumed with tunes $\nu_{0,x,y} = 4.6/4.6$, alternatively split tunes $\nu_{0,x,y} = 6.45/4.6$.
- A gradient error harmonic $n = 9$ is adopted, with variable strength.
- The 2D KV-envelope equations are used to model a long bunch, thus ignoring the effect of the slow synchrotron motion in a real bunch.

Figure 8.1 shows the maximum KV-envelope excursions in x and y, normalized to the initial envelope, for the unsplit lattice with $\nu_{0,x,y} = 4.6/4.6$. The gradient error level is 10^{-3} relative to the unperturbed focusing on harmonic $n = 9$. First, it is noted that in the presence of space charge there is practically no response of the envelope at the single particle tune resonance condition $\nu_{x,y} = 4.5$. Second, the fast (in-phase) and slow (out-of-phase) eigenmodes calculated in Sect. 5.3.3.1 are retrieved. Due to the different coherent shifts the fast mode frequency fulfils the exact resonance condition, $\omega_f = 9$, at the higher intensity, where $\nu_{x,y} = 4.4$; and the slow mode $\omega_s = 9$ at the slightly reduced intensity, where $\nu_{x,y} = 4.47$.

Due to the finite width of the resonance stopband, growth occurs for still lower values of $\nu_{x,y}$, until the sharp drop of the response. The peak growth, when entering the stopband from the l.h.s. edge, is owed to the fact that the onset of envelope instability dynamically shifts the envelope eigenfrequency to higher values – towards the low space charge direction – while the amplitude is increasing. Hence,

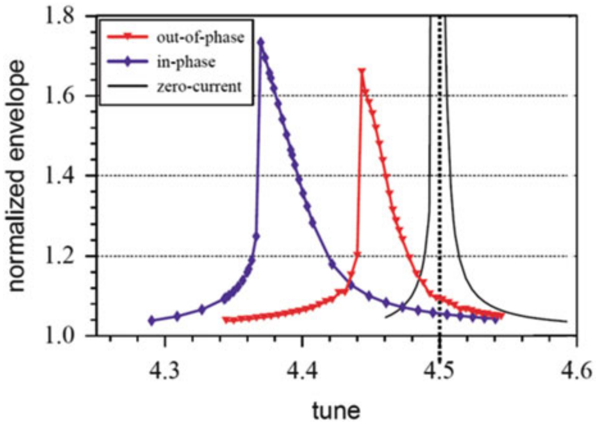

Fig. 8.1 Coherent resonance stopband showing maximum KV-envelope excursions for symmetric and antisymmetric gradient errors at harmonic $n = 9$, with fixed $\nu_{0,x,y} = 4.6/4.6$ and as function of tune $\nu_{x,y}$. For reference, also the zero-current response to the same error is shown (From [11])

the system remains in the effective stopband until it reaches its r.h.s. edge. Entering at the r.h.s. of the stopband the opposite occurs, where a small growth causes a detuning, and the system is pushed out of resonance.

A similar observation of a nonlinear *attractive*, respectively *repulsive* effect of space charge at opposite ends of the stopband is described in the parametrically driven envelope instability phenomenon in Sect. 7.4.2 and Fig. 7.6.

For the split tunes, $\nu_{0,x,y} = 6.45/4.6$, the eigenmodes are also separated, and the harmonic $n = 9$ only drives the envelope resonance in y. Figure 8.2 shows results for different error levels, and with a "normalized tune shift" as abscissa. The latter is defined as $(\nu_y - 4.6)/0.1$, hence increasing intensity in the opposite direction compared with Fig. 8.1. Again, no resonant effect is obtained for $\nu_y = 4.5$ ("normalized tune shift"=1). The different error levels show that the stopband for vanishing gradient error approaches the smooth approximation resonance condition, $\omega_2 = 9$. The latter is described by Eq. 5.14, which leads to a 'normalized tune shift' of 1.6 (the exact value theoretical value of 1.635 is indicated in Fig. 8.2).

The findings in [11] confirm that coherent space charge effects cannot be ignored for coasting beams and second order resonances. Note that the coherent resonance frequency is shifted away from the single particle tune, and in the direction of the zero-intensity tune. This re-confirms the earlier suggestion by Smith in [7] that such coherent effects potentially should allow higher intensities than would be suggested by the single particle resonance condition. In the literature this observation is occasionally called "coherent advantage" – see also Sects. 8.2.3 and 8.2.3 for a quantified discussion of this in multi-particle simulation.

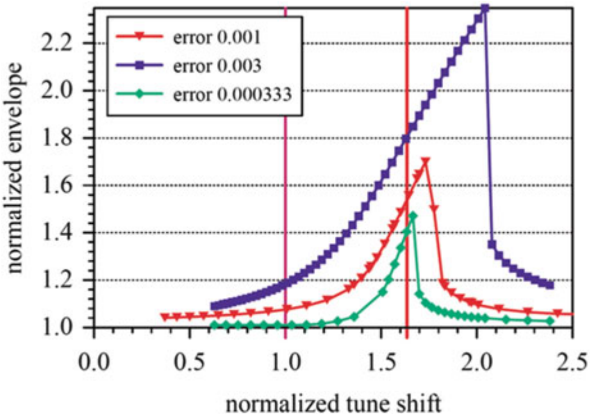

Fig. 8.2 Coherent $n = 9$ gradient error resonance stopband of y-envelope for split (fixed) $\nu_{0,x,y} = 6.45/4.6$, as function of normalized tune shift, and for three different error levels (From [11])

8.2.2 Skew Errors and Linear Coupling

Aslaninejad has quantified in [9] the effect of space charge and anisotropy on the sum and difference *odd* modes with skew errors (linear coupling) by using the Vlasov perturbation approach. Note that the odd difference modes can also become spontaneously unstable – in the absence of external skew errors – if sufficient anisotropy is present as shown in Sect. 5.3.3.2.

Given an external linear coupling term $\propto xy$, the theory allows calculating the linearised theory resonance response on the normalized space charge potential perturbation of the same functional form, which is plotted in Fig. 8.3. Note that at resonance the linearised theory potential perturbation becomes infinite. Nearly no response is found at an assumed single particle resonance condition, $\nu_x = 4$, which ignores the coherent shift. Including the coherent effects, however, shifts the sum mode resonance to a smaller value, and the difference mode to a larger value.

Using the fully nonlinear Chernin equations, the emittance exchange in a stopband of an $n = 1$ difference resonance case is studied by Franchetti et al. in [12]. Results for a lattice with constant focusing and a single skew quadrupole kick per turn are shown in Fig. 8.4, where $\nu_{0y} = 3.2$ is kept fixed, and ν_{0x} is varied. The initial emittance ratio is $\epsilon_r \equiv \epsilon_x/\epsilon_y = 4$, with intensity such that $\Delta\nu_x = 0.09$ and $\Delta\nu_y = 0.2$. For reference, a zero space charge case with the same strength of linear coupling is included (dotted), where resonance occurs at $\nu_{0x} = 4.2$, and emittances are completely exchanged. With space charge and the same strength of linear coupling (dashed line), the exchange is weaker and shifted, both caused by space charge.[2]

The emittance exchange modelled by the second order Chernin equations is always periodical due to lack of Landau damping. For zero intensity the exchange is always complete, but the time needed decreases with larger skew strengths.

[2]Note that the shift on the ν_{0x} axis differs from that on the ν_x axis in Fig. 8.3.

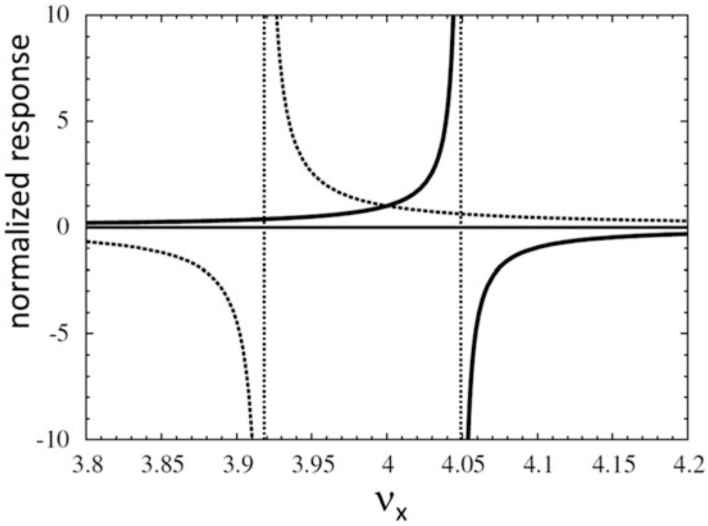

Fig. 8.3 Normalized linearised theory resonance response for second order odd coherent modes in sum ($n = 7$, *dotted curves*) and difference ($n = 1$, *continuous curves*) resonances as function of ν_x (fixed $\epsilon_x/\epsilon_y = 4$, $\nu_y = 3$, $\nu_{0,y} = 3.2$). *Vertical dashed lines* are indicating exact resonance locations (From [9])

Fig. 8.4 Linear coupling difference resonance with coherent space charge effect from fully nonlinear Chernin equations: fixed $\nu_{0y} = 3.2$ and scanned over region $4.1 < \nu_{0x} < 4.25$ ($n = 1$). Shown is the maximum emittance exchange for nominal strength of linear coupling as well as five times smaller, including the zero space charge case for the nominal strength (From [12])

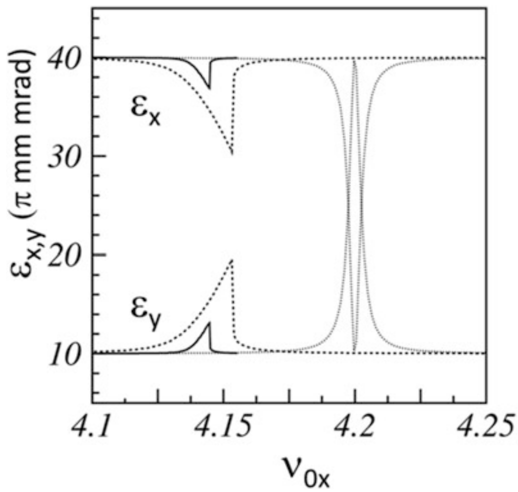

For finite intensity there is a coherent shift by space charge; also a space charge detuning effect with beginning exchange, which limits the amplitude (plotted is the maximum of exchange). For the five times weaker skew strength the maximum exchange amplitude is correspondingly decreased (continuous line). The shift can be calculated theoretically from the small perturbation model in [9], or the eigenmode derivations in Sect. 5.3.3.2, which yields

$$\nu_x - \nu_y = n + \Delta\nu_x \frac{\epsilon_r - 1}{2(1 + \sqrt{\epsilon_r \nu_{0y}/\nu_{0x}})}. \tag{8.2}$$

Inserting numbers we obtain $\nu_x = 4.05$, or $\nu_{0x} = 4.14$, which agrees very well with the location of the stopband for small strength in Fig. 8.4. For comparison, ignoring the coherent r.h.s. term in Eq. 8.2 would yield a stopband at $\nu_x = 4$, or $\nu_{0x} = 4.09$, where obviously no response is seen.

In summary, as in the previous section for gradient errors, coherent shifts are an essential element to determine the proper location of the stopbands as well as explain the nonlinear limitation of the amplitude of exchange by merit of the self-consistent space charge detuning.

8.2.3 PIC-Simulation Examples

The resonant response obtained by second order moment equations is by nature coherent. PIC-simulation is needed to test this coherent behaviour versus the decoherence effect of broadened particle tune spectra in non-KV distributions. For the gradient error resonances this is elucidated here in a few examples.

We take a "toy ring", where the ring "circumference" is assumed to consist of three FODO cells, and $\nu_{x,y}$ is understood as phase advance "per turn".

In the absence of gradient errors we refer to the simulation of Fig. 6.4. It serves as reference case, except for the fact that in Fig. 6.4 tunes are defined per cell, and in the present case per turn, hence multiplied by three.

The $n = 1$ error is realized by extending the length of a single quadrupole in the third cell of the "circumference" by 2%. The smooth approximation resonance condition reads $2\nu + \Delta\nu_{coh} = 1$, where $\Delta\nu_{coh}$ is given by $\Delta\nu$ for the fast, and $\frac{1}{2}\Delta\nu$ for the slow mode (Sect. 5.3.3.1).

In Fig. 8.5 we assume $\nu_{x,y} = 0.5$ to test the behaviour at an assumed *single particle resonance condition*.[3] The theoretical coherent frequencies for fast and slow envelope modes are further away from this assumed resonance condition. No resonance response is found for the waterbag distribution, likewise the accompanying envelopes only show a small, periodical modulation due to the proximity of the gradient resonance. However, a small resonance action is seen for the Gaussian, where the tunes of a fraction of the particles close to the condition $\nu_{x,y} = 0.5$ are pushed above 0.5. The net effect is a 6% growth of the rms emittances over the first 100 turns, which continues with the smaller rate of $\approx$1% per 100 turns.

For comparison, we shift $\nu_{0,x,y}$ upwards to the value 0.6. As expected, again no resonance effect is seen for the waterbag distribution; for the Gaussian Fig. 8.6 indicates a trapping effect of some particles exactly at $\nu_{x,y} = 0.5$, but the rms emittance growth is only $\approx$2% over 200 turns. This justifies the observation that for

[3]Note that in the TRACEWIN code $\nu_{x,y}$ corresponds to an rms value.

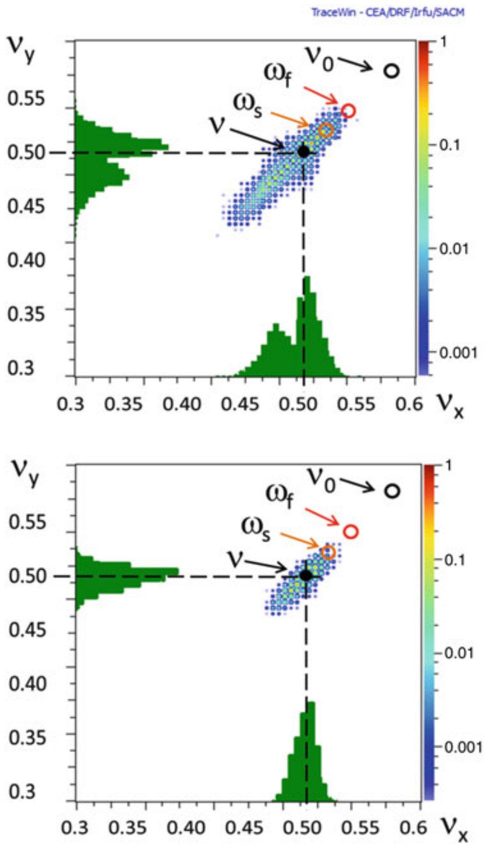

Fig. 8.5 Tune diagrams for coasting beam in FODO lattice with gradient error; rms tunes are $\nu_{x,y} = 0.5$, with $\nu_{0,x,y} = 0.58$. Shown are Gaussian (*top graph*) and waterbag distribution (*bottom graph*); also indicated are the resonant tune values 0.5 (*dashed lines*), and the theoretical envelope mode frequencies

both, waterbag and Gaussian distributions, a part of the particle tune spectrum can be on and even beyond the single particle resonance condition, without significant resonant growth. Hence, the claim of a "coherent advantage" is justified here.

In Fig. 8.7 we set $\nu_{0,x,y} = 0.56$, which has the effect that the slow mode accurately satisfies the coherent resonance condition $\omega_s = 1$. The resonance effect is pronounced in both cases. A significant part of the particle spectrum is pushed above the slow mode coherent resonance condition.

The corresponding KV envelopes in the top graph of Fig. 8.8, where the maximum of an $x-$envelope coincides with a minimum of the $y-$envelope, and vice-versa, confirm the action of the out-of-phase nature of the slow mode. The lower graph shows the mismatch factors of the waterbag case (similar for the Gaussian one), which suggest that the response is highly coherent in the beginning, and more incoherent later on.

Figure 8.9 shows the corresponding rms emittance evolution for both distributions. Most of the emittance growth occurs during the pronounced initial coherent resonance phase; for the Gaussian case a kind of saturation is reached; whereas

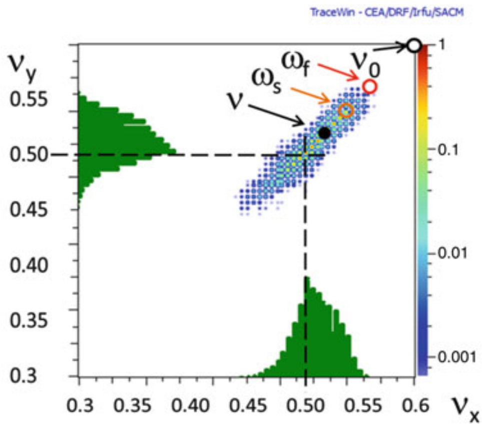

Fig. 8.6 Tune diagram for coasting beam in FODO lattice with gradient error; $\nu_{x,y} = 0.52$ and $\nu_{0,x,y} = 0.6$ for Gaussian distribution

the waterbag emittance continues growing, although in a less coherent fashion than initially. Checking Fig. 8.7, this could be owed to the fact that the low-tune (e.g., low betatron amplitude) part of the broad Gaussian spectrum is too far from the resonance to interact with it.

8.2.4 Coherent Advantage

The above findings on gradient error resonances in coasting beams confirm the early envelope based observation by Smith in [7] that the coherent response generates a space charge gradient force, which counteracts the applied gradient error force and thus leads to a favourable shift of the resonance condition.

Results on the resulting "coherent advantage" are summarized in the following. Note that we define it here as the acceptable factor (e.g. for which no rms emittance growth occurs) by which the intensity can be increased relative to the assumed single-particle criterion, according to which the small amplitude particles (e.g. the lowest tune particles) would just reach the resonance condition.

- The picture of a *coherent resonance crossing* is justified for a compact distribution as the waterbag, but also for the Gaussian. Both allow having a significant part of the single particle tune spectrum under the resonance condition, and without a visible evidence of a resonance effect.
- The more compact waterbag distribution altogether responds in a more coherent fashion, which can be attributed to the fact that the slow as well as fast mode frequencies fall outside the single particle tune spectrum.
- The suggestion of a "coherent advantage" effect is confirmed. Taking Fig. 8.6 as reference for the Gaussian, and Fig. 8.5 for the waterbag distribution, this factor is at least 1.5.

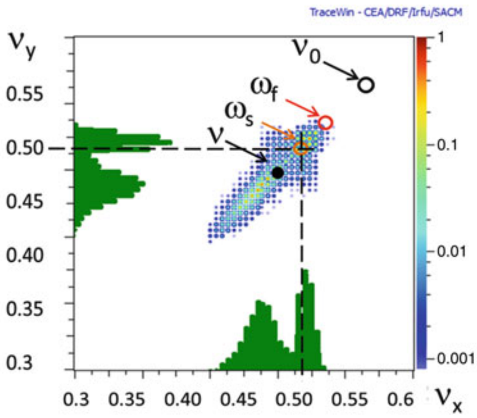

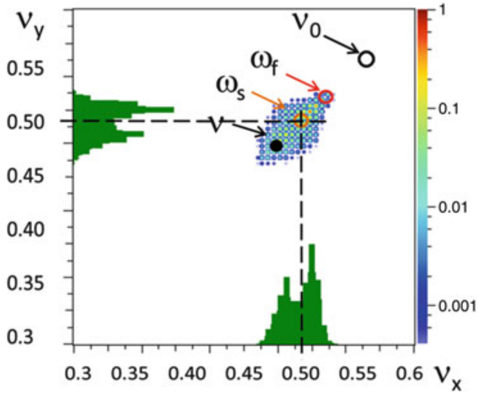

Fig. 8.7 Tune diagrams for coasting beam in FODO lattice with gradient error; with slow mode frequency on coherent gradient error resonance, $\nu_{0,x,y} = 0.56$, $\nu_{x,y} = 0.48$; for Gaussian (*top graph*) and waterbag distribution (*bottom graph*)

The absence of synchrotron motion is essential for these conclusions. In bunched beams, with sufficiently fast synchrotron motion, individual particle tunes migrate due to space charge and chromatic effects, which is expected to mitigate the coherent effect. This subject is still a matter of ongoing research activities.

8.3 Application to Quadrupolar Signals for Diagnostics

The measurement of the coherent envelope or quadrupole mode frequencies is a direct method of observation of a space charge effect. Theoretically, it is closely connected with the discussion of gradient error enforced resonance of the previous section, but here an external kicker is assumed instead.

So-called “quadrupolar pick-ups” have been conceived in many places to measure beam ellipticity via the quadrupole moment oscillations of the beam, which indicate, for example, a mismatch of the injected beam. Ideally they consist of a

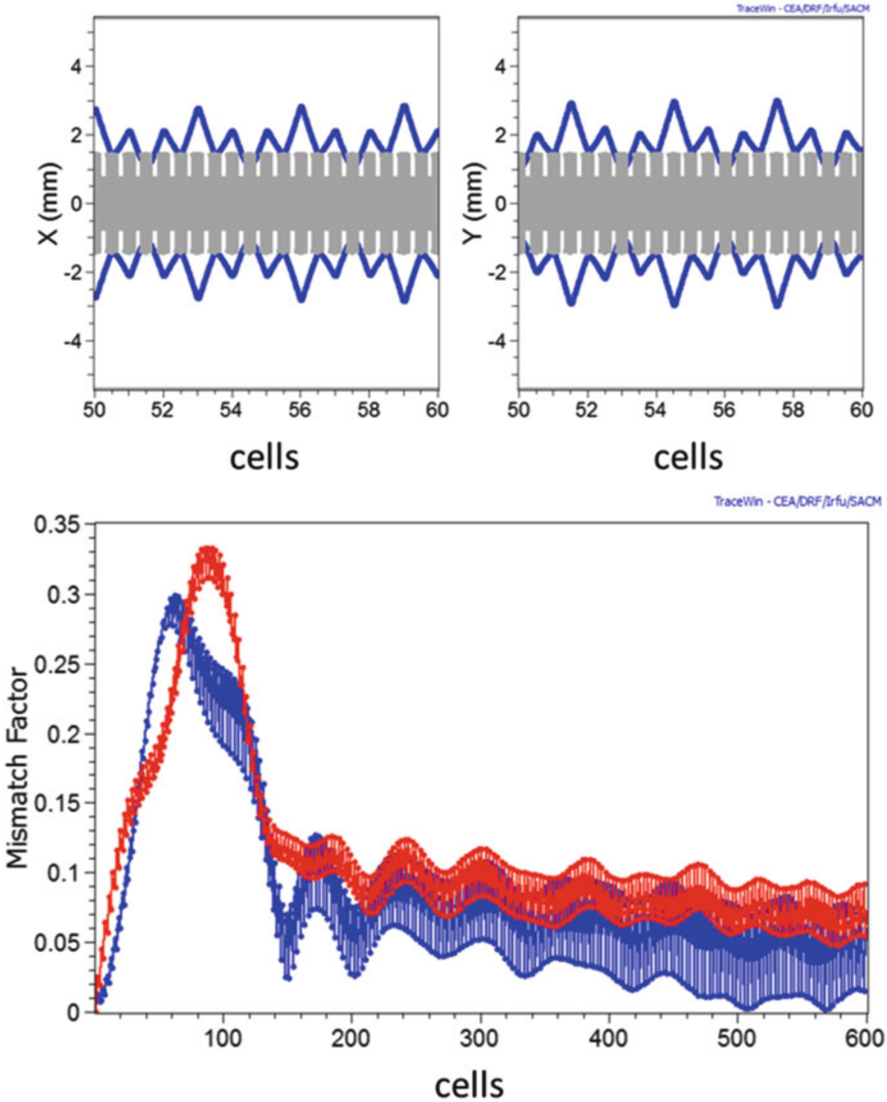

Fig. 8.8 *Top graph*: KV-envelopes for Fig. 8.7 case confirming the out-of-phase nature of the slow envelope mode excited by the gradient error. *Bottom graph*: mismatch factor for same case and waterbag distribution indicating the strongly coherent response in the early phase

horizontal and a vertical pair of plates and a kicker. The difference between sum voltages (needed to suppress the signal from transverse dipole modes) on both pairs is measured. Besides electrostatic versions, which have been used in various accelerators [13–15] also magnetic versions have been developed [16].

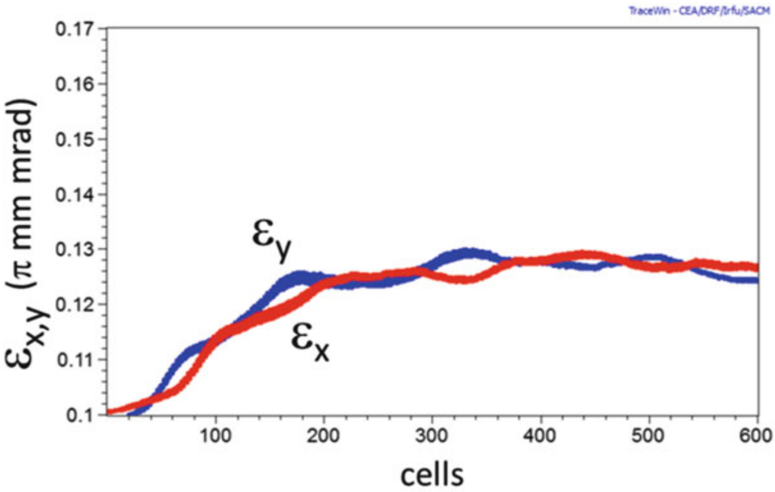

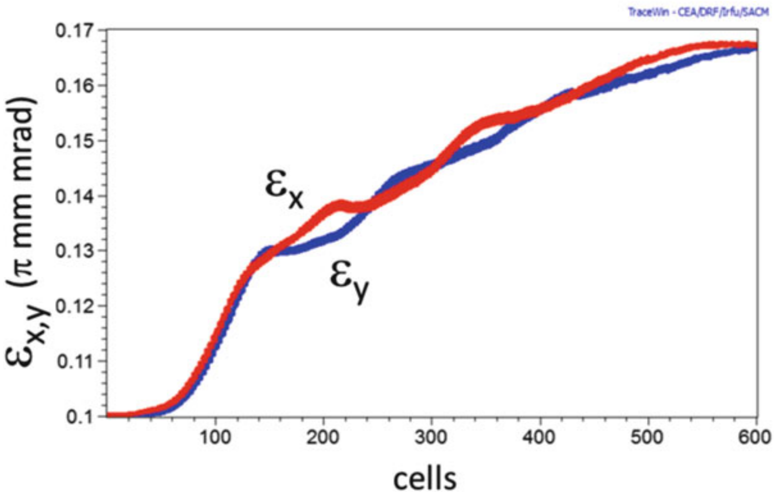

Fig. 8.9 Rms emittance growth for Fig. 8.7 case; for Gaussian (*top graph*) and waterbag distribution (*bottom graph*)

Using the relationship between coherent frequency shift and rms single particle tune shift, the latter can be determined through a measurement of the former. Generally, for all parameters, such a relationship can be determined by using the full second order even mode dispersion equation, Eq. 5.11. For sufficiently split tunes, and linearized in $\Delta\nu_x$, we use Eqs. 5.12 and readily obtain (and similar in y)

$$\Delta\nu_x = \frac{2\nu_{0,x} - \omega_1}{\frac{1}{2}\left(3 - \frac{\eta_0}{(1+\eta_0)}\right)}, \tag{8.3}$$

where ω_1 is the measured coherent frequency. Eq. 8.3 can be used to determine the emittance, and it is identical with the relation derived by Hardt in [17], where it was proposed as diagnostics method in the earlier days of high intensity accelerators.

Using the full dispersion equation, Eq. 5.11, it can be shown that the approximation of Eq. 8.3 is sufficiently accurate for tune splits down to the incoherent rms space charge tune shift. For very small tune splits, $|\nu_{0,x} - \nu_{0,y}| \ll \Delta\nu_x$, Eq. 8.3 becomes inaccurate as pointed out by Metral in [18]. For sufficiently round beams we can employ the formula for unsplit and round beams, Eq. 5.16. For the slow mode branch of it, which relates to quadrupolar oscillations,[4] this is equivalent to

$$\Delta\nu_x = \frac{2}{3}\left(2\nu_{0,x} - \omega_1\right). \tag{8.4}$$

For practical measurements related to quadrupolar modes the effect of realistic distribution functions and possible decoherence of the quadrupolar mode merit further consideration. Simulations of Sect. 8.2.3 suggest that this should not be an issue for well-truncated distributions, like waterbag, but more work is needed to explore this in detail.

8.4 Nonlinear Dynamics and Space Charge

As was shown in previous chapters, coherent shifts of space charge modes become smaller with increasing order of the resonance. Even compact distributions, like waterbag, are likely to overlap with higher order coherent mode frequencies. This enhances the possibility that the resonance response of the density distribution is decohered by Landau damping, and mainly incoherent response matters. Synchrotron motion is likely to further enhance this de-coherence. Under such conditions, fully self-consistent modelling of space charge may not be necessary, and the incoherent tune shift becomes the dominant effect of space charge.

Experiments and simulations on nonlinear dynamics with space charge have grown substantially in recent years. An overview on this and the associated challenges in operating circular accelerators is given by Machida in [19].

In fact, simulations using methods like “frozen-in” space charge – possibly with rms size updates – are significantly faster than fully self-consistent PIC-methods, which matters for very long-term simulations of nonlinear dynamics problems including space charge. The “frozen-in” space charge method has been explored extensively, and compared with experiments, by Franchetti and his collaborators in the context of simulations for benchmarking experiments on nonlinear dynamics

[4]For unsplit focussing and round beams the fast mode pertains to a pure breathing oscillation, which would not leave a signal on quadrupolar pickups.

and space charge at the CERN Proton Synchrotron in [20] (using an octupole to drive the resonance) and at the SIS18 of GSI Darmstadt in [21].

As an example we briefly discuss the SIS18 nonlinear dynamics and space charge benchmarking. It was part of the dedicated experimental campaign S317 in the years 2007–2010 using an ${}^{40}Ar^{18+}$ beam injected at 11 MeV/u and a maximum intensity of 10^9 ions. Its scope was to validate the MICROMAP code (see [22]) predictions by modelling a space charge dominated nonlinear resonance crossing in an ion synchrotron, where the resonance under study was driven by a sextupolar type magnet error. The data included complete sets of measurements comparing beams with and without rf, both at low and at high intensity. The assumed theoretical model has been that space charge (in combination with chromaticity) leads to a periodical crossing of the resonance due to synchrotron motion. This has a scattering effect[5] on the crossing particles, which should lead to emittance growth and beam loss. The observed correlation between transverse beam loss and simultaneous bunch length shortening has been taken as confirmation for this space charge dominated periodic resonance crossing model.

For illustration, quantitative results of code predictions with the experimental results at a horizontal tune of 4.33 and horizontal/vertical tune spreads of 0.04/0.045 are shown in Fig. 8.10 (for details on measurements and theory see [21]). The space charge induced shifts of loss and emittance growth are seen to agree well between simulation and experiment. The simulation can, however, only explain about 50% of the measured beam loss, while the simulated emittance growth is higher. The authors claim that this is to be attributed to the limited knowledge of the SIS18 synchrotron lattice (closed orbit, multipole strengths etc.), which does not allow a satisfactory reproduction of the real dynamic aperture of the machine, hence beam loss. Also, the lack of selfconsistency in the MICROMAP simulations, where the "frozen-in" space charge method is used, should play a role.

New benchmarking experiments on different types of resonances are in progress at the CERN Proton Synchrotron as reported in [23, 24] and [25].

Complementary to code comparisons in large accelerators are experiments including space charge in the table-top Paul-trap devices reported by Okamoto et al. in [26, 27], and by Gilson et al. in [28]. These experiments allow easy parameter changes and good comparison with theory, but comparison with production accelerators is challenging.

[5] Accompanied also by trapping of particles on the resonance, but to a much weaker degree.

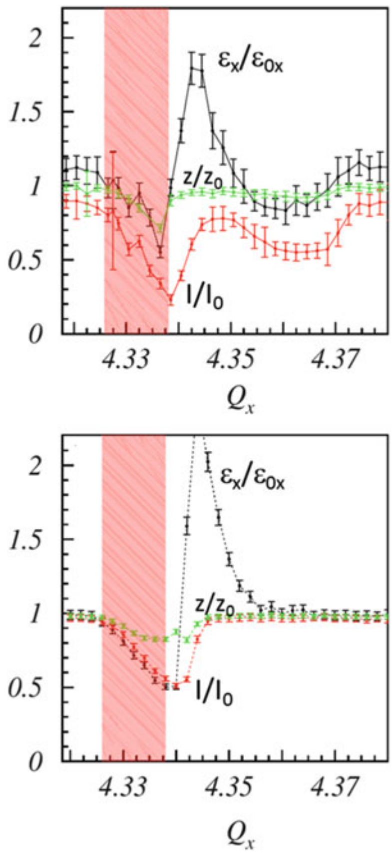

Fig. 8.10 SIS18 nonlinear dynamics and space charge benchmarking campaign. Based on a sextupolar resonance (zero current resonance location marked by bar) with space charge: Relative emittance growth (ϵ_x/ϵ_{0x}), beam loss (I/I_0) and bunch length (z/z_0) as function of horizontal tune shown in experiment (*top frame*) and MICROMAP simulation (*bottom frame*) (Source: [21])

References

1. V. Kornilov, O. Boine-Frankenheim, I. Hofmann, Phys. Rev. ST Accel. Beams **11**, 014201 (2008)
2. R. Baartman, Betatron resonances with space charge, in *Workshop on Space Charge Physics in High Intensity Hadron Rings*, Shelter Island, May 1998, AIP Conf. Proc. 448 (AIP Press, New York, 1998), p. 56
3. H. Okamoto, K. Yokoya, Nucl. Instrum. Methods Phys. Res. Sect. A **482**, 51 (2002)
4. K.Y. Ng, *Physics of Intensity Dependent Beam Instabilities* (World Scientific, Hackensack, 2006)
5. D.C. Morin, Transverse Space Charge Effects in Particle Accelerators, MURA Report 649, Ph.D. thesis, University of Wisconsin, (1962)
6. P. Lapostolle, *Proceedings of International Conference on High Energy Accelerators*, Dubna, 1963, p. 900
7. L. Smith, in *Proceedings of the International Conference on High Energy Accelerators*, Dubna, 1963, p. 897
8. M. Venturini, R.L. Gluckstern, PRST-AB **3**, 034203 (2000)
9. M. Aslaninejad, I. Hofmann, PRST-AB **6**, 124202 (2003)

10. C.M. Warsop, D.J. Adams, B. Jones, B.G. Pine, Proc. HB2016, Malmö, June 2016, paper MOPR030 (2016)
11. A.V. Fedotov, I. Hofmann, Phys. Rev. ST Accel. Beams. **5**, 024202 (2002)
12. G. Franchetti, I. Hofmann, M. Aslaninejad, Phys. Rev. Lett. **94**, 194801 (2005)
13. M. Chanel, Study of Beam Envelope Oscillations Measuring the Beam Transfer Function with a Quadrupolar Pick-Up and Kicker, EPAC1996, Sitges, (1996)
14. R.C. Bär et al., NIM-A **415**, 460 (1998)
15. R. Singh, P. Forck, P. Kowina, W.F.O. Müller, J.A. Tsemo Kamga, T. Weiland, M. Gasior, *Proceedings of IBIC 2014*, Monterey, 2014, p. 629
16. A. Jansson, Noninvasive measurement of emittance and optical parameters for high-brightness hadron beams in a synchrotron, Ph.D. thesis, Stockholm University, 2001
17. W. Hardt, On the incoherent space charge limit for elliptic beams, CERN/ISR/Int. 300 GS/66.2, 1966
18. E. Metral, paper MOPR024, Proceedings of HB2016, Malmö (2016)
19. S. Machida, *Proceedings of 6th International Particle Accelerator Conference*, Richmond, paper WEYB1, pp. 2402 (2015)
20. G. Franchetti et al., Phys. Rev. ST Accel. Beams **6**, 124201 (2003)
21. G. Franchetti et al., Phys. Rev. ST Accel. Beams **13**, 114203 (2010)
22. G. Franchetti, I. Hofmann, G. Turchetti, in *Workshop on Space Charge in High Intensity Hadron Rings*, Shelter Island/New York, 1998, ed. by A.U. Luccio, W.T. Weng, AIP Conf. Proc. No. 448 (AIP, New York, 1998), p. 233
23. H. Bartosik, A. Oeftiger, F. Schmidt, M. Titze, *Proceedings of 7th International Particle Accelerator Conference (IPAC'16)*, Busan, Mar 2016, paper MOPOR021, p. 644 (2016)
24. G. Franchetti, S.S. Gilardoni, A. Huschauer, F. Schmidt, R. Wasef, *Proceedings of 57th ICFA Advanced Beam Dynamics Workshop on High-Intensity and High-Brightness Hadron Beams (HB'16)* Malmö, June 2016, paper TUAM6X01, pp. 278–282 (2016)
25. S. Machida, S.S. Gilardoni, M. Giovannozzi, S. Hirlaender, A. Huschauer, C.R. Prior, *Proceedings of 57th ICFA Advanced Beam Dynamics Workshop on High-Intensity and High-Brightness Hadron Beams (HB'16)*, Malmö, June 2016, paper TUAM7X01, pp. 283–287 (2016)
26. H. Okamoto, H. Tanaka, Nucl. Instrum. Methods Phys. Res. Sect. A **437**, 178 (1999)
27. H. Okamoto, K. Ito, K. Fukushima, T. Okano, *Proceedings of HB2014*, East-Lansing, TUO2LR03 (2014)
28. E.P. Gilson, M. Chung, R.C. Davidson, P.C. Efthimion, R. Majeski, Phys. Rev. ST Accel. Beams **10**, 124201 (2007)

Chapter 9
Emittance Exchange in Anisotropic Beams

Abstract Anisotropy – as imbalance of rms kinetic energies between different degrees of freedom in the moving frame – is an important source of resonant behaviour under space charge. In practice anisotropy may result from production, injection, acceleration, changes in focusing and other sources. This chapter considers space charge as source of resonant emittance transfer in anisotropic beams. The description focusses on theoretical models, with examples of experimental evidence. In circular accelerators the most commonly known example is the so-called "Montague resonance". In linear accelerators such anisotropy occurs between transverse and longitudinal degrees of freedom. Although the distinction between "coherent" and "incoherent' resonance is not always straightforward, examples of clearly coherent features are presented.

9.1 Introductory Remarks

The question arises, what mechanisms can lead to emittance transfer and – at least in part – removal of anisotropy during acceleration or beam storage. Due to the relatively low density of beams in conventional accelerators collisional relaxation towards more isotropic beams does not occur.[1] An alternative source of emittance transfer within the beam is space charge, and its various modes of resonant interaction.

The "Montague-resonance" has been known since the 1960s as undesirable source of horizontal-vertical emittance exchange in synchrotrons, and the original analysis by Montague [1] treated the phenomenon as a purely single particle resonance phenomenon.

For high-current linear accelerators the issue of undesirable emittance exchange in "non-equipartitioned" designs of accelerators was first raised by Jameson in [2, 3] and compared with the theoretical model on "space charge coupling due to anisotropic distributions" from [4].[2]

[1]This is different for long-term storage as in colliders or storage rings, where small angle Coulomb scattering (intrabeam scattering) can be significant.

[2]Fully documented in [5].

I. Hofmann, *Space Charge Physics for Particle Accelerators*,
Particle Acceleration and Detection, DOI 10.1007/978-3-319-62157-9_9

The focus of this chapter is to explore the subject of resonant emittance exchange in a broader context by going beyond Montague's single particle model and discussing it as *space charge coupling* in anisotropic beams as introduced in Sect. 5.3.

9.2 Definition of Anisotropy and Equipartition

Following Sect. 2.2.3 we express anisotropy as ratio of kinetic energies as introduced by the factor T. Assuming an equivalent constant focusing[3] and introducing a and b as rms sizes in the directions z and x, and similar for rms tunes $\nu_{z,x}$,[4] the factor T can be re-written as[5]:

$$T \equiv \frac{a^2 \nu_z^2}{b^2 \nu_x^2} = \frac{\epsilon_z \nu_z}{\epsilon_x \nu_x}. \tag{9.1}$$

This definition is an exact measure of the kinetic energy ratio for KV-distributions, and we extend it to all other rms equivalent distributions used in simulations.

A beam with $T = 1$ is then described as *isotropic* or *equipartitioned* between z and x with the understanding that this is equivalent to equal rms velocities in the moving frame. Obviously, "equipartitioned" does not have the thermodynamic implication here that particles are uniformly distributed on surfaces of constant energy in phase space.

9.3 Montague's Single Particle Approach

Emittance exchange due to space charge forces at or near the fourth order difference resonance condition $2\nu_z - 2\nu_x = 0$ in the transverse plane of a synchrotron was first suggested and analysed in the frame of a single particle model by Montague in [1]. Exchange of significantly different emittances in horizontal and vertical planes is at risk of beam loss in case of aperture limitations. His conclusion was that the resonance should be avoided in circular accelerators by sufficient splitting of horizontal and vertical tunes, unless they are already separated by one or more integers.

---

[3]Equivalent is understood as equal phase advances per meter, independent of the type of focusing.

[4]Here we use z and x as transverse coordinates for easier comparison with the longitudinal and transverse coupling in the later part of this chapter.

[5]This definition assumes, however, upright ellipses in phase space; for tilted ellipses as in convergent or divergent beams, or in periodic focusing, the additional "flow term" $\overline{xx'}^2$ in Eq. 2.8 (similar for z) must be considered.

Montague's derivation is based on the assumption of a rigid Gaussian density profile. The space charge potential, expanded around the beam axis, has even order terms, and the zero-th harmonic of a pseudo-octupole term, z^2x^2, provides the driving term for the single particle difference resonance $2\nu_z - 2\nu_x = 0$, which is a relatively strong resonance for high space charge levels. Analysing the stopband width, it was concluded that sufficiently split tunes are required to avoid emittance exchange from, for example, the horizontal to the vertical plane, and that the needed split increases with space charge.

9.4 Coherent Resonance Approach

From a theoretical point of view, the single particle ansatz by Montague predicts no emittance exchange for the uniform density KV-beam – however large its anisotropy is. Limiting the analysis to a pure single particle resonance phenomenon ignores the existence of the coherent modes of interaction derived in [5] and reviewed in Sect. 5.3. In fact, a useful demonstration of this is the comparison between a 2D PIC-simulation of an anisotropic KV-beam and an rms equivalent waterbag beam in [6], where the analytical theory is compared with simulation based on the MICROMAP code [7].

The resulting rms emittance exchange in the transverse plane of a KV and the rms equivalent waterbag distribution, with initially $\epsilon_z/\epsilon_x = 2$, hence an initial anisotropy $T = 2$, slightly split tunes $\nu_z/\nu_x = 1.04$ and $\nu_x/\nu_{0,x} = 0.8$ is shown in Fig. 9.1. The waterbag example confirms the prediction of Montague, that too close tunes lead to a rapid exchange of emittances due to a fourth order term already present in the initial space charge potential – somewhat weaker for the waterbag than for a Gaussian due to less density nonuniformity. Surprising is a similar effect in the KV-case, with obviously a uniform initial density and no driving term for a fourth order resonance. Both cases indicate an approach to equipartition, but full equipartition is not reached.

The KV-behaviour can be explained only in terms of a coherent difference mode instability growing exponentially from an initial density non-uniformity on the noise level, which is driven by the "energy" anisotropy between x and y. The exponential growth is qualitatively confirmed by the slowly rising exchange in Fig. 9.1. The important conclusion is that an initial density non-uniformity is not needed due to existence of this coherent, resonant exchange instability.

Based on the Vlasov analysis for anisotropic KV-beams summarized in Sect. 5.3, and following [6], the imaginary parts of ω for all types of coherent difference modes can be plotted. This is shown in Fig. 9.2 for the example of $\epsilon_z/\epsilon_x = 2$, with a tune depression $\nu_x/\nu_{0,x} = 0.5$ and a range of tune ratios (top graph). A number of exponentially unstable coherent eigenfrequencies ω are identified. Besides the expected fourth order mode, a second order odd mode (the "self-skewing" mode of Sect. 5.3.3.2) and a third order even mode (Sect. 5.3.3.3) play a prominent role. The comparison with results from the corresponding 2D PIC simulation with

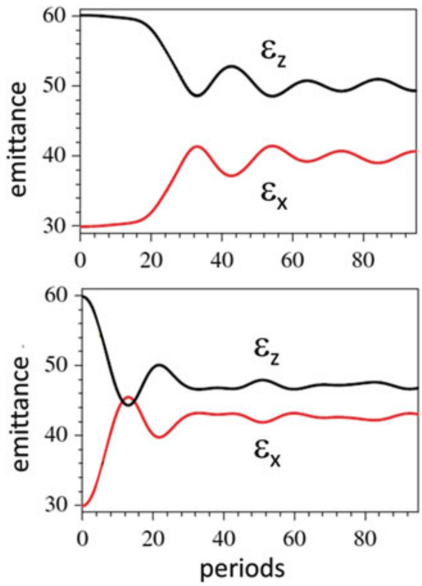

Fig. 9.1 2D PIC simulation with MICROMAP showing coherent nature of emittance exchange for KV (*top graph*) and waterbag (*bottom graph*) distributions for initial $T = 2$ anisotropy, $\epsilon_z/\epsilon_x = 2$, $\nu_z/\nu_x = 1.04$, $\nu_x/\nu_{0,x} = 0.8$. Units on abscissa are betatron periods in x in the absence of space charge (From [6])

MICROMAP and an rms equivalent waterbag distribution in the bottom graph of Fig. 9.2 shows very good agreement.

Interesting is the perhaps unexpected stopband just above $\nu_z/\nu_x = 2$, which is associated with a *third order* even mode instability driven by the anisotropy. Initially, its driving term – a pseudo-sextupole space charge term – only exists on the noise level. The exponential growth predicted theoretically for the KV-distribution matches surprisingly well with the PIC simulation result for a waterbag distribution. Due to the large tune split required for instability of this mode it is unlikely to occur in circular accelerators; but possibly in linear accelerators with a strong focusing imbalance between longitudinal and transverse. In fact, an evidence of it is recently reported from the J-PARC linac, see Sect. 9.6.2.

The simulation results in Fig. 9.2 also give no indication of fifth – for example at $\nu_z/\nu_x = 3/2$ – or higher order resonances.

Note that the dotted vertical line in the bottom plot of Fig. 9.2 stands for "energy equipartition" – a "safe" region. Left from it there is an indication of relatively weak emittance exchange in the opposite direction. It would be enhanced if smaller emittance ratios were chosen, in which case the equipartition point would move to the right.

The question can be raised if periodic focusing systems are equally exposed to these collective resonances. Simulations of the cases in Fig. 9.2 in a FODO lattice show nearly identical results as long as the phase advance is away from the 90° stopband [6].

In summary, there is a good match between the KV-based perturbation theory growth rate spectrum and the final output of a waterbag PIC simulation. For the waterbag distribution the following can be concluded:

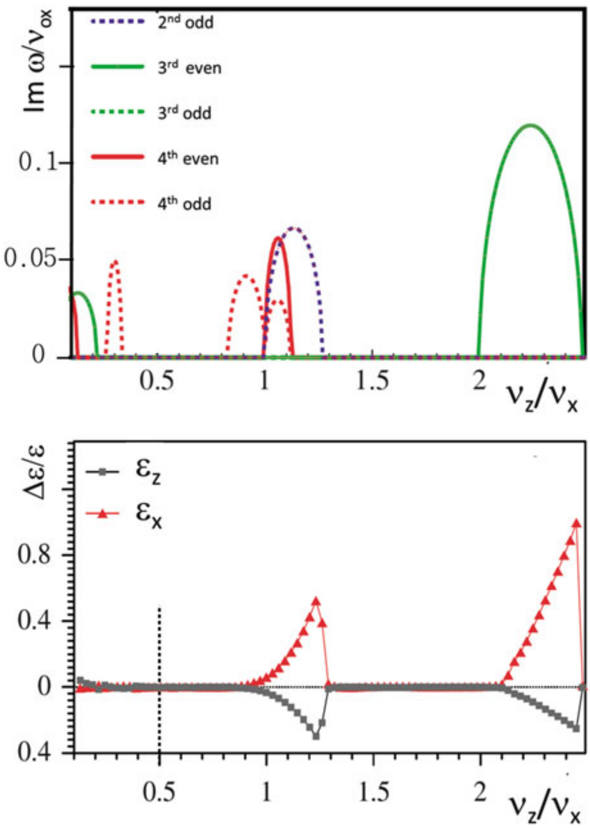

Fig. 9.2 *Top graph*: analytical theory growth rates as function of tune ratios for different unstable eigenmodes of anisotropic 2D KV-beam with $\epsilon_z/\epsilon_x = 2$; *Bottom graph*: 2D PIC simulation with MICROMAP for rms equivalent waterbag distribution, showing saturated emittances, with *dotted line* at 0.5 indicating point of "energy equipartition" (From [6])

- The 2:2 resonance, also called "main resonance", can be interpreted as fourth order single particle difference resonance, since the required space charge pseudo-octupole term is already present in the equilibrium beam. A coherent part, however, enters as shift of the exchange curve to the right of $2\nu_z/2\nu_x = 1$, which suggests a coherent resonance condition $2\nu_z - 2\nu_x - \Delta\nu_{4,coh} = 0$. Furthermore, the self-limiting effect of the exchange is also a coherent effect.
- For the 1:2 third order resonance no single particle explanation exists, and it is entirely due to a coherent, anisotropy driven instability. The shift of the exchange curves to the right of $\nu_z/\nu_x = 2$, suggests an approximate resonance condition $\nu_z - 2\nu_x - \Delta\nu_{3,coh} = 0$, where $\Delta\nu_{3,coh}$ describes the shift.

The rms emittance exchange on these resonance stopbands is predominantly a core, and not a halo effect as is shown in [6]. There is, however, also the possibility that anisotropic halos are subject, for example, to the 2:2 resonance driven by the core space charge as shown in [8]. This way, coupling of transverse halo particles into the longitudinal plane or vice versa can occur even if the core itself is isotropic or near to it. On the other hand such a halo coupling opens the possibility of longitudinal "halo cleaning" by transferring it into the transverse plane by means of the coupling resonance, where it can be scraped more easily.

9.5 Stability Charts

The commonly used resonance charts in the transverse tune space of circular accelerators are usually based on nonlinear dynamics in the externally applied magnetic fields. The space charge "Montague resonance" is an additional, but relatively strong stopband adjacent to second or fourth order difference resonance lines associated with magnet field components.

In linear accelerators magnet driven resonances play no role, and the matter of a suitable resonance chart comes up only in connection with emittance transfer in beams with anisotropy, at varying intensity levels as well as emittance and focusing ratios.

The suggestion in [9] that the analytical theory for anisotropic beams could be used to develop a kind of stability diagram for linear accelerators is supported by complementary studies with PIC simulations in [6, 10–12] and others. The choice of the plane of tune ratio and of tune depression, for a given emittance ratio, is based on these theoretical results. This allows following the evolution of beam parameters – the tune footprint – along a linac as long as the emittance ratio follows the initial value, which is normally the design goal.

Examples of such stability charts[6] are shown in Fig. 9.3. The chart with $\epsilon_z/\epsilon_x = 2$ (top graph) includes the data shown in Fig. 9.2. Growth rates, indicated by the colour intensity coding, are understood as maxima over the unstable modes, including second (odd), third, and fourth order, while white regions are free of instability.

The width of the 2:2 stopband near $\nu_z/\nu_x = 1$ is estimated in [12] as approximately

$$\frac{\Delta(\nu_z/\nu_x)}{\nu_z/\nu_x} \approx \frac{3}{2}\frac{\Delta(\nu_x/\nu_{0,x})}{\nu_x/\nu_{0,x}}. \tag{9.2}$$

At the tune ratio, which equals the inverse of the emittance ratio, initial "equipartition" $T = 1$ is realized – marked by the dotted line. It is characterized by a wide region free of instability. Note that for very large tune depression the stopbands overlap, and a kind of "sea of instability" is obtained.

[6]This and following "stability charts" have been generated with a diagnostics option of the TRACEWIN code, which uses the stability and growth rate data generated by the theory in [9].

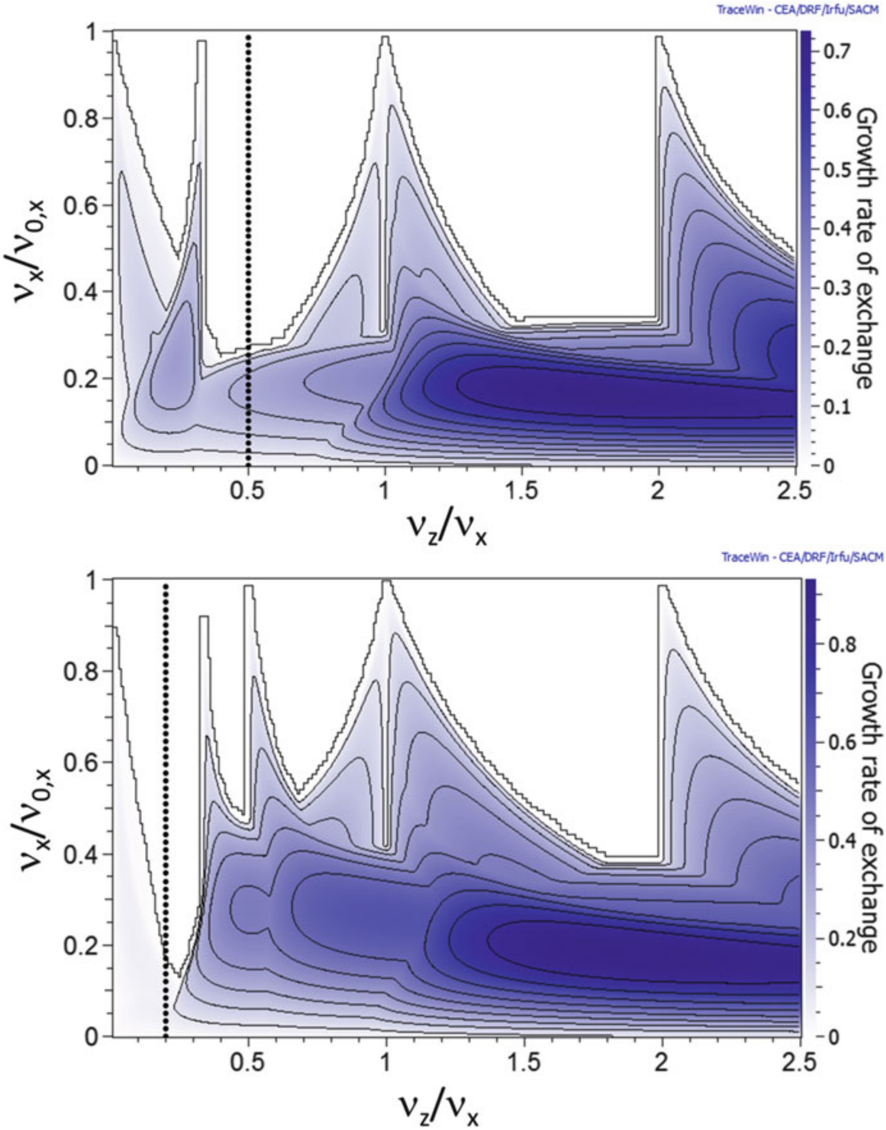

Fig. 9.3 "Stability charts" for emittance ratios ϵ_z/ϵ_x of 2 (*top graph*) and 5 (*bottom graph*), showing the analytically calculated stopbands, where resonant exchange of emittances is predicted, as function of tune ratio ν_z/ν_x (abscissa) and tune depression $\nu_x/\nu_{0,x}$ (ordinate). *Contour lines* indicate levels of growth rates of unstable modes in units of zero space charge betatron units in x, and *dotted vertical lines* the equipartition condition

9.6 Experimental Evidence

Practical demonstration of the agreement between this theory and simulation has been used since 1981 to facilitate linac design practice (as in [2]) and interpret actual performance; but explicit experiments aimed directly at comparison to the theory have been few and only possible in places where sufficient accelerator operation flexibility and diagnostics exist.

We report here about three dedicated benchmarking measurements, pertaining to circular machines as well as linacs.

9.6.1 "Montague-Experiment" at CERN-PS

The scope of these measurements was observation of the "Montague resonance", including a comparison with computer simulation and examining the expectation of coherent resonance effects beyond the single-particle model by Montague. These measurements have been carried out in the context of achieving maximum high-intensity performance in the CERN Proton Synchrotron (PS) during the years 2002–2004 and summarized by Metral et al. in [13].

The measurements were performed with a single bunch from the CERN Proton Synchrotron Booster, which was fast injected into the PS machine at 1.4 GeV kinetic energy on harmonic $h = 8$. The number of protons per bunch was typically 10^{12}. In a code benchmarking experiment, with results shown in Fig. 9.4, the vertical tune was fixed at $\nu_{0,\mathtt{v}} = 6.21$, and the horizontal one, $\nu_{0,\mathtt{h}}$, was varied between 6.15 and 6.25 (constant during each measurement). Initially injected normalized emittances have been $\epsilon_{\mathtt{h}} = 30$ and $\epsilon_{\mathtt{v}} = 10$ mm mrad. The simulations were carried out using the fully 3D particle-in-cell code IMPACT [14], employing a grid of $65 \times 65 \times 257$ in x, y, z, and 10^6 simulation particles with a 6D Gaussian distribution in a constant focusing lattice. They have been run over 1000 turns, which was found sufficient to ensure saturation. The synchrotron period was 1.5 ms, corresponding to 650 turns, while the emittance exchange takes typically 100 turns only, according to simulations. Hence, the synchrotron motion should have negligible influence on the emittance exchange, which then becomes largely a 2D phenomenon.

The widths of the stopbands in experiment and simulation are in good agreement and support the theory background discussed in Sect. 9.4. Also, the stopbands extend primarily left from $\nu_{0,\mathtt{h}} = 6.21$, which is consistent with the fact that $\epsilon_{\mathtt{h}} > \epsilon_{\mathtt{v}}$. The sharp descent of the 3D simulation response curve close to $\nu_{0,\mathtt{h}} = 6.21$ fully agrees with the 2D simulations in Fig. 9.2.[7]

[7] In comparing with Fig. 9.2 it is noted that there the stopband is shifted to the right of the point, where $\nu_z = \nu_x$; this is entirely explained by using space charge depressed tunes instead of zero current tunes as Fig. 9.4.

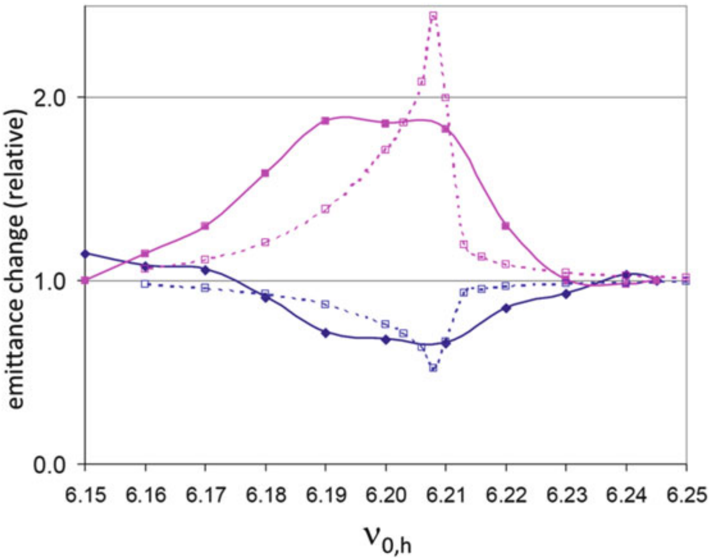

Fig. 9.4 Montague resonance stopband at CERN PS: Measured (*full lines*) and simulated (*dotted lines*, with Gaussian distribution) factors of relative change of rms emittances as function of $\nu_{0,\mathrm{h}}$, with fixed $\nu_{0,\mathrm{v}} = 6.21$. Vertical emittances as *upper* (*purple*) *curves*; horizontal emittances as *lower* (*blue*) *curves* (Source: [13])

This descent is explained as result of the collective response of the charge distribution: a beginning exchange at the left (soft) edge makes the width of the stopband shrink and stops the exchange [10]; this is not the case at the (hard) right edge, where the exchange can fully develop. This strongly asymmetric behaviour is absent in the experimental response curve, where possibly chromatic effects or additional resonances may have had an additional influence.

Besides these "static" measurements with tunes kept constant during each measurement, also "dynamic crossing" measurements have been carried out during the same 2002–2004 campaign at the CERN PS as reported in [13]. The tune was swept through the full range of the stopband during 100 ms real time – corresponding to more than 60 synchrotron periods and over 40.000 turns. Fully self-consistent 3D PIC simulations to model such a long-term behaviour were not feasible at the time of the measurements. With progressing development of the IMPACT code Qiang et al. have reported in [15] about a successful comparison using the fully nonlinear lattice of the CERN PS, with results shown in Fig. 9.5. First, the experimental result showed rms emittance exchange until full "equipartition". This was unexpected in the light of earlier 2D simulations in an idealized lattice as reported in [12]. There, slow sweeping through the stopband from below would just cause a reversal of emittances, hence an adiabatic and reversible process. Obviously this was not the case in the experiment, but the 3D simulations showed excellent agreement with this finding. It can be assumed that near the point of symmetry,

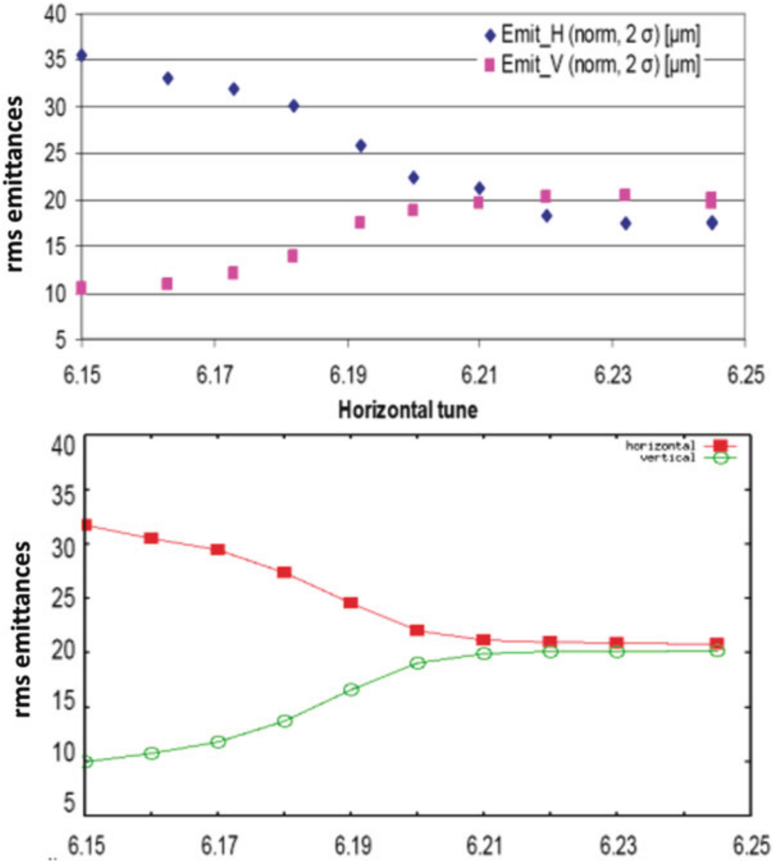

Fig. 9.5 Dynamic crossing of Montague resonance stopband at CERN PS comparing rms emittances from experimental (*top graph*) and simulated (*bottom graph*, with Gaussian distribution) data. The horizontal tune $\nu_{0,\mathrm{h}}$ was swept linearly in time from 6.15 to 6.245 over 100 ms, the vertical one was fixed at $\nu_{0,\mathrm{v}} = 6.21$ (Source: [15])

where $\nu_{0,\mathrm{h}} = \nu_{0,\mathrm{v}} = 6.21$, irreversible processes connected with the combined effects of synchrotron motion, the nonlinear lattice and space charge play a role and contribute to the suppression of an adiabatic, reversible behaviour.

9.6.2 Linac Emittance Transfer Experiments at GSI and J-PARC

The first experiment exploring space charge induced emittance transfer in a linear accelerator was carried out by Groening et al. in [16]. The measurements were taken at tank A1 of the UNILAC heavy ion linac at GSI, and during high-current operation with an Ar^{18+} beam. Results are shown in Fig. 9.6. Transverse zero current phase advances could be varied between 30° and 100° over the 60 cells of the tank, while the longitudinal one was kept constant at 43°. The initial longitudinal:transverse ratio of emittances was a factor 10, and the growth of transverse emittances could be measured at the end of tank A1. At the condition of the main 2:2 resonance, where the ratio of longitudinal and transverse phase advances is near unity, the experiment confirmed the predicted growth of the transverse emittances, as shown in the top graph of Fig. 9.6.

The simulations were carried out with the TRACEWIN and DYNAMION codes. Tune foot prints of the simulations for different values of the transverse phase advance have been plotted on the stability chart for the emittance ratio 10, as shown in the bottom graph of Fig. 9.6, illustrating the location of the 44° case on the 2:2 resonance stopband.

An experiment at the J-PARC proton linac, extending over the full linac, and in a different parameter range, with transverse as well as longitudinal emittance measurements[8] is reported by Plostinar et al. in [17]. J-PARC accelerates H^- for stripping injection into the subsequent rapid cycling synchrotron. It is therefore subject to beam loss by the intrabeam stripping process described by Lebedev et al. in [18]. In the context of minimizing this loss and at the same time avoiding undue emittance transfer four different working points[9] have been examined, with the anisotropy factor $T = k_t\epsilon_t/k_l\epsilon_l$ tuned to the values 1.0, 0.9, 0.7 and 0.5. The initial emittance ratio was assumed fixed at the standard ratio $\epsilon_t/\epsilon_l = 1.2$, which allows operation near "equipartition". In the top graph of Fig. 9.7 these values are located on the stability chart calculated for the given emittance ratio. As predicted by the charts, the simulation cases with ratios 1.0 (equipartitioned) and 0.7 have no emittance exchange, while cases 0.9 and 0.5 show exchange on the 2:2 (fourth order), respectively 1:2 (third order) resonance. These simulations are compared with input and output emittance measurements. Numerical results of measurements for the four different anisotropy factors T are shown in Fig. 9.8. They confirm the theory and simulation predictions of cases 1.0 and 0.9; case 0.7 is found to have a small level of exchange not predicted. Not fully understood is case 0.5, which the authors interpret as experimental observation of the 1:2 resonance. Theory in Sect. 9.4 predicts such a mode as collective instability driven by the combined action of anisotropy and a third order space charge pseudo-sextupole, which is assumed to grow out of initial noise or mismatch. The observed amount of emittance exchange for this particular case exceeds, however, the simulation results for yet unclear reasons, and caution may be required for this interpretation.

In summary, experiments to demonstrate the effects of beam anisotropy and space charge remain a challenging subject in linear accelerators. This includes sufficiently accurate knowledge of the location of dangerous resonance modes and strategies to avoid them. Certainly, more experimental data are needed.

[8] Using wire scanners transversely and bunch shape monitors longitudinally.

[9] This flexibility is owed to the fact that this linac uses electromagnetic quadrupoles.

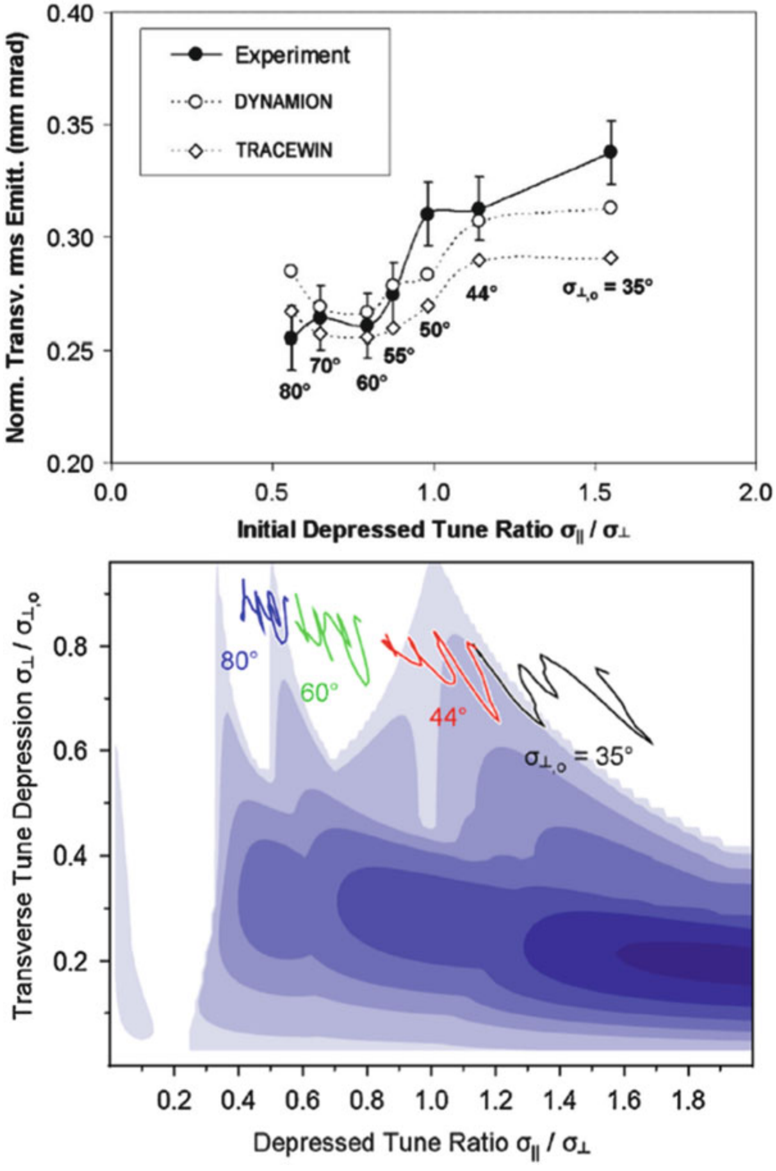

Fig. 9.6 Experiment on space charge induced emittance exchange at GSI UNILAC. *Top graph*: Measured and calculated stopbands as function of tune ratio. *Bottom graph*: Stability chart for UNILAC with simulation tune foot prints near the "main resonance", for different values of transverse phase advance (Source: [16])

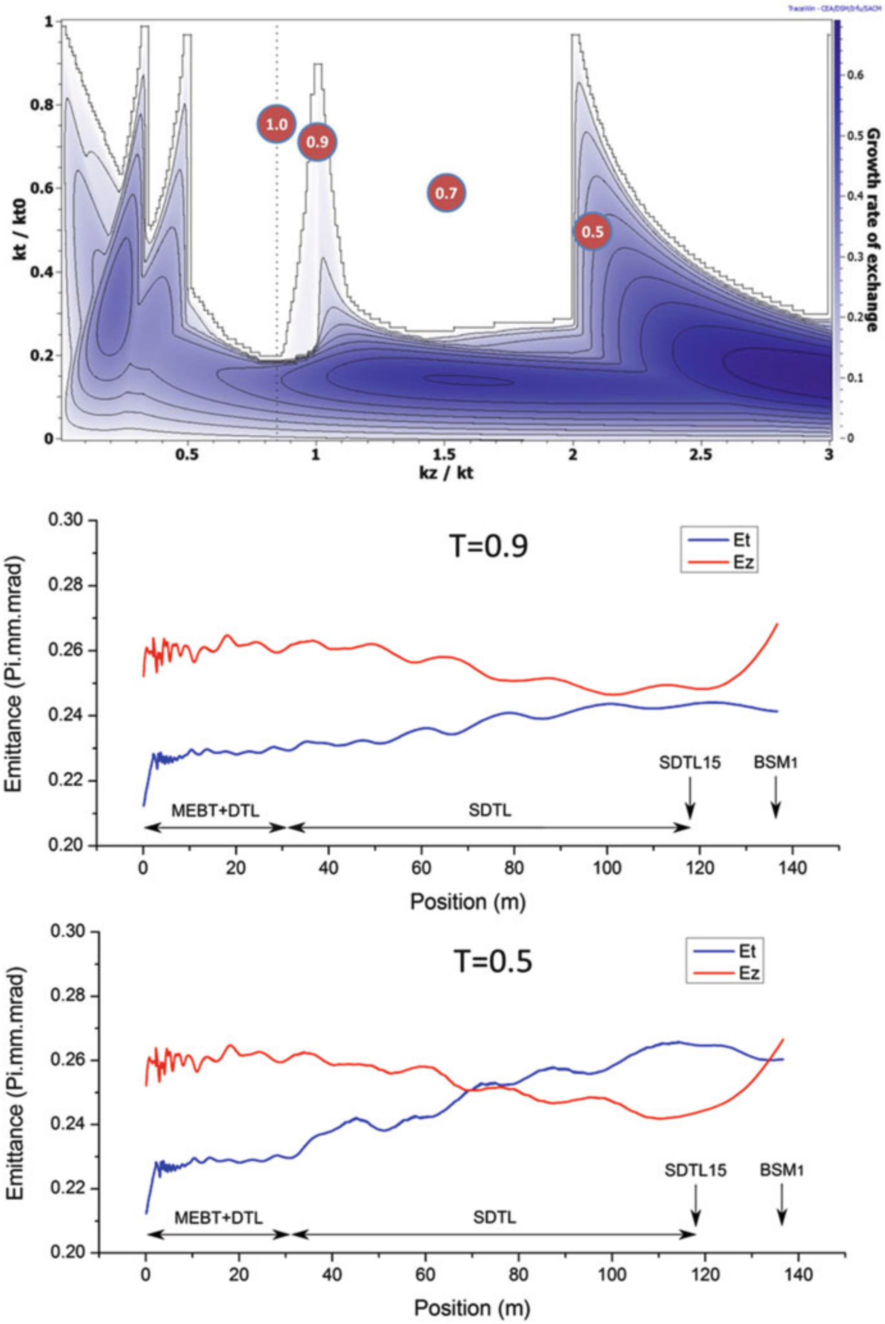

Fig. 9.7 JPARC linac simulation on space charge induced emittance transfer. *Top graph*: Stability chart for $\epsilon_t/\epsilon_l = 1.2$ with different test working points in terms of anisotropy factors T. *Bottom graph*: TRACEWIN simulated emittance evolution along linac for $T = 0.9$ and $T = 0.5$ (Source: [17])

T_t/T_z	ε_t (π.mm.mrad)	ε_z (π.mm.mrad)
1.0	0.216	0.269
0.9	0.229	0.233
0.7	0.253	0.223
0.5	0.293	0.161

Fig. 9.8 JPARC experimental output data pertaining to different values of anisotropy factor *T* in Fig. 9.7 (Source: [17])

References

1. B.W. Montague, CERN-Report No. 68–38, CERN, 1968
2. R.A. Jameson, *Proceedings of the 1981 Linear Accelerator Conference*, Santa Fe, 1981, p. 125
3. R.A. Jameson, IEEE Trans. Nucl. Sci. NS-**28**(3), 2408 (1981)
4. I. Hofmann, IEEE Trans. Nucl. Sci. NS-**28**(3), 2399 (1981)
5. I. Hofmann, Phys. Rev. E **57**, 4713 (1998)
6. I. Hofmann, G. Franchetti, O. Boine-Frankenheim, J. Qiang, R.D. Ryne, Phys. Rev. ST Accel. Beams **6**, 024202 (2003)
7. G. Franchetti, I. Hofmann, G. Turchetti, in *Proceedings of the Workshop on Space Charge Physics in High Intensity Hadron Rings*, vol. 448, AIP Conf. Proc. (AIP, New York, 1998), p. 233
8. I. Hofmann, Phys. Rev. ST Accel. Beams **16**, 084201 (2013)
9. I. Hofmann, Phys. Rev. E **57**, 4713 (1998)
10. I. Hofmann, O. Boine-Frankenheim, Phys. Rev. Lett. **87**, 034802 (2001)
11. I. Hofmann, G. Franchetti, J. Qiang, R. Ryne, F. Gerigk, D. Jeon, N. Pichoff, *Proceedings of the European Accelerator Conference*, Paris, ed. by J.L. Laclare, 2002, p. 74
12. I. Hofmann, G. Franchetti, Phys. Rev. ST Accel. Beams **9**, 054202 (2006)
13. E. Metral at EPAC2004, WEPLT029, E. Metral et al., AIP Conf. Proc. **773**, 122 (2005)
14. J. Qiang, R.D. Ryne, S. Habib, V. Decyk, J. Comput. Phys. **163**, 434 (2000)
15. J. Qiang, R.D. Ryne, G. Franchetti, I. Hofmann, E. Metral, paper WEPPR011, *Proceedings of IPAC2012*, New Orleans, 2012
16. L. Groening, I. Hofmann, W. Barth, W. Bayer, G. Clemente, L. Dahl, P. Forck, P. Gerhard, M.S. Kaiser, M. Maier, S. Mickat, T. Milosic, S. Yaramyshev, Phys. Rev. Lett. **103**, 224801 (2009)
17. C. Plostinar, M. Ikegami, Y. Liu, *Proceedings of 4th International Particle Accelerator Conference (IPAC 2013)*, Shanghai, 12–17 May 2013
18. V.A. Lebedev, J.-F. Ostiguy, N. Solyak, A.V. Aleksandrov, A.P. Shishlo, paper THP080, *Proceedings of Linear Accelerator Conference LINAC2010*, Tsukuba, 2010

Chapter 10
Discussion of Space Charge in Accelerator Design

Abstract Space charge issues and their control are important factors for an effective design of high intensity accelerators, whether circular or linear. They enter into a number of constituents of design work: the choice of suitable lattices and working points, definition of upper bounds in magnet nonlinearities, minimation of lattice errors, various design considerations to avoid beam halo and beam loss, and other measures. The goal of this chapter is to summarize criteria connected with space charge and relate these criteria to the relevant chapters and sections of this book. Obviously, this discussion, which is seen primarily from a theoretical angle, can only serve as a guideline. For practical applications many other factors and constraints will have to be considered.

10.1 Circular Accelerators

In circular accelerators space charge is often seen as main factor limiting intensity, but with very limited direct impact on the design. Lattices are chosen to match with the needs of injection and extraction, acceleration, avoiding resonances etc. There are, however, several design relevant space charge issues:

1. *Working points*: Generally speaking, the distance of the working point to significant resonances in the $\nu_x - \nu_y$ tune diagram must be consistent with the maximum expected tune spread. Flattened density profiles (Sect. 4.2) are advantageous, also flattened longitudinal bunch profiles with higher harmonic rf buckets. Especially for second order resonances (and coasting beams) the "coherent advantage" phenomenon – see Sect. 8.2.4 – can help increasing the acceptable intensity.
2. *Structure resonances*: Working points close to structure resonances are avoided – depending on space charge. This is equally true for space charge driven structure resonances (see Sect. 4.4.2), which would have significant strength at high intensity. Along the same line the envelope instability or an accompanying fourth order resonance at 90° phase advance are usually avoided. However, fast bunch rotation (compression) combined with high intensity may lead to a fourth order structure resonance – depending on the lattice structure and working point (compare Sect. 4.4.3).

I. Hofmann, *Space Charge Physics for Particle Accelerators*,
Particle Acceleration and Detection, DOI 10.1007/978-3-319-62157-9_10

3. *Injection mismatch*: Due to the smaller relative space charge tune depression in circular accelerators an injection[1] mismatch and its consequences on halo – discussed in Sect. 6.1.2 – are less of concern than in linear accelerators. As it always leads to some emittance degradation – even without space charge – good injection matching is desirable.
4. *The "Montague resonance"*: As a purely space charge driven resonant effect leading to exchange of initially unequal emittances the "Montague resonance" is generally avoided by sufficiently split tunes (see Sect. 9). Possible interference with linear coupling effects in combination with space charge needs to be checked (Sect. 8.2.2).
5. *Long-term effects of resonances and space charge*: In bunched beams space charge is an important source of periodic tune modulation and crossing of resonances. Its effect on beam halo and loss, jointly with chromatic effects, is a matter of ongoing research (compare Sect. 8.4).

10.2 Linear Accelerators

For linear high intensity accelerators space charge effects have a more direct impact on the beam dynamics layout of a design. In practice, however, space charge driven considerations must be compared with other important design constraints.

There are several challenges in these issues: First, for the accelerator designer to balance technical and cost constraints versus beam dynamics constraints; second, for a comparison between theory and experiment the difficulty is always faced that idealized models cannot be easily compared with reality, where beams adopt largely unknown 6D phase space distributions and focusing structures are exposed to various kinds of errors.

10.2.1 General Rules

Several beam dynamics criteria addressing space charge issues have been discussed in the literature and found wide acceptance – although some aspects are still under discussion.

1. *Mismatch, with magnet and rf errors*: Deviations from ideally matched beams throughout the accelerator by poor matching and/or errors lead to resonant halo formation driven by space charge (Sect. 6.1.2). The relaxation of mismatch into halo depends much on the tails of the distribution function and is, for example,

[1] This applies, in particular, to single-turn injection.

much faster for a Gaussian than for a waterbag. Matching of beam core and halo are, however, not identical tasks.

2. *Transitions between structures*: Abrupt non-resonant changes in average focusing lead to mismatched density profiles and sudden rms emittance growth by nonlinear field energy, especially for strong space charge tune depression (Sect. 6.3).
3. *Transverse* 90° *stopband*: The commonly accepted rule is $k_{0,x,y} < 90°$ to avoid the envelope/fourth order mode (Sects. 7.5 and 7.6, also Fig. 7.28), which would lead to undesirable rms emittance growth and/or halo formation. An exception can be made, if this limit is exceeded only for a few lattice periods leaving no time for growth.
4. *Longitudinal* 90° *stopband*[2]: Theoretically a corresponding limit $k_{0,z} < 90°$ is required to avoid the longitudinal equivalent to the transverse envelope instability (or accompanying fourth order resonance) provided that the transverse focusing period is identical with the effective longitudinal one. In most room temperature linacs this limit is above what can be reached with technically feasible rf voltages. In superconducting linacs this argument does not apply, and a different reasoning is suggested in Sect. 10.2.2.
5. *Higher order stopbands*: Theoretically the third order coherent parametric resonance ($k_0 > 60°$, Sect. 7.5) might be crossed in linacs, but its practical effect may be small if the stopband is crossed sufficiently fast (similar for fourth order). For a schematic overview on the location of all coherent parametric resonances phenomena we also refer to Fig. 7.28, where $k_{0,1}$ can be related to $k_{0,z}$, and $k_{0,2}$ to $k_{0,x,y}$.
6. *Emittance transfer and anisotropy*: Exchange of emittances, which is intensity dependent, is undesirable. It is therefore accepted that accelerator design should avoid stopbands, like the 2:2 one, where resonant exchange in the direction of more equipartition could occur, as was discussed in connection with the stability charts in Sect. 9.5. On the other hand, suggestions to design an accelerator as "equipartitioned" from the beginning are an unnecessary constraint in view of the large resonance-free areas on the stability charts. Beam halo can also be anisotropic and subject to coupling. As discussed in Sect. 9.4 the presence of one of the coupling resonances – for instance the main 2:2 resonance – can lead to transfer from a halo-intense plane to one with no or weak halo, which may be usable for halo cleaning.
7. *Minimize intrabeam stripping for H^-*: For negative hydrogen beams – to allow stripping injection into a storage ring – the possibility exists that intra-beam stripping leads to particle loss of the resulting proton as was suggested in [1]. The only cure of this source of beam loss is lowering density by weaker focusing, which has the undesirable side effect of enhancing space charge tune depression. As a result, the response on space charge resonances might get more serious.

[2]Note that the longitudinal phase advance is equally defined over the transverse focusing period.

10.2.2 Addendum to Superconducting Linacs

The longitudinal 90° limit was recently revisited in [2], which is expected to be relevant for superconducting linear accelerators and their possibilities of enhanced longitudinal focusing up to the point, where the longitudinal phase advance exceeds the transverse one.

It is argued in [2] that the $k_{0,x,y} < 90°$ limit is only justified in the special case where there is one rf focusing period per transverse focusing cell. This is the case, for example, if transverse focusing is achieved with periodic solenoids, and one rf gap per drift space. With focusing by quadrupoles and one rf gap per drift this amounts to two rf focusing periods per transverse lattice period. Thus $k_{0,z} = 90°$ would be equivalent to only 45° phase advance per rf period[3] as illustrated in Fig. 10.1 for a superconducting linac with, for example, a periodic sequence of cryomodules where each module contains three focusing lattice cells.

It is therefore suggested that in a system as in Fig. 10.1 the effective rf focusing period is only half the transverse one and the choice of $k_{0,z} > 90°$ is acceptable from the point of view of the 90° stopband.

In the design of advanced superconducting linear accelerators this results in an additional design freedom, which allows the option of larger accelerating gradients and stronger longitudinal focusing with potential length and cost savings. In terms of the stability diagrams of Fig. 9.3 a choice of working point to the right of the 2:2 stopband at $k_z/k_x \approx 1$ might become an option – at least from a beam dynamics point of view.

The space $k_{0,z} > 90°$ is, however, not free of additional stopbands. As shown in Sect. 7.7.2, the parametric sum envelope instability in x, y, z defines an additional border, which cannot be ignored. Analogous to Fig. 7.28, a thus modified overview including the correspondingly extended design region is shown in Fig. 10.2. Note the diagonal stopband defined by the x, y, z sum envelope instability. The stopband

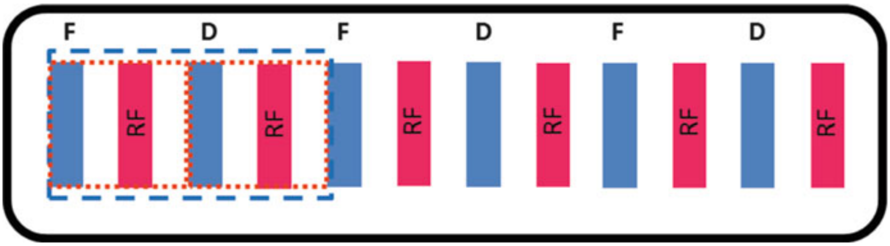

Fig. 10.1 Schematic example of a cryomodule with three focusing lattice cells (*dashed*), each containing two rf periods (*dotted*) (Source:[2])

[3] Note that due to transverse-longitudinal space charge coupling the transverse period is in principle also enforced on the longitudinal one for space charge reasons, but only in a very weak sense not leading to resonant behaviour and emittance growth as shown in [2].

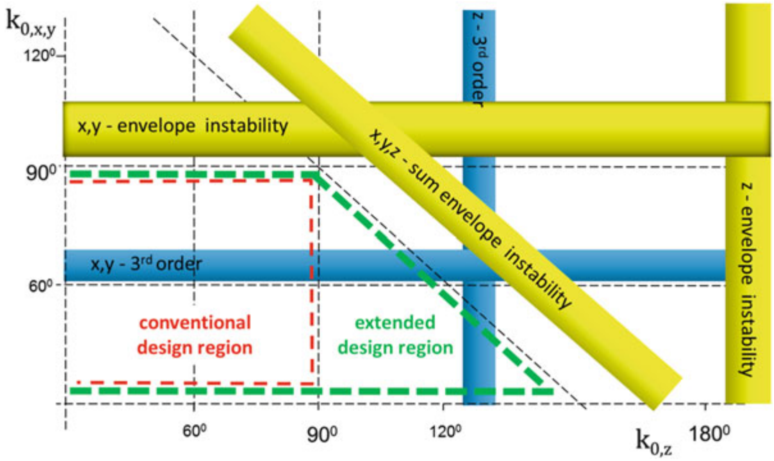

Fig. 10.2 Schematic stability chart of second and third order parametric instabilities for lattice with two rf gaps per transverse focusing period, shown in plane of longitudinal/transverse zero-current phase advances. The extended design region (*dashed green triangular* region) is compared with the conventional one. *Dashed lines* in each order indicating location of zero-intensity limits (Source:[2])

shown above $k_{0,z} = 120°$ is equivalent to a halved phase advance of 60° per rf period, and theoretically connected with the third order parametric resonance discussed in Sect. 7.5.1.3.

In summary, the above space charge based criteria must be understood as guidelines. Their practical application is subject to many technical constraints and verification by multi-particle simulation for a given design.

References

1. V.A. Lebedev, J.-F. Ostiguy, N. Solyak, A.V. Aleksandrov, A.P. Shishlo, paper THP080, *Proceedings of Linear Accelerator Conference LINAC2010*, Tsukuba, 2010
2. I. Hofmann, O. Boine-Frankenheim, Phys. Rev. Lett. **118** (11), 114803 (2017)

Epilogue

Space charge in accelerators has primarily been considered from a theoretical angle, comparing analytical models with the results of multi-particle computer simulations, and to some extent with experimental data from a few specific, dedicated experiments. Such comparisons help to categorize the diversity of mechanisms in which direct space charge matters. Advances made over the past few years have helped to arrive at a more balanced understanding of these mechanisms and narrow the gap between highly idealized analytical models and multi-particle simulations – a trend that is encouraging and should be promoted.

It cannot be overlooked, however, that systematic and clear experimental data on space charge physics processes is difficult to obtain in production accelerators and therefore still quite limited. This is to a large extent due to the challenges of having sufficient diagnostics, and getting enough access to beam time on devices that are primarily user facilities. The impression of many workers in the field that the gap between theory – including simulation – and the real world of operating accelerators is still considerable is not misleading. On the other hand, currently operating high intensity accelerators have largely achieved their initially set goals.

It is sometimes argued that narrowing the gap between theory and experiments is mainly "interesting", but "not important". What clearly speaks against this is that progress in understanding and controlling space charge by means of more dedicated experiments is needed to enhance the performance of existing facilities and for "next-generation" high intensity accelerator projects. However, such experiments must be done carefully and on the basis of adequate diagnostics. Sufficient knowledge of the real machine is crucial, which is a major challenge. This includes knowledge of errors and uncertainties; otherwise better convergence between simulation and experiment becomes difficult if not impossible.

Experiments, even if conducted under the often-difficult circumstances of running machines, also help stimulate new ideas and models of understanding – to the benefit of existing and new projects alike. In order to achieve this goal, ongoing

I. Hofmann, *Space Charge Physics for Particle Accelerators*,
Particle Acceleration and Detection, DOI 10.1007/978-3-319-62157-9

advances in all participating fields are necessary: in understanding analytical theory, in conducting meaningful and well-understood computer simulations and, equally important for theorists and for experimentalists, in devoting much more time to experimental studies.

Glossary

Coherent oscillations/resonances A mode of oscillation with phase correlations between particles (not from periodic focusing) caused by mismatch or by a resonance driving the coherent mode.

Direct space charge interaction The assumption that in the moving frame the effect of space charge can be described in electrostatic approximation.

Error resonances Driven by deviations from specified magnet strength.

Even/odd modes The distinction of eigenmodes of coherent oscillation according to their symmetry.

FODO lattice Focusing-Drift-Defocusing-Drift periodic focusing sequence.

Free energy The assumption of an amount of energy – electrostatic or kinetic – available for emittance growth.

Halo Large amplitude particles beyond initial distribution.

Incoherent oscillations/resonances Oscillations of an ensemble of single particles in a matched or quasi-matched equilibrium, with amplitude growth, but no phase correlations (except for the focusing periodicity).

Landau damping Damping of coherent modes of oscillation by their interaction with particles, or an incoherent spectrum of modes.

Matched beams The assumption that a distribution of particles follows exactly the periodicity of a focusing system, or is time-independent in constant focusing.

Mismatched beam A coherent deviation from a matched beam.

Nonlinear field energy The extra or "free" internal electrostatic field energy of an ensemble of particles due to an unmatched density non-uniformity; note that a uniform beam leads to linear self-fields and minimum field energy.

I. Hofmann, *Space Charge Physics for Particle Accelerators*,
Particle Acceleration and Detection, DOI 10.1007/978-3-319-62157-9

Positive/negative energy modes The phenomenon that excitation of certain modes requires increasing/lowering of the total energy of the beam – here in the moving frame.

Pseudo-multipoles Terms arising from expanding the space charge potential of a beam – analogous to magnet multipoles.

Quasi-matched beams In periodic focusing exactly matched distributions are not possible – with the exception of a 4D KV-distributions –, and “quasi-matched” stands for an approximation to “matched”.

Parametric resonance A periodically modulated parameter of a system, like the length of a mechanical pendulum or the focusing constant in particle optics, can drive the system unstable; frequently the term parametric instability is used specifically for a half-integer frequency relationship in parametric resonance.

Single particle resonance Used as synonym for incoherent resonance.

Rms-equivalence Basis of comparing different distribution functions by assuming equal rms ensemble averages in all directions of phase space.

Smooth approximation Approximation of a periodic focusing structure by a constant one with same phase advances per meter.

Structure resonances Driven by the force from magnets or space charge following the focusing lattice structure periodicity.

Tunes Oscillation frequencies of particles with respect to a reference orbit or a synchronous particle; in linear accelerator notation as $k_{x,y,z}$ in degrees per focusing period, in ring notation as $\nu_{x,y,z}$ in periods per turn. In the presence of space charge usually understood as rms values.

Tune depression The reduction of a “tune” due to space charge.

Tune shift & spread Describes the offset of tunes by space charge; tune spread is the width of a distribution of tunes.